Simulation of Combustor - Turbine Interaction in a Jet Engine

Vom Fachbereich Maschinenbau
an der Technischen Universität Darmstadt
zur
Erlangung des Grades eines Doktor-Ingenieurs (Dr.-Ing.)
genehmigte

D i s s e r t a t i o n

von

Eva Verena Klapdor, M.Sc.

aus Duisburg-Rheinhausen

Berichterstatter:	Prof. Dr.-Ing. J. Janicka
Mitberichterstatter:	Prof. Dr.-Ing. H.-P. Schiffer
Tag der Einreichung:	1. November 2010
Tag der mündlichen Prüfung:	16. Dezember 2010

D 17

Darmstadt 2011

Acknowledgments

This thesis presents the results of my work as fellow of the DFG graduate school 1344, “Unsteady System Modeling of a Jet Engine", at the Institute of Energy- and Powerplant Technology (EKT) at the TU Darmstadt.
I would like to thank Prof. Dr.-Ing. Johannes Janicka for his helpful advice and guidance throughout this period. I am especially thankful for the freedom he gave me for working on my project. I also wish to thank Prof. Dr.-Ing. Heinz-Peter Schiffer of the Department of Gas Turbines and Aerospace Propulsion (GLR) at the TU Darmstadt for taking over the co-review of this thesis. As fellow professor of the graduate school he shared his expertise and ideas concerning the turbine aspects within the field of combustor-turbine interaction.

During my time as a PhD student I was granted to spent some time at Rolls-Royce Deutschland within the combustor development group. I owe thanks to their leader Dr.-Ing. Thomas Doerr and to the whole group for their warm welcome and the good atmosphere. Especially i wish to thank Dr. Ruud Eggels and Dr.-Ing. Max Staufer for their help with the numerical tools.

I want to thank all my colleges at the EKT in particular Dr.-Ing. Du-Fhan Choi and Stefan Bareiss, who not only shared a room with me but also many thoughts on work and non-work related theories. I also like to name Dr.-Ing. Thomas Kania, Niko Spyrou, Simone Eisenhuth and Cem-Koray Ertem with whom I associate relaxing coffe-breaks including off-topic discussions that were sometimes disputable but always refreshing. Frederik Fuest and Jens Kuehne provided me with helpful hints as they read parts of my thesis.

As my thesis covers combustor-turbine interaction I often found myself in discussions with the colleagues from the GLR department. They were always helpful with my concerns on turbine design theory. I especially wish to thank Stavros Pyliouras for the good co-work on our paper and Christoph Biela and Martin Kegalij for revising parts of my thesis.

Most importantly I want to thank my parents and my brother who always supported me, especially in times when I lost the energy to concentrate on my work. They were always patient and found supportive words.

Darmstadt, October 2010
Eva Verena Klapdor

Erklärung zur Dissertation

Hiermit versichere ich, die vorliegende Dissertation ohne Hilfe Dritter nur mit den angegebenen Quellen und Hilfsmitteln angefertigt zu haben. Alle Stellen, die aus Quellen entnommen wurden sind als solche kenntlich gemacht. Diese Arbeit hat in gleicher oder ähnlicher Form noch keiner Prüfungsbehörde vorgelegen.

Eva Verena Klapdor Darmstadt, den 01. November 2010

Nun schaut der Geist nicht vorwärts, nicht zurück,
die Gegenwart allein ist unser Glück.

Johann Wolfgang von Goethe

Contents

Nomenclature

Uppercase Latin Letters		Unit
A	cross section	m^2
A_i	area of face i	m^2
C_*	modelling constants (various *)	-
E_a	activation energy for a reaction	kJ/kg
H	total specific enthalpy	kJ/kg
L	characteristic/integral length scale	m
M	molar mass	g/mol
Ma	Mach number	-
$\mathcal{P}$	probability density function	-
Pr	laminar Prandtl number	-
Pr_T	Prandtl number for temperature	-
$\dot{Q}$	energy source	kJ/(kg s)
R	universal gas constant	-
Re	Reynolds number	-
S	Face of cell	m^2
S_{ij}	strain-rate	$1/\mathrm{s}$
T	temperature	K
T_{tot}	total temperature	K
T_{30}	combustor inlet temperature	K
T_{40}	combustor exit temperature	K
U_{in}	velocity at inlet	m/s
V	volume	m^3
V_k	diffusion velocity of species k	m/s
Y_k	mass fraction of species k	-
$Y_{k,eq}$	equilibrium mass fraction value of species k	-
Y_M	compressibility correction	
$\mathcal{Y}$	progress variable	-
$\mathcal{Y}''^2$	variance of progress variable	-
X	location vector	m
X_k	mole fraction of species k	-
$\mathcal{Z}$	mixture fraction	-
$\mathcal{Z}''^2$	variance of mixture fraction	-

Lowercase Latin Letters		Unit
a	speed of sound	$\mathrm{m/s}$
a_n	neighbour coefficient of pressure equation	-
a_p	central coefficient of pressure equation	-
a_u	central coefficient of momentum equation	-
c_p	specific heat at constant pressure	$\mathrm{kJ/(kg\,K)}$
c_v	specific heat at constant volume	$\mathrm{kJ/(kg\,K)}$
e	internal energy	$\mathrm{kJ/kg}$
$f_{k,i}$	volume force acting on species k	$\mathrm{m/s^2}$
f_n	weighting factor	-
q	gravity vector	$\mathrm{m/s^2}$
h	specific enthalpy	$\mathrm{kJ/kg}$
h_s	sensible specific enthalpy	$\mathrm{kJ/kg}$
Δh_f^0	enthalpy of formation	$\mathrm{kJ/kg}$
k	turbulent kinetic energy	$\mathrm{m^2/s^2}$
k_r	reaction rate coefficient	$\mathrm{m^3/(mol\,s)}$
$\dot{m}$	massflux	$\mathrm{kg/s}$
$\vec{n}$	normal face vector	-
p_{tot}	total pressure	Pa
p	pressure	Pa
p'	pressure correction	Pa
p_{therm}	thermodynamic pressure	Pa
q	energy flux	$\mathrm{J/(m^2 s)}$
q_T	turbulent heat flux	$\mathrm{J/(m^2 s)}$
t	time	s
t_{ij}	laminar shear tensor	$\mathrm{m^2/s^2}$
u	velocity	$\mathrm{m/s}$
u_τ	wall friction velocity	$\mathrm{m/s}$
u^+	dimensionless velocity	-
y^+	dimensionless wall distance	-

Upper Case Greek Letters		
Γ_Φ	diffusion coefficient of a scalar Φ	*
Δ	difference	*
Π	total pressure ratio	-
Φ	scalar quantity	*
Ω	rotation tensor	$1/\mathrm{s}$

Lower Case Greek Letters

γ	isentropic exponent	-
γ_p	under relaxation factor for pressure	-
γ_ρ	under relaxation factor for density	-
ϵ	dissipation of turbulent kinetic energy	m^2/s^3
η	Kolmogorov length scale	m
κ	Karman constant	-
μ	laminar dynamic viscosity	Pa s
μ_{eff}	effective dynamic viscosity	Pa s
μ_t	turbulent dynamic viscosity	Pa s
ν	kinematic viscosity	m^2/s
ν_{rs}	stoichiometric coefficient of reaction r	-
ρ	density	kg/m^3
ψ	circumferential coordinate	$^\circ$
σ_ϵ	turbulent Schmidt number of ϵ	-
σ_k	turbulent Schmidt number of k	-
τ	integral time scale	s
τ_c	compressibility of a gas	$1/Pa$
τ_η	Kolmogorov time scale	s
τ_{ij}	turbulent shear tensor	m^2/s^2
τ_w	wall shear stress	$kg/(m\ s^2)$
ζ	total pressure loss	%
$\dot{\omega}_k$	reaction rate of species k	$kg/(m^3 s)$
$\dot{\omega}_T$	heat release due to combustion	$kJ/(kg\ s)$

Operator Symbols

$\bar{}$	temporal mean
$\tilde{}$	Favre filter
$'$	temporal fluctuation
$''$	fluctuating part of Favre filtered quantity

Abbreviations

acl	axial chord length
ACARE	Advisory Council for Aeronautical Research in Europe
ATB	Air Transport Bureau
BD	Beta Distribution

CAD	Computer Aided Design
CAEP	Committee on Aviation Environmental Protection
CPU	Central Processing Unit
CDS	Central Difference Scheme
CDN	Converging Diverging Nozzle
CFD	Computational Fluid Dynamics
CFL	Courant Friedrichs Levy number / Courant number
CTI	Combustor Turbine Interaction
DFG	Deutsche Forschungsgemeinschaft
FANS	Favre Averaged Navier Stokes
FGM	Flamelet Generated Manifold
FVM	Finite Volume Method
ICAO	International Civil Aviation Organization
LES	Large Eddy Simulation
LTO	Landing-Take-Off cycle
LUDS	Linear Upwind Difference Scheme
MC-TPDF	Monte-Carlo Transported PDF
NGV	Nozzle Guide Vane
OTDF	Overall Temperature Distribution Factor
OPR	Overall Pressure Ratio
PDF	Probability Density Function
PPDF-FGM	Presumed Probability Density Function - FGM
PUC	Precise Unstructured Compressible
RANS	Reynolds Averaged Navier Stokes
RR	Rolls-Royce plc.
RRD	Rolls-Royce Deutschland
RTDF	Radial Temperature Distribution Factor
RQL	Rich burn - Quick quench - Lean burn
TI	Turbulence Intensity
TL	Turbulence Length Scale
UDS	Upwind Difference Scheme

1 Introduction

1.1 Motivation for Combustor-Turbine Interaction Research

Modern jet engines are of highly advanced technology. The components of the thermodynamic cycle (i.e. compressor, combustor, and turbine) operate close to their efficiency limits. But there is still the need for improvement of the overall efficiency. Oil reserves are limited, the pollution due to aircrafts is playing an important role for global warming, more efficient use of resources is requested by politics and the industry is longing for low prices. These, among other things, may be achieved by extending the life time of an engine, reducing fuel consumption, lowering manufacturing costs, lowering material costs etc. Regardless of which aspect, the main cycle components (compressor, combustor, and turbine) are the key factors. But the separate improvement of single components is limited due to the interaction effects between them. Changes in one component may have impact on another and lead to efficiency loss or other problems there. For example, increasing the combustion temperature will increase the carnot-cycle efficiency, but will also cause higher thermal stress and thus shorter lifetime of the high pressure turbine. The need to take the interaction phenomena into account becomes obvious. This thesis captures one of the numerous interfaces within a jet engine: the combustor-turbine interface and the associated combustor-turbine interaction (CTI).

1.1.1 Combustor Development

Two components are involved, while focusing on the combustor-turbine interface: The combustor and the turbine. The combustor is the central component of the jet engine. Thermal energy is added to the thermodynamic cycle by fuel combustion. The combustion must be efficient and stable; reliability of ignition at high altitudes must be given. At the same time pollutants are to be minimized as they are especially harmful to the environment, being released into the atmosphere at high altitudes.

Regulatory stipulations are one of the mainsprings of combustor development and improvement today - in context of pollutants. They are determined by the International Civil Aviation Organization (ICAO). Formal meetings are held every three years by their Committee on Aviation Environmental Protection (CAEP), by which guidelines are set

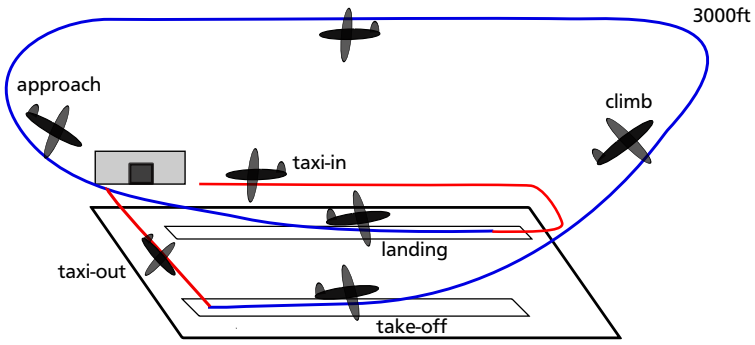

Figure 1.1.: ICAO LTO Cycle with standard power settings during engine certification: 26 minutes taxi (7 % take-off thrust), 42 seconds take-off (100 % take-off thrust), 132 seconds climb (85 % take-off thrust) and 4 minutes approach (30 % take-off thrust)

in what extend engines' emissions need to be decreased. These guidelines are ultimately concerted with the contracted states of the Air Transport Bureau (ATB) and are compulsory for all engine manufacturers. Nitric Oxides (NO_x) emissions allowed for a jet engine are given in Annex 16 Volume II to the Convention on International Civil Aviation [1]. They are measured during the standardized landing take-off (LTO) cycle shown in figure 1.1 as tested during certification of an engine.

The allowed amount of NO_x emission depends on the engines overall pressure ratio (OPR) and the thrust generated. With increasing OPR the allowable amount increases. The limits from the last three CAEP meetings are given in figure 1.2 for engines with more than 89 kN thrust. In the same figure the emissions of some exemplary engines are shown. Momentarily, most of the engines operate below CAEP 6 limits. But with further decreasing limits, which are planned for the future, these engines will not get certified anymore. In 2001 the "Group of Personalities" of the Advisory Council of Aeronautics Research in Europe (ACARE) announced their vision for 2020 [86]. These include a reduction of CO_2 emission by 50 % and NO_x emissions by 80 % compared to emissions allowed by CAEP 2. While some of these reductions are to be achieved by the overall reduction of fuel consumption, approximately 50 % are addressed to combustor improvement. The according benchmark is also shown in figure 1.2.

To link the goals of NO_x reduction to combustor development the respective formation mechanisms must be considered. Four different mechanisms are commonly distinguished [132] for NO: The thermal, prompt, nitrous oxide, and fuel-bound "routes". Without covering the details, the main facts for designing NO-low combustion are the following:
Thermal NO is formed according to the Zeldovich mechanism [140]. The formation exponentially increases with temperature and is significant for temperatures higher than

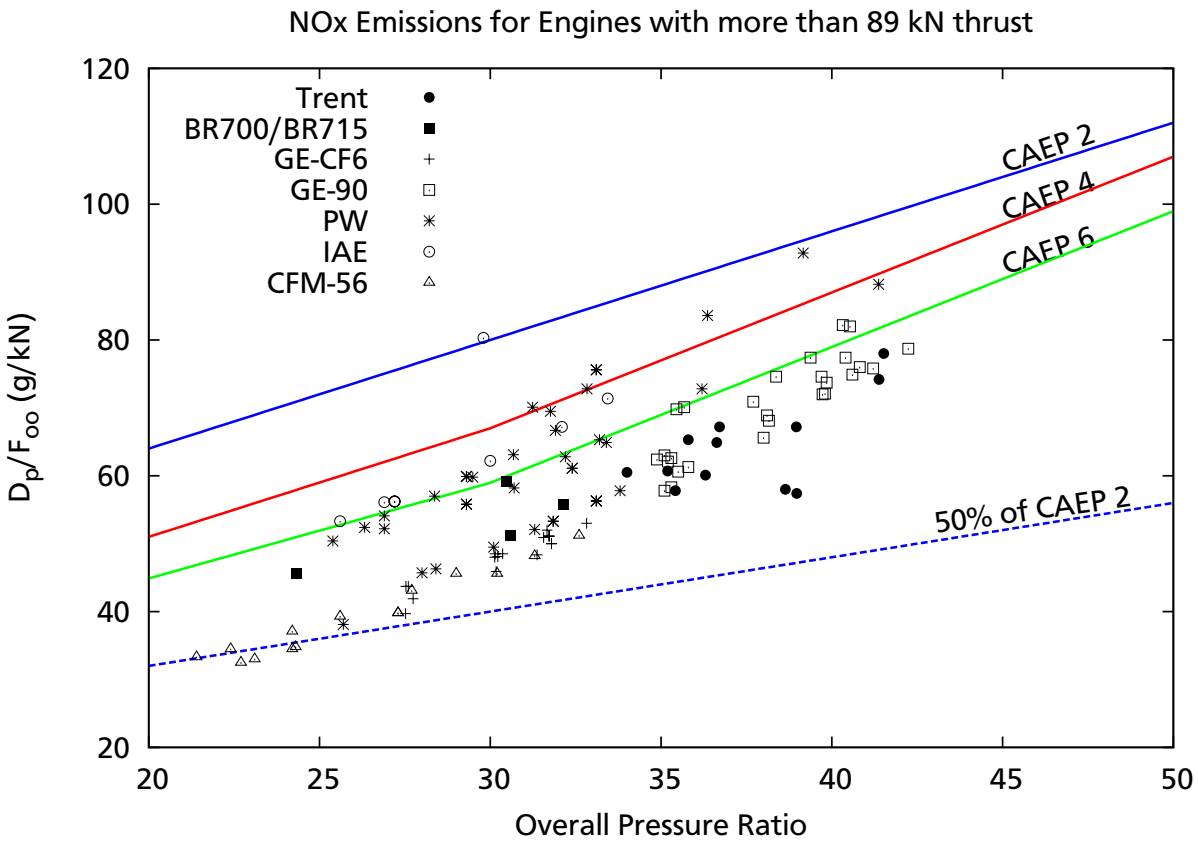

Figure 1.2.: Allowed mass in grams of NO_x emissions (D_p) per rated output (F_{oo}) depending on the overall pressure ratio of the jet engine. Regulatory limits according to CAEP 2, CAEP 4 and CAEP 6 and data for selected engines with more than 89 kN thrust, according to ICAO databank [53]

1700 K. Oxygen (O_2) is needed for the formation reaction. Hence, to reduce thermal NO, the crucial parameters are a low temperature, a low O_2 concentration and a short residence time. The prompt NO, also called Fenimore NO, forms at the flame front only and needs carbon hydrates (CH) for the reaction. Therefore it is mainly associated with rich flames. In contrast to thermal NO it already forms at lower temperatures around 1000 K. NO formation via the nitrous oxide (N_2O) mechanism is usually negligible. The percentage to the total NO formation increases, if lean premixed measures are used that lower thermal and prompt NO. These measures have a smaller influence on the nitrous oxide mechanism. Another source for NO is the fuel bounded nitrogen. However, this is rather a problem in coal combustion and is irrelevant as design criteria for jet engine combustors.

Two main strategies of combustion design have evolved from the need to lower NO emissions. The staged Rich burn-Quick quench-Lean burn (RQL) and the Lean-Burn technology. RQL-combustors have three zones: The first zone, in which a rich flame guaranties a stable reaction, adjacent a quenching zone, in which the reaction is cooled

to minimize thermal NO_x production, and closing with a lean zone in which the fuel's burnout is controlled. This staging concept is also known from modern steam generators in power plants.

Further improvements for this concept are possible but to reach the ACARE goals on NO_x emissions, the Lean-Burn technology is more promising, especially for larger engines. It is also referred to as Low-NO_x technology; a detailed description on its basics and development is given by Lazik et al. [73, 74].[1] Using premixed combustion can minimize thermal NO_x formation during the combustion process, as the temperatures are lower. Here, the flow needs to be stabilized with increased swirl. For this technology no extra "lean burn zone" as found in the rear part of RQL combustors is necessary. On the one hand this can lead to more compact combustors, on the other hand the swirl used is considerably higher, the swirl nozzle is bigger (figures of such nozzles can also be found in [74]). An increased interaction between the flow in the combustor and the flow in the turbine is to be expected. Especially effects on the turbine will increase as in Lean-Burn combustion systems no primary and secondary air jets penetrate and degrade the swirl. Additionally, the temperature profile at the exit of the combustor will probably be higher near the walls compared to the temperature profiles of RQL combustors. This would lead to higher thermal load on the stator-plates. Another problem that arises with Lean-Burn technology is an increased instability of the flame. The unsteady flame front exhibits pressure dynamics that can cause combustion instabilities and harm the structure of the combustion chamber. The first stator of the turbine, commonly named nozzle guide vane (NGV), is part of the high-pressure structure and may influence the unsteady temperature field within the combustor [107].

It must be mentioned here, that different jet engine manufacturers follow different strategies concerning development of combustor technology. While Rolls-Royce (RR) and Pratt and Whitney are to improve RQL-combustors for small engine applications, and Lean-Burn technology for larger thrust engines, General Electric is relying on Lean-Burn only and is striving to implement a scalable Lean-Burn combustor technology for all their engines.[2]

[1] Lazik and his co-authors are development engineers for the combustor technology at Rolls-Royce Deutschland.

[2] Company strategies as presented at the IGTI ASME 2010 in Glasgow at Penal Session: Low emissions aviation technology to meet future regulatory requirements.

1.1.2 Turbine Development

The second component to be considered in CTI is the turbine. It must react on whichever flow conditions exit the combustor. Here, the temperature and total pressure profile are important. The temperature distribution should incorporate a lower temperature at hub and casing, as the mechanical stresses are highest at the hub and the tip is difficult to cool. This is of course mainly true for the rotors of the turbine and it may be questioned whether the temperature-traverse from the combustor is still existent behind the stator. The flow is subject to the influence of secondary flow effects within the stator that will influence the temperature distribution [13]. The swirl from the combustor may additionally have an impact on the flow through the stator and succeeding stages of the turbine.

To characterize the temperature profile at the exit of the combustor, two parameters are commonly used. The overall temperature distribution factor OTDF:

$$\text{OTDF}(\psi, r) = \frac{T_{\text{max}}(\psi, r) - T_{40}}{T_{40} - T_{30}}\,, \tag{1.1}$$

and the radial temperature distribution factor RDTF:

$$\text{RTDF}(r) = \frac{T_{\text{mean}}(r) - T_{40}}{T_{40} - T_{30}}\,, \tag{1.2}$$

where ψ is the circumferential coordinate and r is the radius, which is measured from hub to tip. T_{30} and T_{40} are the combustor inlet and exit temperature, respectively. The circumferential variation of the temperature is averaged in case of the RTDF.

In turbine development today the averaged total temperature and these parameters are considered for design as inlet condition [29]. But these parameters do not give explicit information of the actual two-dimensional temperature traverse, to which the NGV is exposed. Many studies have shown that the temperature field exiting the combustor is highly non-unifom and that the aerodynamics and heat loading of the turbine are actually influenced by this non-uniformity. The following outline shall give an overview of the last 30 years of CTI research, subsuming the most important steps for each of the three categories:

- combustor effects on turbine
- turbine effects on combustor
- combustor turbine interaction.

1.2 Development and State of the Art in Combustor-Turbine Interaction Research

1.2.1 Influence of Combustor Flow on Turbine

Historically, one of the first investigations on CTI were conducted by Stabe et al. [123] in 1984. The influence of non-uniform radial ("realistic") temperature profiles on the performance of a turbine of a high bypass ratio engine compared to the formerly widely assumed uniform inlet temperature was experimentally studied. The overall performance of the turbine was found not to be influenced. The inlet total pressure profile significantly changed near the hub, being exposed to the implemented combustor exit temperature simulator.

In 1986 Butler et al. [21] kept the total pressure within the temperature distortion constant. The NGV remained unaffected while within the rotor a separation of the hot and cold gas areas to the pressure and suction side, respectively, occurred. A numerical investigation on the same setup was performed by Rai et al. [101]. Parts of the setting needed to be changed as they performed only two-dimensional calculations which resulted in several discrepancies between the experimental and numerical results. However, their study corroborated the experimental observation, that the flow through the NGV is not affected by the hot-streak,[3] while the rotor is. In 1988 Krouthen et al. [66] also did simulations of the same experiments, while concentrating on the development and analysis of the used numerical tool and the influence of using different boundary layer models. Three dimensional simulations of Butler's experiment [21] were done in the early 90's by Dorney [33, 32] and Takahashi [126, 127]. They offered a possibility to have a closer look on the flow phenomena in the stator and rotor. The focus of all these studies was layed on the interaction between hot-streaks and rotor. The basic consent was formed, that considering non-uniform temperature profiles exiting the combustor is important when designing the first stage of a turbine.

The aforementioned investigations were conducted at low-speed. In 1995 Shang et al. [117] introduced a new test rig that simulated hot-streaks and radial temperature distortions in a transonic turbine stage. Additionally, temporal fluctuations were added to the hot-streak generator to simulate turbulence intensity levels similar to those measured at combustor exits (they assumed 8 % citing [83], while also higher values up to 40 % are reported in the literature [65, 43]). No influence of the turbulence level on the heat transfer in the rotor was observed. The temperature distortions with an RTDF of up to 12 % significantly changed the rotor blade heat transfer.

[3] hot-streak: "pronounced non-uniformities in combustor exit flow temperature" [97]

In 1996 Dorney et al. [34] simulated a combustor hot-streak migrating through subsonic and transonic flows and found that the predicted influence on the heat transfer coefficient is more prominent in the transonic flow condition. Still, a uniform total pressure field was assumed at the inlet, which is not present in real engines.

One critical region of the combustor-turbine interface is the NGV platform (endwall) as it must resist the highest thermal stresses. While the endwall-heat-transfer has been under investigation for a long time, Radomsky and Thole [100, 99] added the aspect of high free-stream turbulence exiting the combustor to the experimental investigations in 2000. These engine-like turbulence was found to increase the endwall heat transfer compared to the heat transfer at standard test rig turbulence intensities. However, the heat transfer in the leading edge region was almost unaffected by increased turbulence intensities. The experimental setup for this study was introduced by Bangert et al. in 1997 [5]; flowfield and thermal measurements were documented by Kang et al. [60]. With this test rig the focus was oriented towards the flow and thermal field around the NGV. The research group of Thole identified a noticeable impact on the secondary flows within the stator passages [47, 48]. These secondary flows are known to cause aerodynamic losses and high convective heat transfer. Furthermore they interact with the film-cooling that is used to cool the endwall regions. As cooling efficiency is the key for long durability of the hot gas components, a profound understanding of the influencing effects is of high importance. Another aspect they pointed out was the difference in influence of temperature and stagnation pressure gradients. They concluded from their computations, that by a decreasing stagnation pressure from endwall to midspan a changed flow pattern could be observed in the NGV passage [47]. Merely a slight difference in secondary flow was present while varying the temperature gradients.

At the same time Burd and Simon [19, 20] experimentally investigated the effects of two-dimensional slot bleed injection on vane cooling performance. The slot bleeding method was presented as a promising new attempt to increase cooling efficiency compared to film-cooling, also offering the possibility to suppress secondary flow losses in certain areas of the set-up. The inflow of their test section was delivered with 9 %, large-scale turbulence intensity. Barringer et al. [8] however pointed out that for realistic engine-like conditions simulating a non-uniform total pressure field entering the NGV was missing. Therefore, a combustor test section was built that contained film-cooling holes and dilution shootes as well as slot-cooling at the end of the combustor, to provide prototypical conditions for the downstream turbine. Measurements of temperature, total pressure and turbulent intensities were taken at planes before and after the cooling slots. Turbulence intensities of 15-18 % were reported, with indication that the turbulence length scale scales with the dilution holes' diameter. The total pressure field exhibited non-uniformities, as expected.

As a next step the NGV of Bangert et al. [5] was placed behind the combustor simulator to allow for a closer look at the combustor-turbine interface [25, 26]. This study is very interesting as it is the first of its kind. Influences of the combustor cooling concept showed indications at the downstream vane endwall. The cooling set-up led to significantly different secondary flow patterns than expected from two-dimensional turbulent boundary layer theory, which had been used to explain secondary flow structures in turbine passages since its introduction in 1980 by Langston [69]. A computational study on that geometry was published by Stitzel and Thole [124]. The combustor and the NGV were integrated in one domain. Distinct differences of the flow field around the NGV for different cooling geometries were observed. The evaluation was focused on the impact on the NGV flow, but not on the combustor flow. The computations (as the experiments) were non-reacting and the Mach number remained within the incompressible regime due to the scale-up of the test section while matching the Reynolds number [125]. The influence of the combustor-turbine gap was investigated by Cardwell in 2007 [22]. The width of the gap is varying during operation of the engine due to heat expansion of the combustor. The effects of different mass and momentum fluxes on the cooling performance of the vane endwall were investigated, while influences on the combustor flow were not considered.

In the early years of CTI research hot-streak influence on the turbine was mainly considered in terms of its influence on the rotor, summarized in the review paper of Dorney et al. in 1999 [35]. In 2004 Jenkins et al. [58] experimentally simulated a hot-streak impinging on the NGV leading edge, which was film-cooled by a showerhead configuration. The setup of the experiment was introduced in [92] and velocity measurements of the stagnation field are published in [93]. They investigated the effects of high mainstream turbulence and added the effect of varying the pitch position of the hot-streak in [57]. Both - the high free-stream turbulence and the pitch position - showed significant influence on the hot-streak attenuation caused by vane cooling.

One of the more complex rigs is operated by the group of Prof. Thole. It is aimed to include all effects coming from real engine combustors into the simulation of heat transfer within the turbine. A combustor simulator [9] is embedded into the turbine research facility at the Wrigth-Patterson Air Force Base in Dayton, Ohio [45]. It is operated non-reacting. The non-uniform pressure, temperature and turbulence fields entering the turbine are generated artificially [10]. While it includes a combustor panel, the focus of this rig is at the heat transfer and flow conditions within the NGV. Studies on the feedback into the combustor were not published yet. Most recently, studies have been published focusing on the thermal and flow field within the NGV in 2009 [11, 12, 13].

Today the most common numerical approach towards investigating effects from the combustor on the turbine is to mesh only the NGV (and rotor) and apply varying parameters at the inlet boundary to simulate different combustor outflow conditions. An et al. [3, 4] studied the influence of hot streaks by comparing simulations with different total temperature non-uniformities at the inlet. All other variables were kept constant. While they varied the relative pitch of the hot spots to the vane (also known as clocking) He et al. [46] investigated different numbers of hot-streak and its effects on blade heat load. Povey et al. [97] built up a rig that matches Mach number, Reynolds number and turbulence intensities from a real engine. They also give an overview on the latest researches in that area. Martelli et al. [77] numerically studied the same rig concentrating on the hot-spot effects on the rotor. Povey [98] also gave an overview on different experimental simulation strategies of combustor hot-streaks. While the detailed results of these studies shall not be given here, the overall essence is important: They all conclude that hot-streaks and their shape and distribution play an important role on the vane thermal load and heat transfer.

An interesting numerical study is the one by Turell et al. [130]. To study the heat impact of a hot-streak of a high-swirl, lean premixed gas turbine combustor on the first stator row, the entire set-up of a canned combustor from the swirling nozzle until behind the NGV was simulated. For the reactive calculations the two-step global mechanism of Westbrook and Dryer [134] was used. The rotating vortex was directed towards the leading edge of an NGV but “attracted” by the low pressure on the suction side.

1.2.2 Influence of Turbine Flow on Combustor

Investigating the influence of the NGV on the combustor flow is a very new research area, thus only a few publications are available. It is only investigated numerically so-far. Historically, the turbine and combustor community are two separated groups. While the turbine community early started to investigate the influence of the combustor outlet flow on the turbine, the combustor community was concerned with other topics. The catalyst for this new interest can be attributed to recent developments in numerical tools, especially the spreading of reactive Large Eddy Simulation (LES, see section 2.2.1) methods. They are found to be advantageous for accurate, predictive simulations of combustion processes, including complex flow mechanisms as found in practical combustion systems (high turbulence, swirl, and mixing) [90]. For these simulations often incompressible solution algorithms developed for solving low-Mach number flows with heat release are used. Here, a convective boundary condition is applied at the outlet (e.g. [76, 30]); a zero gradient for pressure is assumed at the outlet. Thus, the pressure at the outlet only depends on the velocity field inside the combustor domain. This is ac-

tually not true for the combustor outlet of a real engine, as the NGV induces a potential field in front of it. The static pressure and thereby velocity field at the combustor outlet are thus also affected by the configuration *outside* of the combustor domain. Therefore, the incompressible technique is unsuitable to take effects addressed to the NGV into account.

In 2008 Roux et al. [107] investigated the influence of the NGV on the mean and unsteady velocity and temperature field by using a compressible solver. Two calculations were performed: One in which the stators were included into the computational domain of a combustor, and one, for which the end of the domain was placed in front of the NGV. Strong influence on the mean quantities in the rear part of the combustor and lower influence in the front part, was observed by comparing the simulations. The unsteady field was affected significantly in the rear part, especially the temperature. This is highly important as temperature fluctuations (fluctuations in heat release) can cause combustion instabilities that may damage the combustor if resonant modes of the combustor body are excited. Furthermore, the temperature profile at the exit is *the* criteria when designing a combustor (due to its impact on the turbine, which was outlined in the preceding section). Unfortunately, no explicit information on the used pressure condition at the outlet is given. They merely state that the pressure condition at the outlet "imposes 4.4 bars in the combustion chamber in the two cases". Only a non-rotating, uniform velocity would exhibit a constant pressure field. In numerical simulations it is therefore advisable, to place the outlet boundary condition far downstream from the real exit under investigation. This is obviously not the case in their simulation without the NGV. A study of Xia et al. [138] pointed out the effect of choosing a constant pressure over a realistic pressure profile. The flow structure will be altered near the outlet of the numerical domain.

While concrete, real-geometry studies on the feedback from the NGV to the combustor flow are hard to find, there exist some fundamental, experimental investigations concerning the influence of outlet boundary conditions on swirling flow by Escudier et al. [36]. The influence of different outlet geometries on the swirling flow in a pipe has been investigated. For increased swirl (higher ratio of circumferential to axial velocity) they observe changes in the recirculation zone; i.e. it is shortened. They use the vortex breakdown theory to explain this phenomenon, including the fundamental explanations of Benjamin [14, 15], which identifies sub- and supercritical flow structures in which the former allows information in the flow to travel upstream.

1.2.3 Coupling Strategies

A study of Stanford [79] is aiming to simulate the entire jet engine fully three dimensional within one simulation. The domain is split into the main components compressor, combustor and turbine and separate codes are used for each part. The reactive flow within the combustor is simulated using LES modeling. The flow in the turbine is simulated with a different code, which was developed for turbomachinery applications using unsteady Reynolds Averaged Navier Stokes (RANS, see section 2.2.2) modeling. Transient data is passed between the two codes after every outer iteration. A special software framework [114, 2] is used for executing multiple solvers simultaneously. Each solver communicates with this software, which handles all the search and interpolation routines. One major difficulty is the transformation of LES data into RANS data and vice versa [113]. The whole process may lead to a time consuming data interface as well as to accuracy loss due to the transformation. As noted in [79] they computed a 20° sector of each component. The grids had a total number of 14 million cells and 700 CPUs run for 24 hours to calculate 1500 time steps, while 11,500 steps are needed for a full revolution of the compressor. The grids used for the compressor and turbine were "coarse" grids. To simulate on fine meshes they estimated a needed number of 4000 processors to perform the calculations within the same time. Today this enormous need for computing power and time is still rather available in academia than in industry.

A straightforward way to simulate CTI is the integration of both components in *one* computational domain, as done by Roux et al. [107] and Turell et al. [130]. Both studies, however, had a major drawback considering the combustion simulation. A one- and a two-step kinetic scheme, respectively, were used. These are not complex enough to calculate interesting species concentrations accurately. A combustion modeling technique like flamelet generated manifolds (FGM, see chapter 2.3) is more promising and has shown to yield good results in RANS and LES context. Recently, efforts are taken to even predict NO with an extended version of FGM by Ketelheun et al. [62]. This is of special interest as NO reduction is one of the main concerns in establishing new combustor technology.

This second approach, which includes both, combustor and stator in one domain, is also to be followed in this thesis. The superior combustion modeling (FGM) technique shall be used.

1.2.4 Experiments and Numerical Simulations

Experiments and numerical studies are conducted to understand the flow phenomena and interaction processes between combustor and turbine. The final goal is the definition of guidelines for improved design concepts. Experiments in industry are aimed to find the most promising geometric set-up and therefore are as close as possible to final geometry and operating conditions. Many experiments in university use test rigs that isolate generic features. A closer look on single phenomena is possible. Large test facilities, that include both combustor and turbine, are expensive and need complex peripheries. These are maintained by national laboratories (e.g. DLR in Germany, NASA in America) or are implemented at universities when financial support from industry is granted. The main remaining problem for experimental investigations is to build a test rig that operates close to the real conditions. Today, realistic turbulence, pressure and velocity fields are commonly realized in experiments. While maintaining the Reynolds- and Mach number the temperature remains below real temperatures. The exit profiles of modern jet engines' combustors are 1300 - 2000 K hot, depending on the operating flight condition (take-off, cruise, idle). Thermocouples operatable in these conditions are very expensive and have a short life-time. The stators in such a test rig would need extensive cooling and special material to resist the thermal stresses. Technically one would end up with a real jet engine equipped with necessary instrumentation, ideally with optical access for non-intrusive laser measurement techniques.

The operating conditions draw no limits for numerical simulations. These present a comparatively low-cost alternative. At the same time geometric alterations are easier to implement. Accompanying the experimental investigations a new perspective was added to the understanding of CTI within the last decade. The vast majority of the investigations concentrated on the influence of the combustor exit profiles on the flow through the NGV. Only little consideration was given to the feedback from the NGV to the combustor. Studies on the whole system "jet engine" are also seldomly found in the literature, as those require a high amount of computing power, that is nowadays available only for a few research institutions. As pointed out before there is a need to simulate both, the flow through the NGV but also the complex flame-turbulence interaction and the reaction products that are important to know for combustion design. The aim of this thesis is to develop such a numerical tool.

1.3 Context and Outline of this Thesis

The flow through combustor and NGV is characterized by two regimes. On the one hand there is the compressible regime in the turbine and on the other hand there is the reactive regime within the combustion chamber, where thermal energy is added to the fluid via the reaction process. If one seeks to simulate effects between the combustor and the first stator vane of the turbine of a jet engine, the used equations and solution algorithm need to account for both regimes.

Context of this Thesis

The project, in which context this thesis is written, is part of the DFG[4] graduate school 1344 (Graduiertenkolleg 1344), "Unsteady system modeling of a jet engine". The scope of sub-project C5 is the numerical investigation of the interaction between the combustor and turbine flows. The graduate school is based on the cooperation between different departments of the TU Darmstadt and Rolls-Royce Deutschland (RRD). Therefore, the numerical basis and starting point of this thesis was given to be the CFD-solver used by the combustor development group at RRD. At the moment the incompressible CFD-solver “PRECISE-Unstructured" [5] is used, next to other tools, for combustor calculations at RRD. It is equipped with various combustion models for different types of flames. The presumed probability density function / flamelet generated manifold (PPDF-FGM) model (section 2.4.3) is also available and to be used to account for turbulence-chemistry interaction and combustion modeling. Based on the code at hand and due to the high complexity not all favored modeling techniques could be used. For example, reactive LES was not sufficiently validated in the code at the start of the project so that RANS modeling had to be used, knowing that LES is advantageous when modeling complex turbulent flows and mixing phenomena as present in combustors. However, choosing RANS over LES also has some advantages that are discussed in section 2.2.1. The focus of this work laid on the extension of the incompressible code at hand for the compressible domain, to be able to conduct reactive, integrated simulations of the interacting systems in *one* numerical domain with *one* solver.

Outline of this Thesis

Due to the nature of the CTI system a number of topics needed to be considered: Compressibility, in context of its nature (turbulence) and in context of the numerics. Com-

[4] Deutsche Forschungsgemeinschaft, german largest research funding organisation

[5] Shall be referenced as PRECISE-UNS in the rest of this book

bustion and its modeling, especially in context of the new compressible algorithm for the CFD-solver. Consequently this thesis is structured as follows:

In the second chapter an introduction is given to the basic theories of CTI. The fundamental equations for compressible fluid flow are given and their various terms are discussed. The nature of turbulence and modeling techniques within the context of numerical simulation are explained. The kinetic theory of combustion is introduced as well as the calculation of reaction temperature and products. The fundamental gas dynamic relations for compressible flow are given.

The third chapter is concerned with the fundamentals of numerical simulations. Introducing the Finite Volume method and its implementation in the used code, the implicit scheme used to solve the algebraic equations is explained. Section 4 is devoted to the extended algorithm implemented into the code. Special attention is given to the various boundary conditions, which need different treatment in compressible algorithms compared to the former incompressible solver.

In chapter 5 a newly developed algorithm for coupling the pressure based FGM model with the extended compressible solution algorithm is presented.

Various verification and validation test cases are presented in chapter 6. In the first four sections the results are compared to analytical solution or experimental values. In Section 5.5 application of the new solver to a real NGV geometry and to a model GT combustor are shown.

In chapter 7 finally an integrated simulation of CTI is presented. It serves to demonstrate the capability of the new solver for simulating the combustion and flow in CTI context and related geometry.

Chapter 8 concludes this thesis and gives an outlook on future work on this project.

2 Turbulent Combustion within Compressible Flow Context

Three main topics have to be considered within this thesis. First, the numerical simulation of the turbulent flow needs to be discussed. Turbulence as itself is a complex field of science, which is approached in many different ways. The commonly used methods of modeling turbulent flows are addressed in section 2.2.
Combustion is the next main field considered in this thesis. Depending on the type of flame and flow, different modeling techniques exist for calculating the key aspects of a combustion process. Those are the flame's temperature and the various reaction products, e.g. CO_2, NO_x, etc. In section 2.3 a short introduction into the field of combustion shall be given, while the modeling technique used for this thesis is explained in more detail. Here, the interaction between the chemical reaction and the turbulent flow needs special consideration. Different methods are available to account for interaction, but only the used procedure shall be explained in detail in section 2.4. Thirdly, compressibility needs to be considered. The flow through an NGV is influenced by compressible effects and gas dynamics have to be taken into account. Section 2.5 gives an introduction into the basic concepts needed for the simulation of compressible flow.

2.1 Navier-Stokes Equations for Reacting Compressible Flow

To describe a reacting, compressible fluid flow the following set of equations must be solved: The equation for the balance of mass, the equation for the balance of momentum, the energy equation, and one conservation equation for each species k of a total number N, which are taking part in the reaction.

$$\frac{\partial \rho}{\partial t} + \frac{\partial}{\partial x_i}\left(\rho u_i\right) = 0 \tag{2.1}$$

$$\frac{\partial}{\partial t}\left(\rho u_i\right) + \frac{\partial}{\partial x_j}\left(\rho u_j u_i\right) = -\frac{\partial p}{\partial x_i} + \frac{\partial t_{ij}}{\partial x_i} + \rho \sum_{k=1}^{N} Y_k \, f_{k,j} \tag{2.2}$$

$$\frac{\partial}{\partial t}\left(\rho E\right) + \frac{\partial}{\partial x_j}\left(\rho u_j H\right) = -\frac{\partial q_j}{\partial x_j} + \frac{\partial}{\partial x_j}\left(u_i t_{ij}\right) + \rho \sum_{k=1}^{N} Y_k \, f_{k,j}(u_j + V_{k,j}) + \dot{\omega}_T + \dot{Q} \tag{2.3}$$

$$\frac{\partial}{\partial t}\left(\rho Y_k\right) + \frac{\partial}{\partial x_j}\left(\rho(u_j + V_{k,j})Y_k\right) = \dot{\omega}_k \tag{2.4}$$

The stress tensor t_{ij} is defined as:

$$t_{ij} = 2\mu S_{ij} - \frac{2}{3}\mu\frac{\partial u_k}{\partial x_k}\delta_{ij} \tag{2.5}$$

with the strain rate S_{ij} given by:

$$S_{ij} = \frac{1}{2}\left(\frac{\partial u_i}{\partial x_j} + \frac{\partial u_j}{\partial x_i}\right) \tag{2.6}$$

q is the energy flux, composed of heat diffusion due to temperature gradients, expressed by Fourier's Law, and diffusion of species with different enthalpies.

$$q_j = -\lambda\frac{\partial T}{\partial x_j} + \rho\sum_{k=1}^{N} h_{s,k}\, Y_k\, V_{k,j} \tag{2.7}$$

λ denotes the heat conductivity. While the influence of volume forces f_j (gravity g or other volume forces) on species k is commonly neglected for non-reactive flows, it is not to be neglected in combustion calculation. It is represented by the term:

$$\rho\sum_{k=1}^{N} Y_k\, f_{k,j} \tag{2.8}$$

V_k denotes the diffusion velocity of species k. If only gravity is considered as volume force the term simplifies, as the sum of all mass fractions Y_k is equal to unity, to:

$$\rho\sum_{k=1}^{N} Y_k\, f_{k,j} \hat{=} \rho g_j \tag{2.9}$$

This term is commonly found in literature in the momentum equation. $\dot{\omega}_k$ in (2.4) is the reaction rate of species k while $\dot{\omega}_T$ in (2.3) is the heat release due to the combustion process, given by:

$$\dot{\omega}_T = -\sum_{k=1}^{N} \Delta h^0_{f,k}\dot{\omega}_k, \tag{2.10}$$

where $\Delta h^0_{f,k}$ is the formation enthalpy of species k. $\dot{Q}$ is a heat source such as an ignition spark. All these terms are relevant for the calculation of combustion processes, hence its treatment is to be explained in section 2.3.

E is the total specific energy, which is the sum of the internal energy e and the kinetic energy.

$$E = e + \frac{1}{2} u_i u_i \tag{2.11}$$

H is the total specific enthalpy, which is the sum of the specific enthalpy h and the kinetic energy.

$$H = h + \frac{1}{2} u_i u_i \tag{2.12}$$

The specific enthalpy h contains the internal energy plus the volumetric energy of the fluid:

$$h = h_s + \Delta h_f^0 \tag{2.13}$$

Energy and enthalpy are linked via

$$h = e + \frac{p}{\rho}. \tag{2.14}$$

The temperature difference is given by

$$\Delta T = \frac{\Delta h}{\int_{T_0}^{T} c_p(T) dT}, \tag{2.15}$$

where c_p is the specific heat constant at constant pressure. It depends on temperature and pressure. By inserting equation (2.15) into equation (2.12) the temperature can be calculated as a function of H, using an averaged $\overline{c_p} = \int_{T_0}^{T} c_p(T) dT$:

$$T = \frac{H - \frac{1}{2} u_i u_i}{\overline{c_p}} \tag{2.16}$$

Boundary Conditions for the Navier-Stokes Equation

The boundary conditions for a reactive system include the pressure, velocities given at the inlet and mixture fractions of species at inlet. Furthermore the temperatures of the entering fluids needs to be prescribed. In a compressible context total conditions for pressure and temperature have to be known and treated as explained in section 4.4.

2.2 Turbulence

A flow may either be characterized as laminar or turbulent. In case of a laminar flow, disturbances that are induced on the flow are damped by its viscosity. In turbulent flows, these disturbances are only attenuated. The dimensionless Reynolds number quantifies the quotient between inertial forces and viscous forces:

$$Re = \frac{U \cdot L}{\nu} \tag{2.17}$$

U and L are a characterizing length and velocity scale, respectively. If the Reynolds number is higher than a critical number Re_{crit} the flow is said to be turbulent. Technical flows are in the majority of the cases turbulent in nature. The velocity field underlies arbitrary fluctuations. These fluctuations are introduced by disturbances as mentioned above. Sources can be obstacles, volume forces or walls. Turbulent flow is commonly described as chaotic, stochastic, and random, as well as inheriting vorticity [96]. The turbulent flow structure is figuratively described by so called 'eddies', which are areas in the fluid that have the same vorticity and can be identified separately from the neighboring eddies. Those eddies are of different size and life-time. Thus length- and time-scales are considered to characterize turbulent flow. Depending on the size of an eddy, it is energy containing, energy conserving or energy dissipating. The turbulent energy spectrum (figure: 2.1) classifies the turbulent structures within a flow into corresponding regimes.

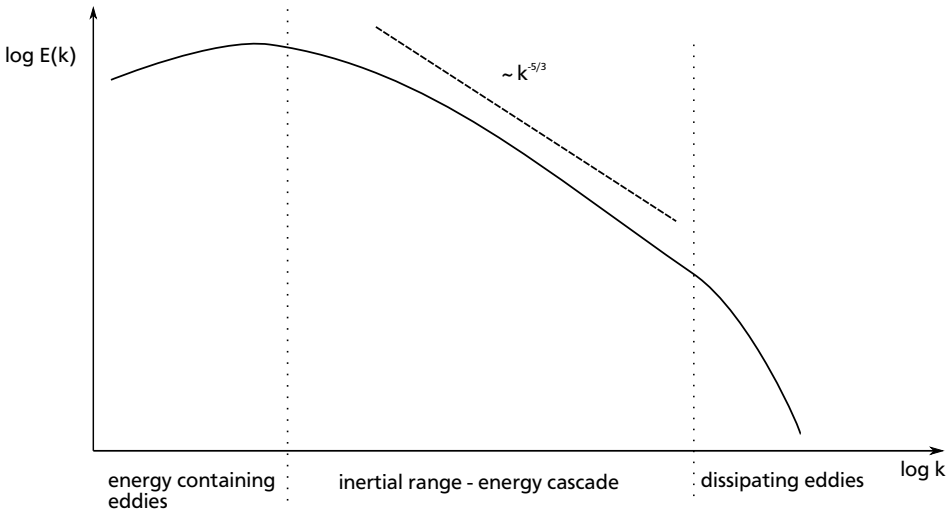

Figure 2.1.: Energy spectrum for turbulent flows and assignment of eddies, k - turbulent kinetic energy

The energy within a flow is transferred consecutively from the larger to the smaller eddies until it reaches the smallest eddies, where it is dissipated into heat. This process

is called energy cascade. The length scale of the smallest eddies is the so-called Kolmogorov length $\eta = \left(\frac{\nu^3}{\epsilon}\right)^{1/4}$. The time scale of these smallest eddies is the Kolmogorov time-scale $\tau_\eta = \left(\frac{\nu}{\epsilon}\right)^{1/2}$ analogously. The size of the largest eddy and the size of the smallest eddy are correlated. The higher the Reynolds number, the larger the biggest eddy and the smaller the smallest eddy becomes. The correlation is a function of the Reynolds number, given by:

$$\frac{\eta}{L} \approx Re^{-3/4} \tag{2.18}$$

The correlation of the smallest time scale τ_η to the integral time scale τ is also a function of the Reynolds number:

$$\frac{\tau_\eta}{\tau} \approx Re^{-1/2} \tag{2.19}$$

Direct Numerical Simulation

Analytic solutions to the Navier-Stokes equations are hard to find for turbulent flows. A more realistic approach is the numerical computation of the solution. For directly solving the equations, all movement within the flow needs to be resolved as every smallest fluctuation needs to be considered to capture all influence on the behavior of the flow. At the same time, to calculate the flow in a jet-engine for example, the whole domain needs to be enclosed into the simulation to capture all influences from the boundaries of the domain. This procedure of resolving every smallest eddy is called Direct Numerical Simulation (DNS), which requires a vast amount of computing resources. Consider for example an annular combustor with a volume of approximately $0.024\,\mathrm{m}^3$ (if only a segment is calculated and periodic boundary conditions are assumed). The Reynolds number in this case is of the order O(6), assuming velocities of around $100\,\mathrm{m/s}$ and a height of the combustor of $0.3\,\mathrm{m}$, using equation (2.17). If the biggest correlated motion (eddy) was assumed to be as big as half the combustor's height, the smallest eddies would be approximately $2\,\mu\mathrm{m}$ in size, according to correlation (2.18). If the whole domain (assuming roughly $0.3\,\mathrm{m} \times 0.2\,\mathrm{m} \times 0.4\,\mathrm{m}$ for height, depth and length) was resolved with cells that have an edge length of $2\,\mu\mathrm{m}$ it follows that for a DNS in a combustor of a jet-engine the needed number of cells would be approximately equal to $3 \cdot 10^{15}$ cells. The time-step size depends at the same time on the Courant number CFL $= \frac{u\Delta t}{\Delta x}$ [27] and would be in this example at approximately $2 \cdot 10^{-8}$, assuming that a CFL number of 1 is necessary to obtain a stable simulation. This rough estimation easily illustrates that with today's resources it is not possible to compute the fluid flow within a combustor (and the successive NGV) of a jet engine with DNS within a reasonable time.

2.2.1 Modeling Turbulent Flow

Large Eddy Simulation

LES modeling offers an alternative method to calculate the turbulent flow in a jet engines combustor. For LES only the bigger scales of the turbulent fluctuations are resolved in time, while the influence of the smaller scales on the velocity field is modeled. The needed computational resources are therefore decreased compared to using DNS. This simulation technique in context of reactive flows is part of today's research and sometimes also used in industry. Many flow-through cycles need to be computed to gain a meaningful statistic for the mean flow, because it is a time-resolving method. At the same time instantaneous motion can directly be made visible. For investigating transient effects between combustor and NGV in a jet engine it seems to be the first choice. The quality of a LES depends strongly on the resolution of the domain. Fine meshes for flow with high Reynolds numbers are necessary. The needed time-step size is often very small. Even if needed resources are smaller than those for a DNS, it is still a very time consuming tool. Influence of proper numerical boundary conditions on the solution are highly discussed within the scientific community.

RANS Modeling

For compressible flow between vanes, where it is highly influenced by the wall boundary, the common tool in industry and research communities is still RANS modeling. RANS stands for Reynolds Averaged Navier Stokes equation and gives it name to the third modeling technique to be considered and used in this thesis. While in LES the time-resolved equations are considered, in RANS modeling the temporal fluctuations are averaged and the influence of the turbulent movement of the eddies on the flow is modeled entirely.

2.2.2 Favre Averaged Navier Stokes Equations

In the following paragraph all terms concerning combustion and involved species are omitted to simplify the introduction of turbulence modeling. They are to be revisited in section 2.3. All modeling is evolved for the non-reacting compressible equations. For incompressible flows Reynolds Averaged Navier-Stokes equations are commonly used. For compressible flows the Favre Averaged Navier Stokes (FANS) equations are favored, as two kinds of fluctuations are to be considered [136]. Firstly, fluctuations in time that are also known from incompressible flow modeling. Here, using Reynolds decompo-

sition, the instantaneous value of a variable is split up into the temporal mean and a fluctuating part:

$$\Phi = \bar{\Phi} + \Phi' \tag{2.20}$$

The temporal mean of the fluctuation is zero: $\overline{\Phi'} = 0$. If all variables in a compressible flow were split up in this way, complex correlations of velocity-density-fluctuations in the RANS equations would arise, which are difficult to model. One reason for this instance is the limited accessibility of those correlations via experiments. Thus, Favre's density weighted averaging is used as well. It is defined as

$$\tilde{\Phi} = \frac{\overline{\rho\Phi}}{\overline{\rho}} \tag{2.21}$$

and again the instantaneous value is split up into a mean (density-mean) and a fluctuating part:

$$\Phi = \tilde{\Phi} + \Phi'' \tag{2.22}$$

The temporal mean of the fluctuation is unequal to zero $\overline{\Phi''} \neq 0$, but it holds that: $\overline{\rho\Phi''} = 0$. Thus, Favre averaging eliminates density fluctuations from the averaged equations [136].

Reynolds decomposition is used for density and pressure and Favre decomposition is used for velocity, enthalpy, energy and temperature.

$$\rho = \bar{\rho} + \rho' \; ; \; p = \bar{p} + p' \; ; \; u = \tilde{u} + u'' \; ; \; h = \tilde{h} + h'' \; ; \; e = \tilde{e} + e'' \; ; \; T = \tilde{T} + T'' \tag{2.23}$$

Substituting (2.23) into the equations (2.1) - (2.3) and averaging in time, the so-called FANS equations for mass, momentum and energy are obtained. The total specific enthalpy shall be used for balancing the energy of the reacting system, hence correlation (2.14) is used to substitute E in the energy equation:

$$\frac{\partial \bar{\rho}}{\partial t} + \frac{\partial}{\partial x_i}\left(\bar{\rho}\tilde{u}_i\right) = 0 \tag{2.24}$$

$$\frac{\partial}{\partial t}\left(\bar{\rho}\,\tilde{u}_i\right) + \frac{\partial}{\partial x_j}\left(\bar{\rho}\tilde{u}_j\tilde{u}_i\right) = -\frac{\partial \bar{p}}{\partial x_i} + \frac{\partial}{\partial x_j}\left(\bar{t}_{ij} + \tau_{ij}\right) \tag{2.25}$$

$$\frac{\partial}{\partial t}\left(\bar{\rho}H\right) + \frac{\partial}{\partial x_j}\left(\bar{\rho}\tilde{u}_j H\right) = \frac{\partial}{\partial x_j}\left[-q_{L_j} - q_{T_j} + \overline{t_{ji}u_i''} - \overline{\rho u_j''\frac{1}{2}u_i''u_i''} + \tilde{u}_i\left(\bar{t}_{ij} + \tau_{ij}\right)\right] + \frac{\partial \bar{p}}{\partial t} \tag{2.26}$$

The total energy and enthalpy read:

$$H = \tilde{h} + \frac{1}{2}\tilde{u}_i\tilde{u}_i + k \quad E = \tilde{e} + \frac{1}{2}\tilde{u}_i\tilde{u}_i + k \tag{2.27}$$

A new term k is introduced that is the turbulent kinetic energy, which is the kinetic energy that exists due to the turbulent, fluctuating motion of the fluid. It is defined as:

$$k = \frac{1}{2}\overline{u_i' u_i'} \tag{2.28}$$

For k a transport equation can be derived that reads:

$$\bar{\rho}\frac{\partial k}{\partial t} + \rho\tilde{u}_j\frac{\partial k}{\partial x_j} = \tau_{ij}\frac{\partial \tilde{u}_i}{\partial x_j} - \overline{t_{ij}\frac{\partial u_i''}{\partial x_j}} + \frac{\partial}{\partial x_j}\left(\overline{t_{ij}u_i''} - \overline{\rho u_j''\frac{1}{2}u_i''u_i''} - \overline{p'u_j''}\right) - \overline{u_i''}\frac{\partial p}{\partial x_i} + \overline{p'\frac{\partial u_i''}{\partial x_i}} \tag{2.29}$$

The turbulent stress tensor τ_{ij}, the turbulent heat flux q_{T_j}, molecular diffusion and turbulent transport of energy $\overline{t_{ji}u_i''} - \overline{\rho u_j''\frac{1}{2}u_i''u_i''}$ contain correlations of fluctuating quantities that can not directly be calculated. These correlations need to be modeled, which is called the turbulence closure.
The next section will give a short introduction into modeling these terms. It has to be mentioned that it is still an open field of science so that new modeling approaches or specific models are introduced every year.

2.2.3 Modeling the Turbulent Stress Tensor

Accounting for turbulence by Reynolds and Favre decomposition and averaging will introduce several new terms into the set of equations. The tensor τ_{ij} is the so called Favre averaged turbulent stress tensor:

$$\tau_{ij} = -\overline{\rho u_i'' u_j''}. \tag{2.30}$$

Commonly it is modeled using the Bousinesq Hypothesis analogous to the laminar shear tensor t_{ij} (2.5):

$$-\overline{\rho u_i'' u_j''} = \mu_T\left(2S_{ij} - \frac{2}{3}\frac{\partial u_k}{\partial x_k}\delta_{ij}\right) - \frac{2}{3}\bar{\rho}k\delta_{ij} \tag{2.31}$$

μ_T is the turbulent viscosity which is the main term in RANS and FANS to be modeled. There exist several approaches of different kind and order. In general it can be distinguished between Reynolds Stress Modeling (RSM), linear eddy viscosity, and nonlinear eddy viscosity modeling. In RSM the turbulence closure is received one level higher, as for all components of the Reynolds stress tensor τ_{ij} a transport equation is solved [71].

While RSM models are known to improve prediction especially of swirling flow, one of the main drawbacks is the increased computing time needed due to the additional transport equations.
Which of these modeling approaches is best used for modeling the flow in context of combustor turbine interaction was in depth evaluated by Jannis Gikadi in [41]. In this thesis only the class of linear eddy viscosity models shall be focused on. Models of different order exist within this class:

One-equation Models

The lowest order are one-equation models. The most prominent example of this class is the Spalart-Allmaras model [121] in which a transport equation for the turbulent viscosity is solved. This equation contains several constants that are set by comparison of calculations to experiments. Thus, this model is fully empirical. For a certain class of applications it is able to predict the flow reasonably good and due to the comparably low need of computing resources it is in favour for the calculation of flows in aerospace engineering like external flow around wings and internal flows in turbomachinery components.

Two-equation Models

The next higher level are the class of two-equation models. The turbulent viscosity is set into correlation to the turbulent energy k and the dissipation ϵ of it:

$$\mu_T \approx \frac{k^2}{\epsilon} \tag{2.32}$$

For both k and ϵ transport equations are solved. Different transport equations are derived using different empirical constants, depending on the kind of model.
One of the earliest two-equation models to be proposed was the one from Launder and Sharma in 1974 [72], which is still the best known and used today. Since then a lot of variants where developed. The realizable k-ϵ model [118], the RNG model [139], the k-ω [135] and the SST k-ω model [81] are the most prominent ones. More-equation-models do also exist, but they are not considered here.

2.2.4 Modeling Turbulent Heat Flux

The diffusive transport of heat is given by the sum of molecular turbulent heat transport q_L and the turbulent heat flux, q_T. The molecular (or laminar) heat flux is approximated

with Fourier's Law, as given above in equation (2.7). The turbulent heat flux is analogously modeled as [136]:

$$q_{Tj} = \overline{\rho u_j'' h''} = -\frac{\mu_T}{Pr_T}\frac{\partial \tilde{h}}{\partial x_j} = -\frac{\mu_T c_p}{Pr_T}\frac{\partial \tilde{T}}{\partial x_j} \tag{2.33}$$

Pr_T is the turbulent Prandtl number for temperature. Mostly this value is assumed to be 0.89 or 0.9, in case of a boundary layer flow. For cases, where shock is involved and where the heat transfer rate varies strongly throughout the domain a variable value is more appropriate [128]. This is however at the moment not implemented in the code.

2.2.5 Standard k-ϵ Model

In the following the modeling techniques within PRECISE-UNS are to be discussed. The incompressible version incorporates the standard k-ϵ model for RANS. Here, the turbulent viscosity is given by:

$$\mu_t = \rho C_\mu \frac{k^2}{\epsilon} \tag{2.34}$$

The k and ϵ-equation in the standard k-ϵ model read as follows:

$$\frac{\partial}{\partial t}(\bar{\rho}k) + \frac{\partial}{\partial x_j}\left(\bar{\rho}k\, u_j\right) = \frac{\partial}{\partial x_j}\left[\left(\mu + \frac{\mu_t}{\sigma_k}\right)\frac{\partial k}{\partial x_j}\right] - \rho\widetilde{u_i'' u_j''}\frac{\partial \tilde{u}_i}{\partial x_j} - \epsilon \tag{2.35}$$

$$\frac{\partial}{\partial t}(\bar{\rho}\epsilon) + \frac{\partial}{\partial x_j}\left(\bar{\rho}\epsilon u_j\right) = \frac{\partial}{\partial x_j}\left[\left(\mu + \frac{\mu_t}{\sigma_\epsilon}\right)\frac{\partial \epsilon}{\partial x_j}\right] - \frac{\epsilon}{k}\left(C_{\epsilon 1}\rho\widetilde{u_i'' u_j''}\frac{\partial \tilde{u}_i}{\partial x_j} + C_{\epsilon 2}\bar{\rho}\epsilon\right) \tag{2.36}$$

The coefficients used are given in table 2.1 and are the so-called standard coefficients proposed in [72]. The coefficients are calibrated for shear flow. In these kinds of flow the diffusion processes are determined by the shear effects. In stagnation points the production of turbulent kinetic energy is damped due to the wall. This damping effect cannot be accounted for with the standard k-ϵ model. Furthermore does the standard k-ϵ model exhibit the well known Turbulent Round-Jet/Plane-Jet anomaly, i.e. the spreading rate of a three-dimensional jet is underestimated [94]. Additionally, the influence of streamline curvature on turbulence is not accounted for in the model.

Table 2.1.: Coefficients of the standard k-ϵ model

C_μ	C_{ϵ_1}	C_{ϵ_2}	σ_k	σ_ϵ
0.09	1.44	1.92	1	1.3

The flow that is present when considering CTI, is dominated by swirling flow in the front part of the combustor, where the flame is stabilized by a swirl-induced recirculation. In front of the NGV a stagnation point is present. Within the NGV the flow direction is altered nearly up to 90°. The main features of the flow in CTI are therefore those that are only poorly predicted with the standard k-ϵ model. Therefore modeling turbulence for CTI applications was investigated in the context of this thesis and an alternative model was chosen and implemented into PRECISE-UNS.

2.2.6 Turbulence Modeling for Combustor-Turbine Interaction

An investigation was conducted on turbulence simulation for CTI in RANS context [41]. Several constraints were given. The alternative model to the standard k-ϵ for the simulation of CTI should improve the mentioned shortcomings, but at the same time keep the needed computing time as low as possible. Models using more than two transport equations like the RSM are too time consuming. While the RNG model and the realizable model by Shih [118] both show similar improved behavior compared to the standard k-ϵ model, the latter one was chosen, as it was reported to be less sensitive to instabilities in steady-flow calculations, which could lead to divergence [41].
One of the main remaining problems while using RANS for turbulent flow calculations is the difficulty to model mixing. In modern jet engine's combustors, which use the RQL principal, mixing is a very important process. To improve the modeling of mixing phenomena one should use LES. As LES was not chosen in this thesis due to the reasons mentioned before (section 2.2) it must be kept in mind, that for future work this is still an open field for improvements.

2.2.7 Realizable k-ϵ Model

The realizable k-ϵ model contains two main differences compared to the standard version. Firstly, the constant C_μ is variable and secondly the dissipation equation is altered. The main critique from the authors Shih et. al [118] concerning the standard k-ϵ model is the non-realizability of the model. Due to the standard modeling of the Reynolds-stress tensor, it can have negative - i.e. unphysical - values, if the gradient of the velocity is higher than a certain limit. This is the case, if the rotation has a higher impact on the stress than the shear. This is compensated using a function for C_μ that depends on the correlation between shear and rotation, and reads:

$$C_\mu = \frac{1}{A_0 + A_S \frac{kU^*}{\epsilon}} , \tag{2.37}$$

where U^* is given by:

$$U^* = \overline{S_{ij}S_{ij} + \tilde{\Omega}_{ij}\tilde{\Omega}_{ij}}\,, \tag{2.38}$$

and $\tilde{\Omega}$ is the mean rotation tensor in a non rotating frame. While in the standard formulation C_μ is always 0.09, which is actually only the case for flat plate flow, the variable formulation in (2.37) will lead to more realistic values for C_μ, which are given by Rodi for different flows in [105].

In the standard k-ϵ model the production terms of the k and ϵ equations are assumed to be proportional to each other. Therefore, they are modeled with the same ansatz. For the realizable k-ϵ model the ϵ equation is derived from the whirl-transport equation while proportionality between anisotropy-tensor and shear rate is assumed. The new ϵ equation reads:

$$\frac{\partial}{\partial t}(\bar{\rho}\epsilon) + \frac{\partial}{\partial x_j}\left(\bar{\rho}\epsilon u_j\right) = \frac{\partial}{\partial x_j}\left[\left(\mu + \frac{\mu_t}{\sigma_\epsilon}\right)\frac{\partial \epsilon}{\partial x_j}\right] - \frac{\epsilon}{k}\left(C_1\rho\widetilde{u_i''u_j''}\frac{\partial \tilde{u}_i}{\partial x_j} - C_2\bar{\rho}\frac{\epsilon^2}{k+\sqrt{\nu\epsilon}}\right), \tag{2.39}$$

where $S = \sqrt{2S_{ij}S_{ij}}$ is a measure of turbulent energy production due to strain. C_1 is given by

$$C_1 = \max\left[0.43\,,\ \frac{\eta}{\eta+5}\right], \tag{2.40}$$

where η determines the ratio between turbulent kinetic energy production and dissipation with

$$\eta = \frac{S\,k}{\epsilon}. \tag{2.41}$$

The constants used for the realizable k-ϵ model are given in table 2.2.

Table 2.2.: Coefficients of the Realizable k-ϵ model

C_1	C_2	A_0	σ_k	σ_ϵ
eq.(2.40)	1.9	4.04	1.0	1.2

2.2.8 Compressibility Effects in Turbulence Modeling

The models introduced so far are all derived for incompressible flow. For compressible flow with increasing Mach number production of turbulent energy decreases. This influence of pressure dilatation is modeled commonly by using Sarker's [111] compressibility correction, which is treated as an additional source term in the k equation:

$$Y_M = 2 \cdot \rho\,\epsilon\,\frac{k}{\gamma\,R\,T} \tag{2.42}$$

This term helps to model the observed decrease in spreading rate with increasing Mach number for compressible mixing and shear flows [128].

2.2.9 Wall Treatment

The turbulence models given above are so-called High-Reynolds number (High-Re) models. They are valid only for flows with high Reynolds numbers. In the vicinity of a wall the flow is decelerated to the wall's velocity due to adhesive forces. A so-called boundary-layer will form.[1] A sketch of the velocity distribution within such a boundary layer is given in figure 2.2.

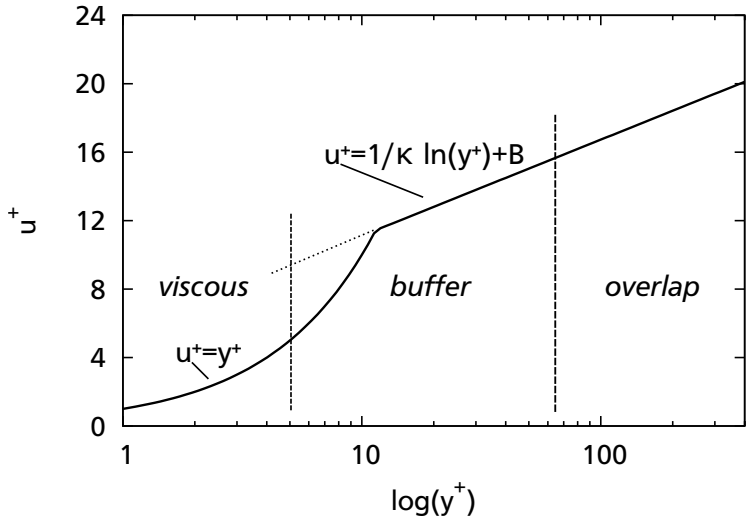

Figure 2.2.: Velocity distribution within turbulent boundary layer as function of wall distance

The boundary layer can be divided into three regions: The overlap layer, which is sometimes called logarithmic layer due to the logarithmic relation between velocity and distance to the wall, the viscous sublayer (sometimes also called laminar layer due to its laminar nature) and the region in between - the buffer layer. A dimensionless wall distance (also known as wall coordinate) y^+, can be defined:

$$y^+ = \frac{\rho u_\tau y}{\mu}, \tag{2.43}$$

[1] An extensive compendium about boundary layer theory is Schlichting's famous book "Grenzschicht-Theorie" [112]. Interestingly on its back cover it is claimed to contain "unerschöpfliche Informationen" (engl.='inexhaustible information'). That is indeed a lot of information on boundary layers on a countable number of pages and therefore in this thesis the part on boundary layer theory is kept very short.

where u_τ is the "wall friction velocity", which is the characteristic velocity of a turbulent flow for a given "wall shear stress" τ_w, defined as:

$$u_\tau = \sqrt{\frac{\tau_w}{\rho}}. \tag{2.44}$$

With this wall friction velocity a dimensionless velocity can be defined

$$u^+ = \frac{\bar{u}_t}{u_\tau}, \tag{2.45}$$

where $\bar{u}_t$ denotes the velocity component tangential to the wall. The different boundary layer regimes can be related to different values of y^+ [112], while a different law for the dimensionless velocity u^+ holds for each of the regimes:

viscous sublayer	0	$\leq y^+$	< 5	$u^+ = y^+$
buffer layer	5	$< y^+$	< 70	
overlap layer	70	$< y^+$		$u^+ = \frac{1}{\kappa} \ln y^+ + B$

Viscous effects are present in all regimes that damp the turbulent kinetic energy to a different extent. The blocking of the wall-normal velocity component has similar effects. The assumption of high Reynolds number is not valid anymore and the calculation of the turbulent viscosity μ_T needs to take those damping effects into account. For k-ϵ based turbulence models two possibilities exist: Using a low-Reynolds number (Low-Re) model, or using wall functions, i.e. the so-called "law-of-the-wall".

Low-Reynolds-Number Modeling

A damping term is added to the k-equation in Low-Re k-ϵ models. Often, it is a function of the wall distance of the near-wall cells and is added using a blending function, which depends on the wall distance y^+. An overview of such Low-Re number models is given in [88]. Calculation of the wall distance y^+ for all cells in a flow domain is a difficult task in complex geometries using unstructured grids. Therefore, a number of models were developed, in which the blending functions are independent of the wall distance [82, 59].

One disadvantage of Low-Re models is the necessity to refine the grid near the wall, so that the centre of the wall-nearest cell lies within the viscous sublayer of the flow's boundary layer ($y^+ \approx 1$). For modeling a combustor and the adjoining NGVs for an integrated combustor-turbine simulation a large amount of cells is necessary for discretizing the domain. If the boundary layer was to be resolved for Low-Re modeling, this number would increase excessively. While the passage around one stator vane is commonly resolved with 1.2 million cells for using Low-Re modeling, using wall functions will decrease the needed amount of cells to around 600,000 cells for the same

passage. This factor of two is one of the reasons to use High-Re modeling coupled with the “law-of-the-wall” for this thesis.

Wall Function

To bridge the viscous sublayer and the buffer layer (which is the most difficult layer to calculate) the wall function can be used. The velocity in the logarithmic region is given by:

$$u^+ = \frac{\bar{u}_t}{u_\tau} = \frac{1}{\kappa} \ln y^+ + B \tag{2.46}$$

B is given from measurements as well as the Karman constant $\kappa = 0.41$. Local energy equilibrium, i.e. production and dissipation of kinetic energy are almost equal in a flow near a solid boundary, is the main assumption of the law-of-the wall. It follows, that

$$u_\tau = C_\mu^{1/4} \sqrt{k}. \tag{2.47}$$

Using the definition of the friction velocity and equations (2.46) and (2.47), one ends up with a formulation for the wall shear stress that incorporates this assumption:

$$\tau_w = \rho C_\mu^{1/4} \kappa \sqrt{k} \frac{\bar{u}_t}{\ln(y^+ e^{\kappa B})} \tag{2.48}$$

With the help of τ_w the adhesive force of the wall can be calculated, that acts on the first cells and resembles the slackening of flow-speed that is induced by the viscous sublayer and buffer layer together. Therefore, it is important that the center of the first cell is in an according distance to the wall, which is usually around $y^+ \approx 35$. But wall functions due to its nature also suffer drawbacks. It is by definition impossible to calculate detached flow, as the law of the wall is derived for attached flow (actually, one probably will end up with a converged simulation and a solution, but this will not be physically correct). Detaching is a very common feature of the flow through an NGV. For aerodynamic design of a stator therefore, Low-Re modeling is to be preferred. Nonetheless, in the present situation it is assumed, that whether or not the flow through the NGV detaches does not have a major influence on the combustor-turbine interaction. This assumption may be reviewed in future studies.

2.3 Combustion

Combustion is an exothermic reaction of two or more reactants (fuel and oxidizer). In this reaction a flame is present, which is the region where the reacting process is taking place, the reactants are converted into products and heat is released. In general, one may distinguish between two different kind of combustion processes. Firstly, the non-premixed combustion, where oxidizer and a fuel-gas mixture that is inflammable are separated before the combustion. They are mixed within the reaction zone. The mixing due to diffusion defines the progress of the combustion process, as the mixing is creating a flammable region between oxidizer and fuel-gas mixture. Non-premixed flames are also called diffusion flames, as the progress of the reaction is controlled by the mixing process.
Secondly, there is premixed combustion, where oxidizer and fuel are perfectly mixed before they enter the reaction zone. Here, the flame migrates through the gas mixture with its characteristic flame velocity that depends on the type of fuel and the air-to-fuel ratio. Modern stationary gas turbines often use premixed combustion. A concise introduction in the different types of flames and their characteristics can be found in [132].
Before having a closer look on the combustion reaction, its calculation, and modeling, the equations that define the fluid flow shall be revisited to identify the influence of combustion on them.

2.3.1 Conservation Equations

The terms in equations (2.1-2.4) that evolve from combustion shall be revisited. Favre averaging needs to be applied to the chemical terms that were left out in section 2.2. The equation for mass conservation (2.1) does not need any special consideration as there is no mass produced or destroyed due to combustion processes. Momentum, energy and species conservation are to be discussed in the following sections.

Conservation of Momentum

In the equation of conservation of momentum the influence of body forces on the different species is taken into account by $\rho \sum_{k=1}^{N} Y_k \, f_{k,j}$. This term is often neglected for deflagrations. The Favre averaged form is given by:

$$\bar{\rho} \sum_{k=1}^{N} \tilde{Y}_k \, f_{k,j}. \tag{2.49}$$

Another influence from combustion on the momentum equation stems from the viscosity μ. Recalling equation 2.25, the diffusive transport is modeled $\frac{\partial}{\partial x_j}\left(\bar{t}_{ij} + \tau_{ij}\right)$, while using the gradient diffusion hypothesis for t_{ij} and τ_{ij} (see equations (2.5) and (2.31)). The laminar viscosity is a function of the temperature, T. The influence of typical temperatures for combustion processes on the viscosity of air is shown in figure 2.3.

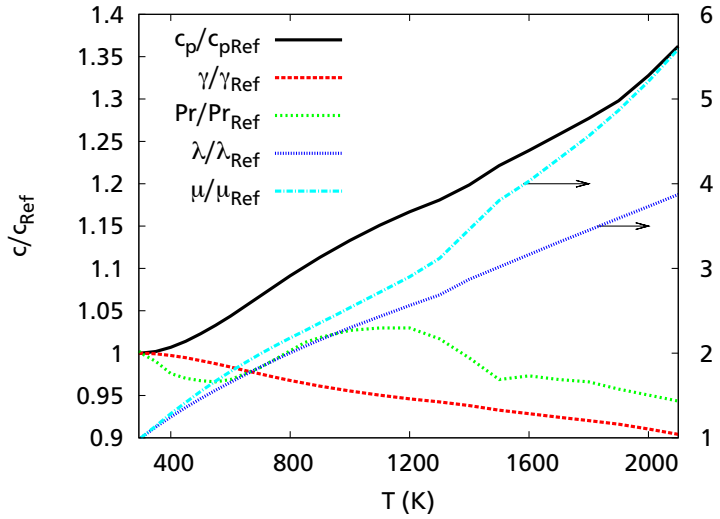

Figure 2.3.: Temperature dependence of gas constants/properties, the reference values are values at 293.15 K, data taken from [40]

The density also changes due to combustion. It will change from the unburnt to the burnt state with a ratio of around 8:1, as the density depends linearly on the temperature.

Conservation of Energy

An overview on the various forms of energy equations may be found in [91].
The total chemical enthalpy is defined as:

$$H = h_s + \sum_{k=1}^{N} \Delta h^0_{f,k} Y_k + \frac{1}{2} u_i u_i \tag{2.50}$$

Favre averaging of equation (2.3) yields:

$$\begin{aligned} \frac{\partial}{\partial t}(\bar{\rho}\tilde{H}) + \frac{\partial}{\partial x_j}(\bar{\rho}\tilde{u}_j\tilde{H}) =& \frac{\partial \bar{p}}{\partial t} + \frac{\partial}{\partial x_j}\left(\tilde{u}_j(\bar{t}_{ij} + \tau_{ij})\right) + \frac{\partial}{\partial x_j}\left(\lambda\frac{\partial \bar{T}}{\partial x_j} - \bar{\rho}\widetilde{u''_j h''_s}\right) \\ &+ \bar{\rho}\frac{\partial}{\partial x_j}\overline{\sum_{k=1}^{N} f_{k,j} Y_k (u_i + V_{k,j})} \end{aligned} \tag{2.51}$$

where h_s is the sensible enthalpy, defined as

$$h_s = \int_{T0}^{T} c_p \, dT. \tag{2.52}$$

Note that equation (2.51) does not include any heat release source from the combustion. The last term may be omitted as influences due to buoyancy are much smaller than kinetic energy due to high velocities. This formulation does not include any additional terms due to combustion compared to (2.26). Nonetheless, there is some influence on the enthalpy equation, as the temperature changes due to the reaction. The heat capacity c_p of a mixture at constant pressure is:

$$c_p = \sum_{k=1}^{N} c_{p,k} \, Y_k \tag{2.53}$$

$c_{p,k}$ is a function of temperature as shown in figure 2.3.

For a compressible reacting flow a change of temperature may result from combustion or from compressible effects. How to account for both effects numerically, is to be explained in section 5.

Conservation of Chemical Species

The Favre averaged form of conservation of chemical species (equation (2.4)) is:

$$\frac{\partial}{\partial t}\left(\bar{\rho}\tilde{Y}_k\right) + \frac{\partial}{\partial x_j}\left(\bar{\rho}\tilde{u}_j \, \tilde{Y}_k\right) = -\frac{\partial}{\partial x_j}\left(\overline{\rho V_{k,j} Y_k} + \bar{\rho}\widetilde{u_j'' Y_k''}\right) + \tilde{\dot{\omega}}_k \tag{2.54}$$

The diffusive flux of species is split into a turbulent and a laminar part. The turbulent flux of species is modeled with the gradient diffusion assumption:

$$\bar{\rho}\widetilde{u_j'' Y_k''} = -\frac{\mu_t}{Sc_{t,k}} \frac{\partial \tilde{Y}_k}{\partial x_j} \tag{2.55}$$

$Sc_{t,k}$ is the turbulent Schmidt number for species k, and μ_t is the turbulent viscosity obtained from turbulence modeling (see section 2.2). The Schmidt number is defined as:

$$Sc = \frac{\nu}{D} \tag{2.56}$$

It characterizes the relation between convective and diffusive transport. The laminar diffusive flux arises due to different diffusion velocities V_k of species k. In combustion

theory it is common to model the effect of those different velocities using Fick's law by [63]:

$$-\frac{\partial}{\partial x_j}\left(\overline{\rho V_{k,j} Y_k}\right) \approx -\bar{\rho}\bar{D}_k \frac{\partial \tilde{Y}_k}{\partial x_j} \tag{2.57}$$

$\bar{D}_k$ is a mean molecular diffusion coefficient for species k, comparable to the thermal diffusion coefficient λ in (2.7). It is worth to mention that this approximation is only exact for binary diffusion flux without pressure gradient and volume forces and if thermal diffusion is negligible. A broad discussion of this topic can be found in [137]. For multi-species gases more exact formulations can be deduced from kinetic theory given in [51]. Poinsot [91] proposed, that Fick's law should not be used for flames, but the following approximation:

$$\rho\, D \frac{W_k}{W} \frac{\partial X_k}{\partial x_j}, \tag{2.58}$$

where W is the mean molecular weight and X_k is the mole fraction of species k. Nonetheless, for turbulent flames he does indeed use Fick's law for laminar species diffusion. Assuming equal diffusion coefficients for all species $D_k = D$ is a standard assumption for non-premixed flames while also commonly used for premixed combustion calculations [38]. For high Reynolds numbers the influence from preferential diffusion on the effective diffusion of species is negligible compared to turbulent transport [7]. In this thesis Fick's law was used, accordingly.
The last term of (2.54) to be modeled in the balance equation for chemical species is the mean reaction rate of species k, $\tilde{\dot{\omega}}_k$. This term, and the species mass fraction $\tilde{Y}_k$, are to be calculated via chemical kinetics.

2.3.2 Chemical Kinetics and Reaction Mechanisms

In the equation of species conservation (2.4), the source term $\dot{\omega}_k$ is a measure of the change of mass of a substance that is present due to the reaction process within a certain control volume. It changes during the reaction process, as the reactants are converted to products and radicals are formed and consumed during this process. This chemical source term can be calculated by chemical kinetics that describe the temporal evolution of a reaction.
The chemical source term is defined as

$$\dot{\omega}_k = M_k \left(\frac{\partial c_k}{\partial t}\right)_{chem}, \tag{2.59}$$

where M_k is the molar mass of the molecules of species k and $\left(\frac{\partial c_k}{\partial t}\right)_{chem}$ is the reaction rate of species k. For an elementary reaction r of an element A that is present in a number of species S one may write [132]:

$$\sum_{s=1}^{S} \nu_{rs}^{(e)} A_s \xrightarrow{k_r} \sum_{s=1}^{S} \nu_{rs}^{(p)} A_s \,, \tag{2.60}$$

where $\nu_{rs}^{(e)}$ and $\nu_{rs}^{(p)}$ are the stoichiometric coefficients of the educts and products. Now the rate law of formation of species k is given by

$$\left(\frac{\partial c_k}{\partial t}\right)_{chem,r} = k_r \left(\nu_{rk}^{(p)} - \nu_{rk}^{(e)}\right) \prod_{s=1}^{S} c_s^{\nu_{rk}^{(e)}} \,. \tag{2.61}$$

The reaction rate coefficient k_r is given by Arrhenius' law, which is a function of temperature:

$$k_r = A\, exp\left(-\frac{E_a}{RT}\right), \tag{2.62}$$

where E_a is the activation energy that is necessary to start the reaction.

Reaction Equation

The reaction of a combustion can be expressed by the reaction equation. For example the reaction of methane and oxygen is given by

$$\mathrm{CH_4} + 2\,\mathrm{O_2} \longrightarrow \mathrm{CO_2} + 2\,\mathrm{H_2O}\,. \tag{2.63}$$

Such a global reaction equation is given for "stoichiometric" conditions. Stoichiometric means, that all reactants on the left side are converted into products on the right side of the equation. The numbers in front of each molecule given are therefore called stoichiometric coefficients.
During an actual reaction the molecules of the reactants do not directly react with each other to form the molecules of the products. They are instead decomposed into their elements to form intermediate radicals (e.g. OH) or molecules, that are again decomposed and rearranged. This progress of reaction can be visualized by the species concentration profiles of a premixed flame, calculated using Chem1D [24]. In figure 2.4 the mass fraction of molecules along the burning direction is shown.

The re-arrangement of new molecules can be described by sub-reactions, called elementary reactions, taking place during the progress of the global reaction. The number of elementary reactions within a global reaction depends on the number of elements

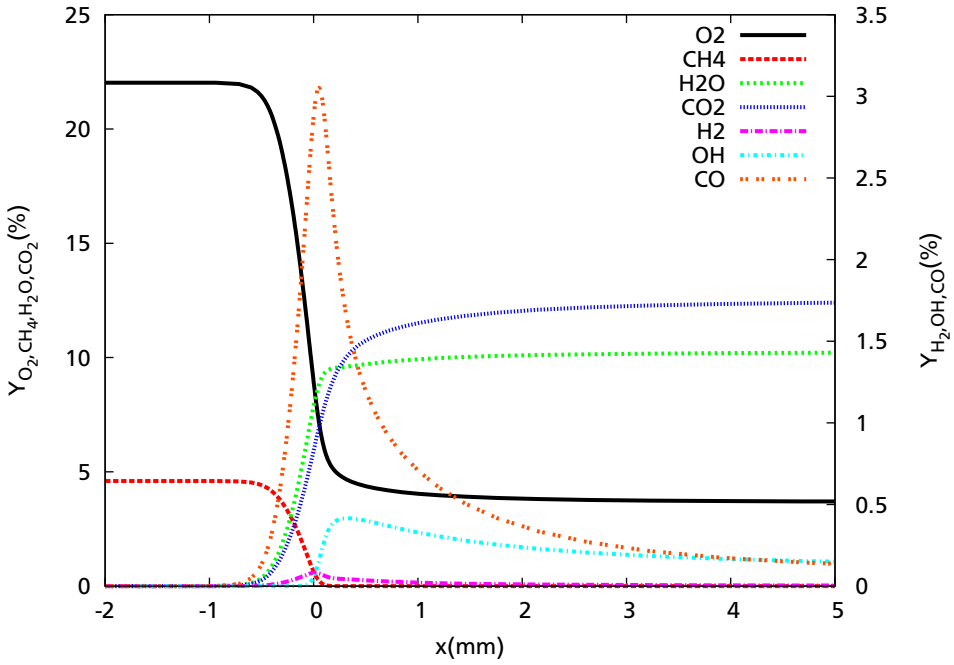

Figure 2.4.: Mass fractions of main and intermediate species of CH4/air combustion, premixed with ϕ = 0.833, along burning direction x; Le = 1, no differential diffusion effects; computed with Chem1D [24].

involved and species formed during the reaction. For the combustion of a relatively "uncomplex" fuel like Hydrogen (H_2) with pure oxygen, given by the global reaction $2\,H_2 + O_2 \longrightarrow 2\,H_2O$, nearly 40 elementary reactions are necessary to capture the chemical processes satisfactorily [132]. For more complex, but still not too complex fuels like methane (CH_4, global reaction as in equation (2.63)) approximately 500 elementary reactions between 50 species are necessary. One well-known mechanism, in which the species and reaction rates of the elementary reactions are listed, is the GRI-MECH 3.0 mechanism [119], commonly used for the calculation of methane combustion.

2.3.3 Reduced Mechanisms

If all species of the detailed reaction mechanism were to be included in the simulation, one equation of the form (2.4) would have to be solved for each species. This exceeds today's computer resources by far. Therefore, it is inevitable to reduce the number of elementary reactions to describe the global reaction process with a manageable number of 'sub-reactions'. Here it is helpful, that some of the reactions taking place are more important to the global reaction process than others. Applying for example the quasi-steady state assumption, one could only take into account those reactions that dominate the reaction process to reach steady state. Reactions, that form intermediate

species, which are quickly consumed again, are not important to reach the final state of the reaction and can be omitted.[2] To keep this short: Some reactions dominate and determine the reaction, others are of less importance for the final state. Several mathematical tools can identify these reactions and create so-called 'reduced mechanisms'. These tools are the sensitivity analysis, the reaction flow analysis and the eigenvector analysis, which are explained in [132].
Still, solving for a reduced number of species with a reduced number of chemical reactions, this process is very time consuming if done during the calculation of the fluid flow. Especially for modeling CTI, where often a large number of grid cells are required to be able to represent the complex geometry, the use of detailed reaction mechanisms would lead to very high computational times.
A way to overcome this problem is to separate the chemical reaction calculation from the fluid flow calculation. In this thesis the methodology of Flamelet Generated Manifolds (FGM) coupled with a Presumed Probability Density Function (PPDF) called PPDF-FGM is used. In the following sections the according theories are explained.

2.3.4 Flamelet Calculation with Chem1D

A one dimensional chemical solver is used to calculate the reaction progress of combustion. In this thesis the solver Chem1D [24] developed at the TU Eindhoven was used. An insight explanation of the theory underlying Chem1D is given by Somers [120], here only a brief introduction shall be given. In Chem1D the following equations are solved:

$$\frac{\partial \rho}{\partial t} + \frac{\partial (\rho u)}{\partial x} = 0 \tag{2.64}$$

is the continuity equation. The energy equation is used in enthalpy formulation for the sum of all N species k.

$$\rho \frac{\partial h}{\partial t} + \rho u \frac{\partial h}{\partial x} - \frac{\partial}{\partial x}\left(\frac{\lambda}{cp}\frac{\partial h}{\partial x}\right) = \frac{\partial}{\partial x}\left(\sum_{k=1}^{N} h_k \left(\frac{1}{Le_k} - 1\right)\frac{\lambda}{cp}\frac{\partial Y_k}{\partial x}\right), \tag{2.65}$$

where the mass fraction of a species Y_k is given by

$$\rho \frac{\partial Y_k}{\partial t} + \rho u \frac{\partial Y_k}{\partial x} - \frac{\partial}{\partial x}\left(\rho D_{km}\frac{\partial Y_k}{\partial x}\right) = \dot{\omega_k} \tag{2.66}$$

and the sum of all species' mass fractions is equal to one:

$$\sum_{k=1}^{N} Y_k = 1. \tag{2.67}$$

[2] From this it follows, that intermediate species as CO cannot be correctly calculated under these assumptions.

The mass fractions of all species for one flamelet are obtained as solution from Chem1D, as shown in figure 2.4. The progress of the reaction can be followed along the geometrical normal of the flame front. Also the temperature, density, molar mass and other gas properties are available from these calculations.

2.3.5 Mixture Fraction and Progress Variable

A common way to overcome the problem of limited computing power is either to solve only for the major species taking place in the reaction or to link species concentration and chemical sources to another variable that is calculated during the CFD simulation. Then Y_k and $\dot{\omega}_k$ of all species can be calculated as a function of this one variable. In non-premixed combustion the diffusion process between fuel and oxidizer is determining the velocity of the reaction process. Reaction is much faster than laminar or turbulent diffusion processes. Therefore, it is common to introduce a mixture fraction variable that determines the composition of fuel and oxidizer within the flow field. This mixture fraction $\mathcal{Z}$ can be uniquely defined for values of Y_k by:

$$\mathcal{Z} = \frac{sY_F - Y_O + Y_O^0}{sY_F^0 + Y_O^0}, \tag{2.68}$$

reaching from 0 for the pure oxidizer (O) to 1 for pure fuel (F), where s is the ratio between oxidizer and fuel reaction rate $\frac{\dot{\omega}_O}{\dot{\omega}_F}$.

One premixed flamelet can be calculated for each given mixture fraction using Chem1D. For non-premixed flames the assumption “mixed is burnt” delivers always the final state of the flamelet as solution to the mixture fraction. This is not applicable for technical applications, such as burners in gas turbines. Here, due to the extensive mixing process in the swirler but also due to premixing the fuel to a certain extend with the oxidizer before entering the reaction zone, there may exist some regime, where the “mixed is burnt” assumption does not hold. A second control variable is needed to uniquely define the burning state. As known from premixed flames, the scalar variable for progress indication shall take a value from 0 for the un-burnt gases to 1 for the burnt gases. This progress variable $\mathcal{Y}$ must be a scalar quantity that continuously increases during the combustion process, e.g. the formation of a final product, or a sum of several products. Van Oijen [131] uses a combination of H_2, H_2O and CO_2 for the reaction progress of methane combustion.

$$\mathcal{Y} = \frac{Y_{H_2}/M_{H_2} + Y_{H_2O}/M_{H_2O} + Y_{CO_2}/M_{CO_2}}{Y_{H_2,eq}/M_{H_2} + Y_{H_2O,eq}/M_{H_2O} + Y_{CO_2,eq}/M_{CO_2}} \tag{2.69}$$

Equilibrium values of the species $Y_{k,eq}$ are used to scale $\mathcal{Y}$ between 0 and 1.

2.3.6 Flamelet Generated Manifolds

Premixed flamelets are calculated for different mixture fractions that are to be expected during the combustion. For each flamelet the progress variable and its source term is constructed. The entire set of flamelets form the Flamelet Generated Manifold (FGM) that constitutes the set of possible states (of species concentration, temperature, etc.) during the combustion. On the one hand the mixture fraction variable defines the extend of mixing between oxidizer and fuel, on the other hand the progress variable defines, in how far the mixed reactants have reacted to create the products. Both variables are transported as standard scalars in the CFD algorithm. Their Favre averaged transport equations in RANS context, omitting the unsteady terms, are given as [102]:

$$\frac{\partial}{\partial x_j}(\bar{\rho}\tilde{u}_i\tilde{\mathcal{Z}}) = \frac{\partial}{\partial x_j}\left[\left(\bar{\rho}D + \frac{\mu_t}{Sc_t}\right)\frac{\partial\tilde{\mathcal{Z}}}{\partial x_j}\right] \tag{2.70}$$

$$\frac{\partial}{\partial x_j}(\bar{\rho}\tilde{u}_i\tilde{\mathcal{Y}}) = \frac{\partial}{\partial x_j}\left[\left(\bar{\rho}D + \frac{\mu_t}{Sc_t}\right)\frac{\partial\tilde{\mathcal{Y}}}{\partial x_j}\right] + \overline{S_{\mathcal{Y}}} \tag{2.71}$$

$$\frac{\partial}{\partial x_j}(\bar{\rho}\tilde{u}_i\overline{\mathcal{Z}''^2}) = \frac{\partial}{\partial x_j}\left[\left(\bar{\rho}D + \frac{\mu_t}{Sc_t}\right)\frac{\partial\overline{\mathcal{Z}''^2}}{\partial x_j}\right] + 2\,C_1\bar{\rho}\frac{\mu_t}{Sc_t}\left(\frac{\partial\tilde{\mathcal{Z}}}{\partial x_j}\right)^2 - C_2\,\bar{\rho}\frac{\epsilon}{k}\overline{\mathcal{Z}''^2} \tag{2.72}$$

$$\frac{\partial}{\partial x_j}(\bar{\rho}\tilde{u}_i\overline{\mathcal{Y}''^2}) = \frac{\partial}{\partial x_j}\left[\left(\bar{\rho}D + \frac{\mu_t}{Sc_t}\right)\frac{\partial\overline{\mathcal{Y}''^2}}{\partial x_j}\right] + 2\,C_3\bar{\rho}\frac{\mu_t}{Sc_t}\left(\frac{\partial\tilde{\mathcal{Y}}}{\partial x_j}\right)^2 + 2C_4\overline{\mathcal{Y}''^2\overline{S_{\mathcal{Y}}}} - C_5\bar{\rho}\frac{\epsilon}{k}\overline{\mathcal{Y}''^2} \tag{2.73}$$

The transport equation for the mixture fracture does not have a source term. The progress variable does, as the progress is influenced by the combustion. The source term $\tilde{S}_{\mathcal{Y}}$ is to be read out from the FGM table.

2.4 Turbulence - Chemistry Interaction

The set of flamelets for different mixture fractions, obtained from FGM calculations, have to be made accessible for the CFD-calculations. For a laminar flow this is straightforward; the quantities (like temperature, density, species concentrations and source terms) can be directly determined from the table. However, for turbulent flows the flow properties are described by a mean and its variance. Both the mean and the variance of the mixture fraction and progress variable have to be taken into account to determine the mean value of the derived properties from the FGM table. It holds:

$$\widetilde{\Phi}(\mathcal{Z},\mathcal{Y}) \neq \Phi(\tilde{\mathcal{Z}},\tilde{\mathcal{Y}}) \tag{2.74}$$

2.4.1 Probability Density Function

The mean value and the variance of a quantity are stochastic measures for the temporal and spatial distribution of this quantity. This distribution can be described via a probability density function. The shape of a probability density function can be determined by moments. The more moments of a pdf are known, the more exact the shape is known. But to exactly know a pdf's shape all infinite numbers of moments have to be known. If only the zeroth (mean) and the first (variance) moment of a pdf are known, the actual shape is still unknown. It could be a Gauss-distribution, a δ-function or a β-distribution, or any other pdf. If higher moments are not to be considered in the CFD-solver the actual pdf in the flame needs to be presumed, keeping in mind, that the assumption most likely only comes close to the real distribution.

2.4.2 Statistical Independence

The distribution of the mean chemical state $\tilde{\Phi}$ depends on the joint pdf of mixture fraction and progress variable.

$$\widetilde{\Phi}(\mathcal{Z},\mathcal{Y}) = \int\int \Phi(\mathcal{Z},\mathcal{Y})\mathcal{P}(\mathcal{Z},\mathcal{Y})d\mathcal{Z}d\mathcal{Y} \tag{2.75}$$

Modeling of such a joint pdf is difficult and requires some restricting presumptions [87]. A common way to overcome the problem of finding an adequate joint pdf is assuming statistical independence of $\mathcal{Z}$ and $\mathcal{Y}$. Then the joint pdf can be written as the product of two pdfs:

$$\mathcal{P}(\mathcal{Z},\mathcal{Y}) = \mathcal{P}(\mathcal{Z}) \cdot \mathcal{P}(\mathcal{Y}) \tag{2.76}$$

2.4.3 Presumed PDF

A common assumption for the shape of the mixture fraction distribution is the β-distribution, BD. It is defined for a variable Φ as:

$$\mathrm{BD}(\Phi;\alpha,\beta) = \frac{\Phi^{(\alpha-1)}(1-\Phi)^{(\beta-1)}}{\sum_0^1 \Phi^{(\alpha-1)}(1-\Phi)^{(\beta-1)}d\Phi} \tag{2.77}$$

For $0 < \Phi < 1$. Where α and β are given as

$$\alpha = \bar{\Phi}\left[\frac{\bar{\Phi}(1-\bar{\Phi})}{\overline{\Phi''^2}} - 1\right] \quad ;\beta = \frac{\alpha}{\bar{\Phi}} - \alpha \tag{2.78}$$

The mean and the variance of Φ are given as:

$$\bar{\Phi} = \int_0^1 \Phi \, \mathrm{BD}(\Phi) d\Phi \tag{2.79}$$

$$\overline{\Phi''^2} = \int_0^1 (\Phi - \bar{\Phi})^2 \, \mathrm{BD}(\Phi) d\Phi \tag{2.80}$$

There are different justifications for taking one or another pdf. Pope [95] for example developed an 'a-priori' pdf for passive scalars based on the assumption "that the statistically-most-likely distribution maximizes the entropy", while arguing that shapes proposed by other authors (e.g. Gauss-pdf, δ-pdf, β-pdf) lack physical justification. However, for the mixture fraction the β-distribution gives good results compared to experimental data [103].
For a long time the β-pdf was also commonly used for the progress variable [68]. But recently the drawbacks of using an ad-hoc shaped pdf for the progress variable are critically questioned. Bray [17] for example showed, that choosing the β-pdf may overestimate the heat release and suggests an approach that incorporates the chemical flame properties into the presumed shape. This idea is also followed by Salehi [109]. Domingo et al. [31] use information of the spatial resolution within the reaction zone to set up the presumed pdf.
The value of the progress variable significantly influences the calculated heat release. In LES context this influence is of special importance as it affects the density fluctuations that prominently influence the instationary calculations. Kuehne et al. [67] made an investigation on the pdf's shape of the mixture and the progress variable using LES/Monte-Carlo Transported PDF (MC-TPDF). The β-pdf shape for the mixture fraction was shown to be a suitable model. For the progress variable neither the β-pdf nor the δ-pdf gave comparable results to the MC-TPDF closure in the investigated configuration. The β-pdf was found to be unsuitable, as it is for example not able to predict double peaks within the distribution that were observed using MC-TPDF. The MC-TPDF also showed perceptible variations for the progress variable in regions of strong mixing, which is an indication that the δ-pdf may also be inappropriate to resemble the shape of the progress variable's pdf.

As illustrated, choosing the right pdf-shape for pre-integrating flamelets from the FGM table is a science for itself. But if one had to choose an ad-hoc shape for the progress variable, as done for the mixture-fraction, in LES context using a δ-function was adequate to obtain reasonable results [87, 44], despite the findings of Kuehne mentioned before. The cells are comparatively small, therefore the variance is too. As for reactive flow calculations the cell size is getting smaller and smaller, this effect becomes more pronounced.

In RANS the spatial resolution in general is smaller. Hence, the variance of the progress variable in one cell will presumably be higher. Then, using a 2-δ-function is less justifiable. Therefore the β-pdf is chosen in this thesis, notwithstanding the named disadvantages. Based on today's knowledge this assumption is as good as any other ad-hoc shaped pdf and was therefore also chosen by other authors [37, 80]. Especially in RANS context, where the calculation of the turbulence's variance is not perfect for complex technical flows, the inaccuracy made by choosing the wrong pdf should be indistinguishable from the miscalculation of the variance. Consequently, the β-pdf was chosen for both mixture fraction and progress variable to pre-integrate the premixed flamelets obtained with Chem1D to an PPDF-FGM-table.

The resulting PPDF-FGM-table is four-dimensional. It is spanned over the $\mathcal{Z}, \mathcal{Z}''^2, \mathcal{Y}, \mathcal{Y}''^2$ - space. For any combination of these four variables temperature, species' mass fractions and gas constants are tabled. They are accessible for the CFD-solver via a four-dimensional interpolation routine. The interaction between turbulence and reaction is hence given by the variances of the mixture fraction $\mathcal{Z}''^2$ and the variance of the progress variable $\mathcal{Y}''^2$ and its influence on the flamelet solution.

2.5 Compressibility

As shown in the previous section, the density of a reacting gas will change due to a reaction process. For a gas the density is a function of the pressure, temperature and the molar mass and can be calculated by the ideal gas law:

$$\rho = \frac{p}{\frac{R}{M}T} \tag{2.81}$$

R is the universal gas constant and M the molar mass of the gas. A sound wave is a pressure perturbation that travels through a medium [129]. The traveling velocity of a pressure perturbation is called speed of sound, a. For an isentropic flow it holds:

$$a^2 = \left(\frac{\partial p}{\partial \rho}\right)_s \tag{2.82}$$

The "compressibility of a gas" is the change in density due to a change in pressure and is defined as:

$$\tau_c = -\frac{1}{\rho}\frac{d\rho}{dp} \tag{2.83}$$

For an isentropic change of state it holds that $p = C\,\rho^\gamma$ and using the ideal gas relation (2.81) it follows:

$$a = \sqrt{\gamma \frac{R}{M}T} \tag{2.84}$$

where γ is the isentropic coefficient. It is defined as the ratio between the specific heat at constant pressure c_p and the specific heat at constant volume c_v.

$$\gamma = \frac{c_p}{c_v} \tag{2.85}$$

For CFD calculations it is useful only to use one of both definitions in the code to maintain consistency. By substituting c_v with the relation $c_v = c_p - \frac{R}{M}$, γ can be written as:

$$\gamma = \frac{1}{1 - \frac{R}{c_p\,M}} \tag{2.86}$$

Mach Number

Similarly to the Reynolds number, which is a measure for the relation of the inertial forces to the viscous forces, the Mach number is defined as the relation of inertial forces to elastic forces:

$$Ma = \frac{U}{a} \tag{2.87}$$

U is the local flow velocity.
A "flow" is said to be "compressible" if the density change due to pressure change induced by the flow velocity is more than 5 %.

$$\frac{\Delta\rho}{\rho} = 0.05 \tag{2.88}$$

For a gas with $\gamma = 1.4$ (air) this is valid for approximately Mach = 0.3. Different regimes for different Mach numbers are distinguished [49][3] :

	Ma	< 0.3	-	subsonic incompressible
0.3 <	Ma	< 0.8	-	subsonic
0.8 <	Ma	< 1.2	-	transonic
1.2 <	Ma	< 5	-	supersonic
5 <	Ma		-	hypersonic

While considering the flow in CTI context the Mach number will remain below 0.3 in the front part of the combustor where the reaction is present. Here, incompressible conditions may be assumed. Within the NGV passages Mach numbers of the transonic regime are reached.

A very important equation for calculations with compressible flow is the gas dynamics relation of an isentropic flow. While the total pressure of an incompressible fluid may be calculated using Bernoulli's equation:

$$p_{tot} = p_{stat} + \rho\frac{u^2}{2}\,, \tag{2.89}$$

the total pressure of a compressible flow is a function of the Mach number and given by:

$$p_{tot} = p_{stat}\left(1 + \frac{\gamma - 1}{2}Ma^2\right)^{\frac{\gamma}{\gamma-1}}\,. \tag{2.90}$$

[3] The upper and lower boundaries for the transonic region vary for different sources

3 Numerical Methods

In this thesis computational methods are used to simulate combusting flows. As outlined before a solver is needed that is able to solve for incompressible as well as for compressible reactive flow. Density changes due to combustion, as well as to gas dynamics, need to be accounted for. Currently the combustor and NGV are analyzed and designed separately using different CFD tools:

The combustion process takes place in that part of the combustor, where compressibility effects are negligible, as the Mach-number is well below 0.3. Many authors use the incompressible formulation of the Navier-Stokes equation for combustion simulations, e.g. [44, 87]. The density is determined from various combustion models, for example the one introduced in section 2.3. The SIMPLE[1] algorithm [23] or related pressure-correction methods are commonly used for solving the incompressible Navier-Stokes equations (section 3.2.6). At RRD the combustion solver PRECISE-UNS is used. It is based on the SIMPLE procedure and an in-house tool, which is developed by the combustion group. In contrast to commercial codes such as FLUENT or CFX, the source code is open for the company and can thus be extended with new models for combustion, spray, etc. The SIMPLE procedure can - in its basic form - not be used for compressible flow calculations.

Turbomachinery parts, as the NGV, are designed with special so-called density based solvers (an overview of those methods can be found in [50]). The in-house tool of Rolls-Royce plc. is Hydra [70] and used by the turbine designers next to commercial codes. For density-based solution procedures it is difficult to solve low-Mach number flows. They make use of the hyperbolic nature of the compressible equations by employing their real characteristics during the solution procedure. For incompressible flows there are no real characteristics. To reach a solution for low-Mach number flows the time- or iteration step size must be decreased which leads to a high number of required steps and therefore long computational time. Special preconditioning is necessary to reach a solution for flows with very low velocities [133].

Either a combustion model has to be implemented into the compressible turbomachinery code or the incompressible combustion solver has to be extended for all-Mach number flows, to obtain a code that can be used in both regions. In general both approaches are possible. In this thesis the second option was chosen. The focus of this work is the

[1] Semi Implicit Method for solving Pressure Linked Equations

influence from the NGV on the flow field within the combustor. The interaction takes places in between both components, in the rear part of the combustor. Thus, the combustor is the main part that is in focus and investigations concerning the feedback from the NGV will be performed by the combustor group (In contrast to that, investigations concerning the influence on the turbine (section 1.2.1) will be performed by the turbine group). It is reasonable to use a code that was specially designed for simulating combustion processes. In PRECISE-UNS additional models are available, such as spray and Lagrange particle tracking, which are required to calculate the flow in a combustor. During the design process of the combustor most of the investigations necessary will still be performed with the incompressible version of PRECISE-UNS. Using the same basic code for the interaction investigations gives the possibility to check for consistency in the calculation of the combustion process itself.

Starting from PRECISE-UNS with PPDF-FGM already available, two main tasks have to be accomplished to obtain a solver for the complete combustor-NGV domain. Firstly, the code needs to be extended for compressible flow. The total enthalpy equation needs to be implemented to account for the coupling of pressure and density. This equation must be incorporated into the solution procedure with an extended SIMPLE algorithm. The procedure will be explained in chapter 4.
Secondly, the interface between combustion model and CFD-solver must be altered. The temperature can not be treated as a passive scalar as it is done when solving for incompressible reacting flow, because it needs to be fed back into the enthalpy equation. For this requirement a coupling procedure was developed and is to be explained in chapter 5.

But first the basic numerical methods and structure of PRECISE-UNS are briefly described. For further explanation it is referenced to Peric et. al. [89]. PRECISE-UNS is written in Fortran90 and some small source code examples shall be used to clarify the numerical procedure.

3.1 Discretization of Transport Equations

The equations for mass, momentum, energy (2.24 - 2.26) and scalars (k, ϵ, $\mathcal{Z}$, etc.) can be written in the general form for Φ:

$$\frac{\partial}{\partial t}\left(\bar{\rho}\,\Phi\right) + \frac{\partial}{\partial x_j}\left(\bar{\rho}\,\tilde{u}_i\,\Phi\right) = \frac{\partial}{\partial x_j}\left(\Gamma_\Phi \frac{\partial}{\partial x_j}\right) + S_\Phi \tag{3.1}$$

3.1.1 Finite Volume Method

The Finite Volume method (FVM) was developed for solving these equations numerically. The domain of the flow under investigation is subdivided into many small control volumes, called cells, which together form the numerical grid. This operation is called the geometrical discretization and can be performed with the help of grid generating tools like Ansys® ICEM CFD or Gambit®, for example. These programs allow to generate a grid with the help of a graphical user interface. First the geometry of the flow domain needs to be set up and then the geometry can be divided into small blocks and cells successively. In the end the grid is written out in a data format that can be read by the CFD solver. These tools commonly incorporate interfaces that allow to import the geometry from CAD programs like ProE® or CATIA®.

Accordingly, the equations need to be discretized. The principle of conservation of mass, momentum and energy within a bounded control volume also holds for every cell of the domain. The integral form of equation (3.1) is needed. For any variable Φ within a control volume (cell) V with adjacent faces S it reads:

$$\int_V \frac{\partial}{\partial t}(\bar{\rho}\,\Phi)\,dV + \int_S \bar{\rho}\,\tilde{u}_i\,\Phi\,\vec{n}\,dS = \int_S \left(D\,\frac{\partial \Phi}{\partial x_j}\right)\,\vec{n}\,dS + \int_V S_\Phi\,dV\,, \tag{3.2}$$

where D represents the diffusive terms and $\vec{n}$ is the vector normal to S. Note, that volumetric terms, as the unsteady change of Φ, are denoted by a volume integral, while fluxes are considered via its movement over the cell's faces. The Gauss Theorem is used to convert volume fluxes into the sum of the fluxes over the cell's faces.

$$\nabla\Phi_P = \frac{1}{V_P}\sum_{i=1}^{n_f}\Phi_i\,S_i \tag{3.3}$$

The order of the spatial derivatives needed to discretize the equations is hereby reduced. For calculating the convective fluxes the values of Φ are needed at the face centers and for calculating the diffusive fluxes the gradient of Φ is needed. After discretization a linear set of equations is obtained for every variable Φ of the form:

$$A\Phi = S \tag{3.4}$$

which has to be solved by a linear matrix solver. A is the coefficient matrix, and S is the source term vector.

3.1.2 Implicit Treatment

When solving an algebraic equation of form (3.4) explicit and implicit methods are available. If Φ only depends on known values for A and S the method is said to be explicit. If Φ itself is used for calculating A and/or S the solution algorithm is called implicit. In an implicit algorithm solving of equation (3.4) must be repeated until the final numerical solution has converged to the analytic solution. The difference between the final solution and current solution is called residuum. For the first step there is no Φ available from the previous solution, so an initial guess is needed. The number of iterations needed for convergence thus depends among other things on the proximity of the guess to the final solution. One benefit of implicit schemes is their robustness to far-off values of Φ, A and S, compared to explicit solvers.

3.1.3 Solving the Algebraic Equations

For solving the algebraic equations of the form $A\Phi = S$ for Φ there exist many possibilities. In PRECISE-UNS the Hypre Solver [52] is used for the pressure equation and the SPARSEKIT Version 2 Solver by Yousef Saad [108] is used for all other variables. Independent on the solver, the matrix A and vector S must be set up within PRECISE-UNS. In the next section this procedure is described.

3.2 Precise-Unstructured

This section begins by explaining the variable and grid arrangement used in PRECISE-UNS. These determine the interpolation routines used for calculating the convective and diffusive fluxes, which are needed for setting up the transport equations.

3.2.1 Collocated Variable Arrangement

In PRECISE-UNS all variables are stored at the cell centers. This arrangement is called collocated grid in contrast to staggered grids, in which the values for the velocity and pressure are stored at different places of the control volume. This is important for the SIMPLE algorithm explained in 3.2.6, as certain measures have to be taken to get a smooth solution field for collocated variable arrangement.

3.2.2 Unstructured Grids vs. Structured Grids

There are two possibilities of structuring the grid information commonly used. In *structured grids* every cell has the same form, e.g. quadratic in 2d and hexaedral in 3d and the same number of neighbors. The location of each node around a cell P within the grid is indexed by i, j (and k) in the two (three) space directions. The neighboring nodes are identified by the next higher or lower index (i.e. $i+1$ or $i-1$). The neighbors of each cell are identified by the cardinal directions (North, South, East, West) plus Bottom and Top for 3d cases. The faces of each cell are identified by the cardinal directions starting with lower case letters, (north, south, east, west) plus bottom and top for 3d cases, accordingly. When setting up the algebraic equations of form (3.2) the code 'walks' over every cell 1 to N_P and adds up the volume sources for every cell i, j, k and fluxes over the faces n, s, e, w, t, b. A sketch of such a cell arrangement is given in figure 3.1.

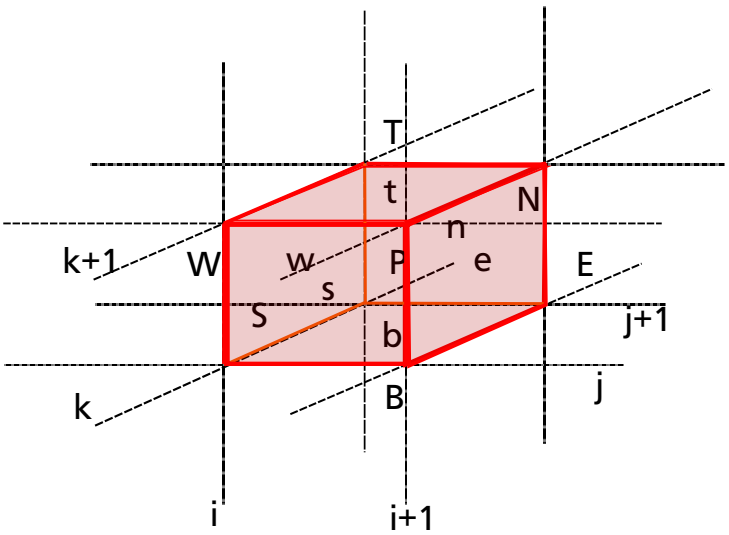

Figure 3.1.: Cell P and adjacencies in structured grid arrangement

In *unstructured grids* different shapes for each cell are possible. All N_{cell} cells are numbered from 1 to N_{cell}. At the same time all faces are stored from 1 to N_{face}. An array is set up that contains information about the adjacencies. For every face i the indexes of the two adjacent cells are stored. The cell that is found first is cell P with index `ip` and the other cell is N with index `in` (see code in figure 3.3). It is obvious that in this way it does not matter how many faces do belong to one cell. The more faces one cell has, the more often the cell will be present in the face-cell array. When setting up the algebraic equations of form (3.2) the code 'walks' over the faces while adding up the fluxes for each cell. A sketch of a face in an 'unstructured' arrangement and according labeling is given in figure 3.2. PRECISE-UNS uses unstructured grids. The obvious advantage over structured grid is the flexibility in the cells' shape that can be used. Complex geometries

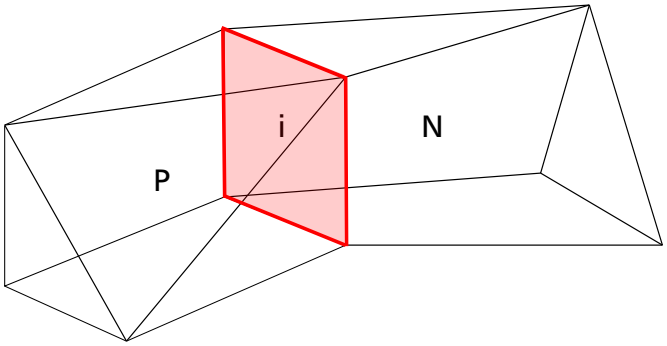

Figure 3.2.: Face i and adjacencies in unstructured grid arrangement

```
do i=1,NFace
      ip = Face(i)%cell1
      in = Face(i)%cell2

      Sface(i) = ...
      Aface(i) = ...

     S(ip) = S(ip) + S(i)
     S(in) = S(ip) - S(i)

     A(ip) = A(ip) + S(i)
     A(in) = A(in) - S(i)
enddo
```

```
do ip=1,Ncel
     S(ip) = ...
     A(ip) = ...

     S(ip) = S(ip) + S(ip)
     A(ip) = A(ip) + A(ip)
enddo
```

Figure 3.3.: Algorithm for setting up the source terms and the coefficient matrix

as found in combustors are easier to divide into small cells if the shape of a cell can freely be chosen. The main difference for the numerical algorithm stems from setting up the coefficients for the algebraic equations of form (3.4) to be solved. The procedure for the unstructured algorithm in PRECISE-UNS is given by a do-loop over the faces to collect all the flux information (figure 3.3 left side). A do-loop over the cells (figure 3.3 right side) collects all the information about volume forces.

3.2.3 Values and Gradients on Faces

Values on Faces

As equation (3.3) shows, one needs to know the value Φ not only in the cell centers but also at the center of each face. These values can be calculated using linear interpolation between the face's i adjacent cells.

$$\Phi_{face,i} = \mathrm{fac}_P \cdot \Phi_P + \mathrm{fac}_N \cdot \Phi_N \tag{3.5}$$

The constants fac_P and fac_N are the interpolation factors that identify the relative distances of the cell's centers to the face. They are calculated for each cell P neighboring cell N via face i by:

$$\mathsf{fac}_P = \frac{\vec{n}_i \cdot (\vec{x}_i - \vec{x}_p)}{\vec{n}_i \cdot (\vec{x}_i - \vec{x}_p) + \vec{n}_i \cdot (\vec{x}_n - \vec{x}_i)}\,, \tag{3.6}$$

where $\vec{n}_i$ is the normal vector of face i, $\vec{x}_i$ the position vector of the face center and $\vec{x}_P$ and $\vec{x}_N$ the position vectors of the cell centers respectively. This interpolation procedure is a Central Differencing Scheme (CDS), which is second order accurate in space. Using CDS for the convective terms may lead to oscillations during the solution procedure. To increase stability a blend with first order accurate upwind (Upwind Differencing Scheme - UDS) is possible. For UDS the value at the face i is set to the value of cell P or N, that lies upstream of the flux direction.
If discretization according to equation (3.5) is used, the resulting $\Phi_{face,i}$ will lie somewhere on face i between the centers of cell P and cell N. It will be at the center c of the interjacent face, if the distance vector $\vec{x}_{PN}$

$$\vec{x}_{PN} = \vec{x}_N - \vec{x}_P \tag{3.7}$$

is in line to the face's normal vector. That is only the case for orthogonal grids. In most of the cases when calculating complex geometries, this condition is not given and cells are skewed. In that case a correction for the face's center (c) value needs to be calculated. In PRECISE-UNS a correction term is added that is the scalar product of the vector that is pointing from the face's center to the intersection of the face and a line connecting the cell centre points of both neighboring cells.

$$\Phi_{i,c} \approx \Phi_i + (\vec{x}_{i,c} - \vec{x}_i) \left(\frac{\partial \Phi}{\partial x_i}\right)_i \tag{3.8}$$

Gradients on Faces

The gradients on faces must also be known. The gradients are interpolated similarly to equation (3.5) by:

$$\left(\frac{\partial \Phi}{\partial x_i}\right)_{face,i} = \mathsf{fac}_P \cdot \left(\frac{\partial \Phi}{\partial x_i}\right)_P + \mathsf{fac}_N \cdot \left(\frac{\partial \Phi}{\partial x_i}\right)_N \tag{3.9}$$

Unlike the values on faces, the gradients are always interpolated using CDS and are not corrected for skewness. For highly distorted grids this may introduce error into the numerical solution.

3.2.4 Convection Terms

As given in equation (3.2) the convective term is calculated by adding up the flux over the faces of each cell.

$$\int_S \bar{\rho}\,\tilde{u}_i\,\Phi\,\vec{n}\,dS \tag{3.10}$$

The order of the convection scheme depends on the interpolation routine that is used to calculate Φ on the face as explained above. First order UDS is stable but adds numerical diffusion to the solution. CDS is second order exact but may lead to oscillations. Therefore, within PRECISE-UNS the CDS (ho) convective flux is blended with the first order scheme (UDS) (lo). The low order discretization is implicitly taken into account (in Matrix A), while the high order correction is added explicitly. The relative amount of higher order discretization employed is called blending factor γ_{blend} and is used to scale the source term.

$$S(\Phi)_{i,blend} = \gamma_{blend} \cdot (S(\Phi^{ho})_i - S(\Phi^{lo})_i) \tag{3.11}$$

If it is equal to zero the amount of convective flux accounted for in the source term is also zero, and therefore the convective flux will depend only on the lower order implicit term used for calculating A. If γ_{blend} is equal to 1 the lower order discretization in A and S will cancel out and the explicit higher order treatment for the convective flux will remain. In any case will the higher order discretization only influence the solution as part of the correction in the source term. This procedure is also called deferred correction method.

Numerical Dissipation

The influence of the numerical scheme on energy conservation can very nicely be seen with a compressible code, e.g. a code, that solves for the energy equation. As said before, while using UDS, that is only first order exact in space, some numerical dissipation will be introduced. This numerical dissipation will be present in the solution for the energy equation. Consider the following: Due to numerical dissipation in the convective terms for the momentum equations the velocity will be computed a little slower than it actually would be. Therefore, also the total enthalpy is convected less, and it looses some of its starting value. In a perfect fluid without friction, and that is what is calculated with the euler-equation, namely setting the viscosity to a value well below computer precision, there should not be any energy loss. If there is some loss in the total enthalpy it is due to the different discretization scheme used. In the converging-diverging nozzle test case (section 6.2.1) the influence of different blending between UDS and CDS for the convective terms is shown.

3.2.5 Diffusion Terms

The gradient at the cells centers are calculated using Gauss's theorem (3.3):

$$\left(\frac{\partial \Phi}{\partial x_i}\right)_P \approx \frac{1}{V_P} \sum_{i=1}^{n_f} \Phi_i S_i \tag{3.12}$$

A deferred correction (dc) is again used for calculating the diffusive fluxes. Here, it is leveraged to suppress oscillations that may stem from interpolating the gradients on the faces with a CDS scheme as in equation (3.9). For the implicit ($impl$) part the gradient in normal direction to the face is used [84]:

$$\left(\frac{\partial \Phi}{\partial n_i}\right)_{i,impl} \approx \left(\frac{\partial \Phi}{\partial x_i}\right)_{face,i} \cdot (\vec{x}_n - \vec{x}_p) \tag{3.13}$$

Then the source term adds up to

$$S(\Phi)_{i,dc} = \mu_{\Phi,i} \left(\frac{\partial \Phi}{\partial x_i}\right)_i - \mu_{\Phi,i} \left(\frac{\partial \Phi}{\partial n_i}\right)_{i,impl} . \tag{3.14}$$

The coefficient $A_i = \mu_{\Phi,i} D_i$ is used in the coefficient matrix for face i, where D_i is the implicit coefficient for face i with area S_i with normal vector $\vec{n}_S$, given as:

$$D_i = \frac{S_i \, |\vec{n}_S|}{\vec{n_S} \, \vec{x}_{PN}} . \tag{3.15}$$

The viscosity $\mu_{\Phi,i}$ is discretized in accordance with equation (3.5). Thus, the treatment of diffusive fluxes is second order accurate while the error is consistent to the error made in all interpolations.

3.2.6 Numerical Coupling of Mass and Momentum Equation

PRECISE-UNS uses the SIMPLE algorithm [23] as solution procedure of the incompressible Navier Stokes equation. Before explaining the necessary changes in order to solve the equations for compressible flows, in this section the standard SIMPLE procedure shall be explained. The basic idea is as follows:
In finite volume methods conservation of mass is the basis for drawing a control volume. It is assumed, that all the mass that flows into the control volume e.g. a duct, will leave the control volume. Within the control volume the velocity may change due to geometrical features, viscous forces or other introduced disturbances. But all the flow

that enters the domain, has to leave the domain at the end. Thus, the balance equation can be stated:

$$\begin{aligned} \dot{m}_{in} &= \dot{m}_{ou} \\ \rho_{in}\, u_{in}\, A_{in} &= \rho_{out}\, u_{out}\, A_{out} \end{aligned} \tag{3.16}$$

For an incompressible flow (without thermal expansion / reaction) the density ρ is constant and equation (3.16) simplifies to:

$$u_{in}\, \rho_{in}\, A_{in} = u_{out}\, \rho_{in}\, A_{out} \tag{3.17}$$

Within one incremental control volume this equation is also true, which leads to the integral form:

$$\int_{Faces} \dot{m} = \int_{Faces} \rho\, u_i\, A_i = 0. \tag{3.18}$$

In an iterating process the mass flux may not satisfy this condition in the first iteration n. The sum of the mass fluxes over the faces of one control volume can be considered as a source term, which is either positive or negative, depending on whether the present velocity is too high or too low:

$$\Delta \dot{m}_{CV} = S_{\dot{m}} \tag{3.19}$$

For a converged solution this should be zero. The mass fluxes need to be corrected. This is done by an additional mass flux $\dot{m}'$ for the next iteration $n+1$ for a face i:

$$\dot{m}_i^{n+1} = \dot{m}_i^n + \dot{m}_i' \tag{3.20}$$

It is obvious, that the sum of all these corrections over the faces of one control volume should be exactly the “discrepancy” source in equation (3.19).

$$\sum_{faces} \dot{m}_i' = S_{\dot{m}} \tag{3.21}$$

Now $\dot{m}'$ has to be estimated. It can be written as $u' \rho\, A$. An expression for the velocity correction can be derived from the momentum equation:

$$u_i' = -\frac{V}{a_p^u} \left(\frac{\partial p'}{\partial x_i} \right)_i \tag{3.22}$$

a_p^u is the coefficient of u in cell p in the momentum equation. When using the velocity correction to calculate $\dot{m}$, the continuity requirement will be fulfilled. As u' is a function of p' the continuity equation can be used to obtain a correction equation for the pressure:

$$a_p\, p_P' + \sum_{neighbors} a_n\, p_N' = -\sum_{faces} \dot{m} \tag{3.23}$$

a_p is the central coefficient for the solution matrix and is equal to the sum of a_n. With the obtained pressure correction p' the pressure field, the velocity field and the mass fluxes can be corrected by:

$$p^{n+1} = p^n + \gamma_p p' \tag{3.24}$$

$$u^{n+1} = u^n - \frac{V_P}{a_p} \left(\frac{dp'}{dx} \right)_P \tag{3.25}$$

$$\dot{m}_i^{n+1} = \dot{m}^n + \frac{\rho A_i^2}{a_p} (p'_N - p'_P) \tag{3.26}$$

Metaphorically speaking: The velocity field and the pressure field need to be consistent. If they are, mass conservation is obtained. Until then, the discrepancy in mass $S_{\dot{m}}$ defines for the pressure and the velocity field the need of change in order to fulfill mass conservation.
The equation for momentum and pressure are strongly coupled. To uncouple them the correction of the pressure field is under relaxed with the relaxation factor γ_p. The velocity and mass flux corrections are not under relaxed at this stage of the solution algorithm, but when they are calculated within the next iteration.

It is important to note that the actual value of p' is not important, but only its difference $\frac{dp'}{dx}$. Also in equation (3.24) actually only the difference to a reference pressure p_{ref} somewhere in the domain is added. That is also the reason, why for an incompressible calculation the actual thermal (static) pressure is not important to know for the solution of the velocity field, but only the momentum driving pressure. This is often called working pressure [128].
Note, that equation (3.23) was derived under the assumption of incompressible flow. Still it may be used for any flow regime. The density could be calculated via the gas law by adding the local reference thermal pressure to the working pressure. It is possible to reach a converged solution only by adopting the velocity field to the pressure changes for lower Mach numbers < 0.5. If the Mach Number is higher, higher pressure differences lead to higher velocity changes *and* higher density changes. Then, by trying to adopt the pressure field to the mass conservation requirement, the values of pressure and velocity would become unrealistic, which would lead to divergence of the solution. To overcome this problem the SIMPLE algorithm needs to be extended. This extension is explained in the next chapter.

4 Implementation of the Compressible SIMPLE Algorithm

The numerical starting point for this thesis was the incompressible pressure based solver PRECISE-UNS from Rolls-Royce Deutschland, which is used to compute the flow field within combustors of jet engines. As pointed out in section 1.3 this code shall be used to also calculate the compressible flow within the first stator blades of the high pressure turbine, following the combustor.
The code uses a pressure-based SIMPLE procedure (section 3.2.6) to solve the incompressible Navier Stokes equations. This shall be kept and extended for compressible flow.

4.1 Extended SIMPLE Algorithm

With density changing depending on p, i.e. $\rho = f(p)$ (definition of compressibility, section 2.5), the pressure correction equation is not flexible enough to reach a converged solution for the velocity and pressure field (section 3.2.6). At higher Mach numbers the density will increase. Introducing a density correction ρ' the basic equation (3.20) changes to:

$$\dot{m}^{n+1} = (\rho^n + \rho')\,(u_i^n + u_i')A_i = \rho^n\, u_i^n\, A_i + \rho^n\, u_i'\, A_i + \rho'\, u_i^n\, A_i + \rho'\, u_i'\, A_i \qquad (4.1)$$

In contrast to the incompressible version there are two additional correction terms, the third and forth on the right hand side of equation (4.1). The forth one is the product of two corrections, which may be omitted as it is much smaller than the other two correction terms. Finally, the mass correction reads:

$$\dot{m}' = \rho^n\, u_i' + \rho'\, u_i^n \qquad (4.2)$$

With the additional second term, the correction obtains more “flexibility” to adopt the pressure field to velocity and density changes within the flow field. As in the incompressible version the velocity is corrected using the pressure gradient (equation (3.22)). The density correction is approximated with

$$\rho' \approx \left(\frac{\partial \rho}{\partial p}\right)_T p' = C_p\, p' = \frac{p'}{\gamma\, R\, T} \quad , \qquad (4.3)$$

which holds for an isotropic flow. Now the mass correction for face i reads:

$$\dot{m}'_i = -(\rho^n \, A \, V)_i \, \overline{\left(\frac{1}{a_p}\right)} \, \frac{\delta p'}{\delta n} + \frac{1}{\gamma \, R \, T}_i \, U_i^n p'_i \tag{4.4}$$

The bar $\overline{(\,)}$ denotes that interpolation is used for the overlined variable. It is important to discretize the face values for the old velocity U_i^n and density ρ_i^n in the same way, as it is done for the calculation of the momentum fluxes. If they are for example discretized with UDS while CDS was used for the momentum equation, numerical diffusion will be added to the solver, and the solution will not have the order chosen in the momentum flux discretization. The density correction at face i is discretized with CDS and also the correction for the velocity is discretized with CDS. For neither variable a correction for skewness of the grid is adopted. It was determined that using this correction would lead to divergence, especially for strong shocks near curved walls (test case supersonic bump, section 6.2.2).

The extended pressure correction reads as usual (equation (3.23)) but the neighbor coefficients are different:

$$a_n = \rho \left(\frac{1}{a_u}\right)_i \frac{\Delta V}{X_N - X_P} + f_n \, \frac{1}{R T_i} \, U_i \, \vec{n}_i \, A_i \tag{4.5}$$

where a_u is the coefficient from the momentum equation and f_n is the weighting factor for non-uniform grid spacing. ΔV denotes the volume of the cell. The central coefficient a_p is assembled as follows:

$$a_p = \sum_i^{faces} \left[\rho \left(\frac{1}{a_u}\right)_i \frac{\Delta V}{X_N - X_P} + \frac{1}{R T_i} \, U_i \, \vec{n}_i \, A_i \right] \tag{4.6}$$

The coefficient of the convective part is discretized with first order upwind to increase stability.

4.2 Implementation of Total Enthalpy Equation

The equation for total enthalpy has to be introduced for the compressible code. The convective term can be treated as the convective terms in all other equations. For the diffusive part three terms need to be considered, which are the turbulent heat flux, the viscous stress and the molecular diffusion and turbulent transport of energy:

$$Inst. + conv. = \frac{d}{dx_j} \left[\frac{\mu_{eff}}{Pr_T} \cdot \frac{\partial \tilde{h}}{\partial x_j} + u_i \cdot (\tau_{ij} + t_{ij}) + \mu_{eff} \cdot \frac{\partial k}{\partial x_j} \right] \tag{4.7}$$

For a stable working code it is important to have a diagonal dominant coefficient matrix. The problem arises, that none of the diffusive terms have total enthalpy included, so building up a diffusive coefficient for H is not straight forward. For the present code the following approach was developed:

The specific enthalpy $\tilde{h}$ in the heat flux term is substituted with help of equation (2.27) and it follows

$$\frac{\partial \tilde{h}}{\partial x_j} = \frac{\partial (\tilde{H} - \frac{\tilde{u_i}^2}{2} - \tilde{k})}{\partial x_j}. \tag{4.8}$$

Then H can be treated with the standard deferred correction approach, while that part of energy, namely the kinetic energy, that is transported too much, is subtracted explicitly from the source term in the total enthalpy equation.

$$\frac{\partial (\frac{\tilde{u_i}^2}{2} - \tilde{k})}{\partial x_j} = \tilde{u}_i \frac{\partial \tilde{u}_i}{\partial x_j} - \frac{\partial \tilde{k}}{\partial x_j} \tag{4.9}$$

Note that the diffusion coefficient to be used for velocity and kinetic energy flux is the same as for enthalpy.

4.3 Calculation of Temperature and Density

After having solved for the total enthalpy the temperature is calculated by:

$$T^{new} = (1 - \gamma_T)\, T^{old} + \gamma_T \left(\tilde{H} - \frac{1}{2}(U^2_{mag}) - \tilde{k} \right) / c_p \tag{4.10}$$

γ_T is a relaxation factor used for T. Values between 0.6 to 0.8 were found to induce good convergence behavior. Finally, the density is calculated via the ideal gas law at the end of each iteration.

The flowchart of the compressible algorithm in contrast to the incompressible algorithm is given at the end of the next chapter in figure 5.11.

4.4 Boundary Conditions for Compressible Flow

For compressible flow calculations the treatment of boundary conditions needs special attention at various places and for different flow conditions.

4.4.1 Subsonic Outflow

For compressible flows the static pressure is given as boundary condition at an outflow boundary. Thus, the pressure correction at the outflow is zero. This can directly be implemented at that part of the algorithm where the coefficient matrix for the pressure correction equation is set up. In the unstructured context, the information of whether a cell is next to a boundary is indirectly stored in the face information. The coefficients are summed up for every cell while 'walking' over the faces. To set the pressure correction to zero at the outlet for each cell it must be known, whether the cell is next to the outlet. The information is not given however. It is only known, which faces belong to the outlet boundary. Therefore, a search algorithm was implemented, that checks for every cell, whether one of the faces belongs to the outflow boundary. If true, the cell is categorized as outlet cell, for which the pressure correction shall be zero. The search algorithm consumes time and is therefore performed only once and then a logical parameter for every cell is stored, respectively.

For a complex flow, the outflow pressure will not be constant. Instead there will be a non-uniform static pressure field at the outlet. The static pressure field behind a stator for example (as in section 6.5.1) will have and increasing pressure towards the casing. The deflection of the flow in circumferential direction will lead to transportation of mass in outward direction. For a jet-flow (as in section 6.4.1) the static pressure will decrease in outward radial direction. These advanced pressure fields are handled 'by-hand' in a user-defined routine that was added to the code for this purpose.

4.4.2 Subsonic Inflow

At the inflow total conditions need to be given. Commonly the total pressure at inflow is pre-set and is defined by the isentropic relation of an ideal gas:

$$p_{tot} = p_{stat,inl} \left(1 + \frac{\gamma - 1}{2} Ma_{inl}^2\right)^{\frac{\gamma}{\gamma-1}} . \tag{4.11}$$

The Mach number at the inlet Ma_{inl} is given by

$$Ma_{inl} = \frac{U_{mag,inl}}{\sqrt{\gamma R T_{stat,inl}}}. \tag{4.12}$$

The total temperature is given by

$$T_{tot} = T_{stat,inl} \left(1 + \frac{\gamma - 1}{2} Ma_{inl}^2\right). \tag{4.13}$$

The solution strategy is as follows:
The static pressure at the inlet is extrapolated from inside. Together with the given total pressure and equation (4.11) the velocity can be estimated via:

$$U_{mag,inl} = \sqrt{\frac{2\gamma\, R\, T}{\gamma - 1}\left[\left(\frac{p_{tot}}{p_{stat,inl}}\right)^{\frac{\gamma-1}{\gamma}} - 1\right]} \tag{4.14}$$

The direction of the flow must further be defined by flow angles, as until here only the magnitude of the velocity is given. How this can be adjusted for 2-d flow is shown in [28].
For 3-dimensional flow and inlets whit normal face vectors free to point in any direction this treatment was re-written for spherical coordinate systems. Two angles and the vector's length are needed to uniquely define a vector in a spherical coordinate system. For the case of velocity vectors the length of the vector represents the magnitude of the velocity given by:

$$U_{mag} = \sqrt{U^2 + V^2 + W^2} \tag{4.15}$$

For representation in spherical coordinates (see for example [18]) the polar angle θ gives the angle between the positive z-axis and direction of U_{mag}, while the azimuthal angle ϕ is the angle between the positive x-axis and direction of U_{mag}. Thus, for example if the flow is entering the domain along (parallel to) the x-axis θ will be 90° and ϕ will be 0°. The (cartesian) velocity components are given by:

$$U = \sin\theta\cos\phi \cdot U_{mag} \tag{4.16}$$
$$V = \sin\theta\sin\phi \cdot U_{mag} \tag{4.17}$$
$$W = \cos\theta \cdot U_{mag} \tag{4.18}$$

For complex flows the inflow angle may be different for every inlet face. Then a global inflow angle cannot be set. Instead local flow angles must be given. This is either possible by-hand, or can be done via prescribing a velocity field and calculating the spherical flow angles, using

$$\theta = \arccos\frac{W}{\sqrt{U^2 + V^2 + W^2}} \tag{4.19}$$
$$\phi = \mathrm{atan2}(y, x) \tag{4.20}$$

While $\mathrm{atan2}$ is an $\arctan$ function that gives unique angles for the whole range from 0°- 360° of azimuthal revolution. In this case the prescribed velocity field will only

determine the direction of the flow, while the magnitude of the velocity will still be a function of equation (4.14).

As suggested by [28] the treatment of the inflow boundary condition was implemented into the pressure-correction equation directly, to speed up convergence. Accordingly, the coefficient for a subsonic inflow using spherical coordinates is:

$$A_{sub,inl} = \frac{\rho R T}{P_{tot} U_{mag,inl} \left((\sin\theta\cos\phi)^2 + (\sin\theta\sin\phi)^2 + (\cos\theta)^2\right)^{1/2}} \cdot \frac{\left[A_x(\sin\theta\cos\phi) + A_y(\sin\theta\sin\phi) + A_z(\cos\theta)\right]}{\left[1 + \frac{\gamma-1}{2}\frac{U^2_{mag,inl}\left((\sin\theta\cos\phi)^2+(\sin\theta\sin\phi)^2+(\cos\theta)^2\right)}{\gamma R T}\right]^{\frac{1-2\gamma}{\gamma}}} \quad (4.21)$$

A_x,A_y and A_z denote the inlet face area normal to the x, y and z-axis respectively.

During the iteration process the static pressure at the inlet will be a result of the static pressure at the outlet and the velocity field between inlet and outlet. The velocity inlet condition will adjust according to the given total pressure at the inlet that was prescribed as boundary condition. The difference between these pressures will hence define the mass flow that passes through the domain. Often it is the case that from experiments only the velocity field at the inlet and the static pressure at the outlet is known. Then the total pressure boundary conditions must be estimated for a first run. If the pressure drop (due to losses) within the domain is not known beforehand (or estimated wrongly) it might (and probably will) be necessary to adjust the total pressure in a second run and restart the simulation, to reach the desired velocity conditions at the inlet. As the velocity field is now already very close to the final solution this second run will converge much faster than the first run. Here it must be mentioned that changing the discretization between those two runs should be avoided, as this will also change the pressure drop within the system, due to the numerical dissipation (section 3.2.4).
For multiple inlets all the above remains valid. Depending on the complexity of the geometry and number of inlets that are to be calculated, estimating the correct total pressure conditions at the various inlets may become a complex task that leads to several re-runs of the simulation. Here it might be useful to perform an incompressible calculation of the incompressible parts of the domain under investigation to get an idea of the static pressure distribution within the geometry.

4.4.3 Supersonic Inflow

For a supersonic inflow also total pressure and temperature are defined, but also all velocity components, static pressure and static temperature have to be given, as no information of these variables can travel upstream the fluid flow. In jet engines this boundary condition is only necessary for ramjet or scramjet combustors, which are not focused in this thesis. Nonetheless, this boundary conditions was implemented for completeness. Its operability is demonstrated in test case 3 of the GAMM series ([104], section 6.2.2).

4.4.4 Supersonic Outflow

For a supersonic outflow the characteristics of the hyperbolic equations points outwards the computational domain. In other words: No information is traveling upstream the flow direction. This means that for the pressure-correction equation the coefficients for the boundary values only depend on the inside values. Thus, an upstream differencing scheme should be used.

4.4.5 Total Enthalpy at Inlet

Before calculating the total enthalpy according to equation (2.16), it needs to be updated at the inlet according to the total temperature condition at the inlet and the local velocity and temperature field:

$$H_{tot,inl} = c_p T_{inl} + \frac{u^2}{2} + k \tag{4.22}$$

T_{inl} is calculated from equation (4.13). In this way the total temperature is implicitly implemented as boundary condition at the subsonic inlet.

4.4.6 Wall Treatment

At an impermeable wall two flow conditions may be distinguished. The slip wall and the no-slip wall. For inviscid flows no friction is present, so the fluid will not stick to the wall and its tangential velocity will not be altered due to the wall. This is called a "slip" wall condition and can easily be implemented by setting the velocity at the bounding wall to the velocity at the cell center directly next to the wall. This should be updated after the pressure correction, so for the next gradient calculation the updated boundary

values are available. Otherwise there would be a gradient at the wall that describes the difference between present and old iteration, which could lead to inferior convergence behavior.
For viscous flows the no slip boundary condition has to be used at wall boundaries. Here, friction is present and the flow in the vicinity of the wall will be influenced, namely slowed down due to this adhesion effect. Interestingly, in german this condition is called "Haftbedingung" (adhesion condition) what stresses the meaning of this boundary condition. This wall boundary condition is a little more demanding to implement and depends on whether Low-Re number modeling or wall-function as explained in section 2.2.9 are used. In this thesis only high-Reynolds-number modeling using wall-functions is used. To account for the adhesive force due to the wall, the shear tensor present due to the velocity gradient between the centre of the first cell next to the wall and the wall velocity is calculated using the wall function (section 2.2.9). A corresponding force is added to the source term of the momentum equation.

4.4.7 Periodic Boundaries

At periodic boundaries the faces point to the attributed neighbor cell of the counterpart boundary. This cell is used as neighbor cell n to calculate all gradients and values on the boundary face in the same way as for the internal faces (section 3.2.3). Consequently, the discretization order for the periodic boundary is consistent with the rest of the domain.

The developed code, which is suitable to calculate compressible flow, is called:
PRECISE-UNSTRUCTURED-COMPRESSIBLE (PUC).

5 Coupling Tabulated Chemistry with Compressible SIMPLE Algorithm

The PPDF-FGM model with tabulated chemistry was originally developed for incompressible flow. In case of incompressibility the density does not change due to pressure changes. It is only a function of the combustion process and can therefore be read from the table. Using the standard SIMPLE algorithm, this density change is not fed back into the pressure correction equation. However, within the compressible SIMPLE algorithm, the density is part of the pressure correction equation. The density is calculated from the ideal gas law at the end of each iteration using the local static pressure. For incompressible conditions the static reference pressure is used to compute the density in the FGM table. Note that for incompressible flows the difference between the local static pressure and the reference pressure (at a given position within the domain) is small. For compressible flows the static pressure cannot be assumed to be constant, so using the tabulated density data would lead to mistakes. Actually, the flow could not be calculated within the compressible region. Therefore, a new coupling strategy had to be developed.

5.1 Temperature and Density

In the PPDF-FGM model species concentrations Y_k and the mean gas properties c_p, λ and γ are obtained as functions of mixture fraction $\mathcal{Z}$ and progress variable $\mathcal{Y}$ and the respective variances. While in incompressible pressure based CFD-solvers the temperature is only a passive scalar, i.e. it only depends on the reaction process, in compressible flow it also depends on changes due to compressibility effects in the subsonic compressible, transonic and supersonic regime. Here, the temperature is a function of the total enthalpy and the kinetic energy.

A discrete treatment of the effects on enthalpy shall be established to account for both effects, reaction and compressibility. The basic assumption is, that the regions of reaction and compressibility are separated. Considering the flow in CTI context two regions can be identified. The incompressible reactive flow within the combustor and the compressible flow within the NGV. Within the incompressible reactive flow region the sensible enthalpy does not change due to reaction, but only due to mixing of fuel and oxidizer

streams. In the compressible region the enthalpy changes due to compressibility while the total enthalpy remains constant.

Recall the Favre averaged total chemical enthalpy equation (5.1). In the following representation all before mentioned modeling assumptions are collected and all data to be obtained from tabulated chemistry is underlined:

$$\begin{aligned}\frac{\partial}{\partial t}(\bar{\rho}\tilde{H}) + \frac{\partial}{\partial x_j}(\bar{\rho}\tilde{u}_j\tilde{H}) =& \frac{\partial \bar{p}}{\partial t} + \frac{\partial}{\partial x_j}\left(\tilde{u}_j(t_{ij}+\tau_{ij})\right) + \frac{\partial}{\partial x_j}\left(\underline{(\frac{\mu_L}{Pr_L}+\frac{\mu_T}{Pr_T})\frac{\partial \tilde{h}}{\partial x_j}}\right) \\ &+ \frac{\partial}{\partial x_j}\left(\underline{(\mu_L+\frac{\mu_T}{\sigma_k})\frac{\partial \tilde{k}}{\partial x_j}}\right)\end{aligned} \tag{5.1}$$

The laminar diffusion $\frac{\mu_L}{\mathrm{Pr}_L}$ of enthalpy can be written as function of laminar thermal diffusion:

$$\frac{\mu_L}{\mathrm{Pr}_L} = \frac{\lambda_L}{c_p} \tag{5.2}$$

λ_L is a material property, easy to retrieve from tables and c_p is the mean specific heat of the reactive species, that is readily available from Chem1D.

For a non-reacting flow the temperature is calculated with the help of the definition of Favre averaged total chemical enthalpy:

$$\tilde{H} = \tilde{h}_0 + \int_{T_0}^{T} \bar{c_p} dT + \frac{1}{2}\tilde{u}^2 + \tilde{k} \tag{5.3}$$

To account for mixing, h_0 is set to the enthalpy h_f of the fuel entering the combustion chamber. For the oxidizer stream h_{Ox} is taken as reference enthalpy. Assuming Lewis number equal to unity the enthalpy can be written in form as a function of mixture only:

$$h_{mix} = h_f + \mathcal{Z}(h_{Ox} - h_f) \tag{5.4}$$

Then the total enthalpy reads:

$$\tilde{H} = \tilde{h}_{mix} + \int_{T_{0,mix}}^{T} \bar{c}_{p,mix}\, dT + \frac{1}{2}\tilde{u}^2 + \tilde{k} \tag{5.5}$$

For the mixture fraction a transport equation can be written that is formally identical to the convective and diffusive terms of the enthalpy equation (5.1)

$$\frac{\partial \rho\mathcal{Z}}{\partial t} + \frac{\partial}{\partial x_j}\left(\rho\tilde{u_j}\tilde{\mathcal{Z}}\right) = \frac{\partial}{\partial x_j}\left(\overline{\rho D\frac{\partial \mathcal{Z}}{\partial x_j}} - \widetilde{\bar{\rho}u_j\mathcal{Z}}\right) \tag{5.6}$$

Compressibility effects, that account for transformation of kinetic into thermal energy are not accounted for. If this function for the mixture fraction is solved in the CFD code the enthalpy of the mixture can be obtained from (5.4). The according enthalpy h_{mix} is stored in the FGM table. The temperature due to combustion is also a function of the progress variable and is as well tabulated in the FGM tables. It is read out as a function of $\mathcal{Z}$ and $\mathcal{Y}$ (and the according variances in case of turbulent flow).
If there are no compressible effects, the result for $\tilde{h}$ derived from the total enthalpy equation (5.1) by just subtracting the kinetic and turbulent kinetic energy from $\tilde{H}$,

$$\tilde{h}_{CFD} = \tilde{H} - \frac{1}{2}\tilde{u}^2 - \tilde{k}\,, \tag{5.7}$$

should be the same as the enthalpy retrieved via the mixture fraction (5.4). If compressibility effects are present the difference:

$$\Delta h = \tilde{h}_{CFD} - h_{mix} \tag{5.8}$$

is a measure of the compressible effects. By this procedure the influence due to compressibility can be separated from the influence of combustion effects. The temperature difference ΔT due to compressibility may then be calculated via

$$\Delta T = \frac{\Delta h}{\overline{c_p}}. \tag{5.9}$$

The specific heat $\overline{c_p}$ is the averaged specific heat c_p for the temperature region between the temperature read from the FGM table, T_{Comb}, and the overall temperature $T = T_{Comb} + \Delta T$, as it holds:

$$\Delta h = \int_{T}^{T_{Comb}} c_p \, \Delta T \tag{5.10}$$

Since the specific heat c_p depends on the temperature, its value is not straightforwardly taken from the table, but corrected using its temperature gradient defined by:

$$\frac{dc_p}{dT} = \frac{c_{p,Comb} - c_{p,ref}}{T_{Comb} - T_{Ref}} \tag{5.11}$$

The existing FGM table is not suited to deliver a reference state. T_{Ref} and $c_{p,Ref}$ should take information on mixture fraction and reaction progress into account. Therefore, a second FGM table (FGM reference table) is calculated. Here, the temperature of the mixture, that is given as boundary condition for the Chem1D calculations, is chosen to be 100 - 200 K less than for the actual FGM table. By this the thermal energy loss due to compressibility effects is taken into account while calculating the FGM table and the gas properties within.

The averaged $\overline{c_p}$ for the temperature range in which the compression is taking place may finally be calculated as:

$$\overline{c_p} = c_{p,Comb} + \frac{1}{2} \cdot \Delta T \frac{dc_p}{dT} \tag{5.12}$$

Note that for a compressible flow with increasing velocity as present in an NGV the ΔT will be negative. The overall temperature T will be in between the combustion temperature and the reference temperature for the reference state. Clearly equation (5.12) is only a linear approximation. But considering the progression of c_p over T in figure 2.3 it seems to be a reasonable choice. As a c_p gradient is used, the calculated $\overline{c_p}$ in regions of compression in which ΔT is positive will be extrapolated values. When choosing the temperature for the FGM reference table the optimal value will cause a flame temperature drop according to the maximal expected temperature drop due to compressibility. Some estimating examples are given in section 5.5.1.

Finally, the overall temperature, including both compressible and combustion effects is calculated via:

$$T = T_{Comb} + \Delta T\,. \tag{5.13}$$

This temperature is fed back into the CFD solver and used to calculate the total enthalpy in the next iteration. Also the density will depend on this temperature by using the ideal gas relation as done for the non-reacting compressible solver.

5.2 Gas Properties

The averaged molar mass is taken from the chemistry table, as it is a function of mixture fraction and progress variable. The variances of both variables have to be taken into account when solving for turbulent flames. As explained in section 2.3 for PPDF-FGM modeling not only the mixture fraction, but also a progress variable and both their variances are solved in the CFD code and define the combustion process. The same holds for the isentropic exponent γ. But it is not included in the Chem1D calculations and therefore not available for beta - integration. To obtain a consistent γ, one needs to recall the thermodynamic relation of the Gas constant R_M:

$$R_M = c_p - c_v \tag{5.14}$$

As R_M of a substance is given by:

$$R_M = \frac{R}{M} \tag{5.15}$$

with the universal gas constant R and the molar mass M. Inserting the definition of the isentropic exponent $\gamma = \frac{c_p}{c_v}$ into equation (5.14) and some transformation, one will end up with

$$\gamma = \frac{1}{1 - \frac{R}{M\, c_p}} \tag{5.16}$$

If M and c_p are taken from the FGM table, they are functions of $\mathcal{Z}$, $\mathcal{Y}$ and their variances, so will γ.

5.3 Differences to the Incompressible Code

In the incompressible version of PRECISE-UNS and in general while using the PPDF-FGM approach for modeling the combustion process there will be regions in the flow-field, in which the gas mixture is outside the flammability limits. For these mixture fractions no flamelet solution can be calculated with Chem1D as described in section 2.3.4. However, the PDF table (section 2.4.3) is computed for the mixture fraction and progress variable space from 0 to 1. If the last flamelet solution from Chem1D is given for a mixture fraction of $\mathcal{Z} = z_{limit}$,[1] one more integrated solution is added to the PDF-table for which $\mathcal{Z} = 1$. Here the gas properties of the pure fuel are stored. For any value of mixture fraction in between z_{limit} and 1 the according gas properties have to be interpolated. This interpolation is handled within the pre-integration tool and accordingly in Precise-UNS. All properties (temperature T,enthalpy h, species concentrations Y_k, source terms S_k and gas properties M, cp) are interpolated linearly, except density, that is interpolated with its reciprocal. This is only a first order interpolation and therefore a source of errors. Other authors use the reciprocal value for the molar mass and the specific gas constant as well [61]. This will lead to more precise values. Only the density is fed back to the CFD solver and will influence the velocity field. All other values are passive scalars.

The compressible algorithm is using the same interpolation and integration tools and routines. But here M, γ, c_p and the temperature are fed back to the CFD solver as explained above. The density on the other hand is calculated by the ideal gas law **after** the influence of the reaction and the compressibility effects are added. Here M from the table is used. As the interpolation for M is different to the interpolation used in the incompressible version of the code for ρ there will be deviations in the calculated density if an incompressible combustion is calculated with the two different versions, incompressible and compressible. The deviations are investigated and discussed using the example of an incompressible flame calculation in section 6.4.1.

[1] For example $\mathcal{Z} = 0.089$, which is approximately the value for methane combustion at atmospheric conditions

5.4 Boundary Conditions for Coupled Calculation

At the inlet two influences have to be accounted for. The enthalpy $h_{\mathcal{Z}}$ due to the mixture of fuel and oxidizer and the heat release $\Delta\tilde{h}$ due to compressibility as explained above. The first step is to calculate the temperature at the inlet due to the given total temperature at the inlet as for the non-reactive code:

$$T_{inl} = T_{tot} - \frac{(\gamma - 1)(\mathbf{u}^2)}{2\,\gamma\,R} \tag{5.17}$$

To estimate $\Delta\tilde{h}$ due to compressibility the same procedure is followed as explained above within the flow domain.

$$\Delta\tilde{h} = \overline{c_p}\,(T_{inl} - T_{Comb}) \tag{5.18}$$

By adding up the influence from mixture and compressibility the total enthalpy at the inlet becomes:

$$H_{tot,inl} = \tilde{h}_{Fmix} + \Delta\tilde{h} + \frac{1}{2}\tilde{\mathbf{u}}^2 + k \tag{5.19}$$

5.5 Discussion

The separation of the compressible from the reacting influence on the temperature and enthalpy (equation 5.8 and 5.13) includes an important assumption when using a tabulated chemistry approach that needs to be discussed.
When calculating the chemistry with Chem1D some assumptions are made. Only one pressure is set as boundary condition during the calculation, as the FGM method was derived for incompressible flow. When the flow is entering the NGV it is accelerated until it reaches the smallest area within the passage (throat). As a consequence the pressure increases. Further downstream the flow expands and the pressure decreases. Using the same FGM table for the whole domain ultimately leads to a discrepancy to the assumed pressure condition set for the flamelet calculation. Especially on the suction side of the NGV the pressure decrease is large. The deviation will lead to a deviation in reaction products and temperature calculation. Premixed flamelets for kerosene combustion were calculated for different pressures in Chem1D to estimate the resulting deviations. The used mechanism is a kerosene mechanism from the University of Heidelberg,[2] that was validated for lean premixed flames up to 20 bar.

[2] It was provided to Rolls-Royce within the project LES/PDF-ECT (Low Emission Systems Simulation Procedures for the Development of Fuel Efficient Combustor Technology), project number: BE 95-1927 by the University of Heidelberg.

Influence of Pressure on the Flame Temperature

Calculations were performed for stoichiometric conditions and AFRs that correspond to simulated take-off and a condition in between (AFR $\approx 22.1, \mathcal{Z} = 0.04525$). It was observed, that with an increasing AFR influences of pressure on flame temperature decreased. Therefore, results for the approximate overall AFR at simulated take-off[3] (AFR $\approx 40, \mathcal{Z} = 0.025$) of the calculated engine in chapter 7 are presented only. The results for stoichiometric and cruise conditions are given in the Appendix. For CTI applications take-off conditions are decisive as it is the richest condition that will be present in the engine. If influences at these conditions are negligible they also will be for all other flight conditions.
In figure 5.1 the influence of the static pressure on the flame temperature is shown. The difference is about 0.2 Kelvin between the flame temperature at 6 bar and at 12 bar,

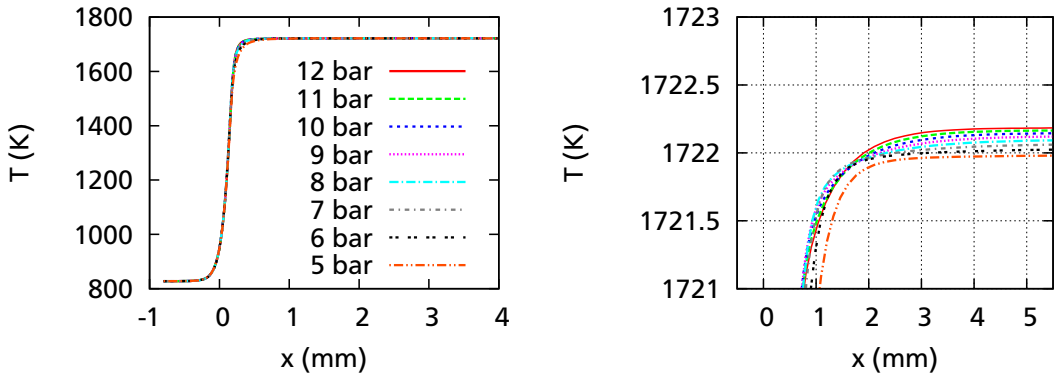

Figure 5.1.: Influence of pressure on flame temperature, right plot zoomed, colormap same as in left plot

which is less than 0.02 % of the actual temperature. These are roughly the conditions that are assumed for the final test case of this thesis. For jet engines operating at higher pressures, first the expected pressure drop has to be estimated. It is the assumed that at the inflow of the NGV the Mach number is 0.1, while at the exit a Mach number of 0.98 is present. The isentropic coefficient is assumed to be $\gamma = 1.3$. Furthermore, a total pressure loss of 5 % within the NGV is presumed. Using the gas dynamics equation (2.90) the pressure drop within the NGV can be calculated via:

$$\Delta p_{stat,NGV} = p_{in} \left[1 - 0.95 \left(\frac{1 + \frac{\gamma-1}{2} Ma_{in}^2}{1 + \frac{\gamma-1}{2} Ma_{exit}^2} \right)^{\frac{\gamma}{\gamma-1}} \right] \tag{5.20}$$

[3] Simulated take-off: The conditions at which combustion is simulated for take-off conditions in a test rig. As the rig is operated at 12 bar the simulations in this thesis are performed for this condition to be able to later compare results with experiments

In figure 5.2 the estimated pressure drop as a function of the inlet pressure of an NGV is shown. Note, that the given values are only estimated values for the boundary restrictions given above.

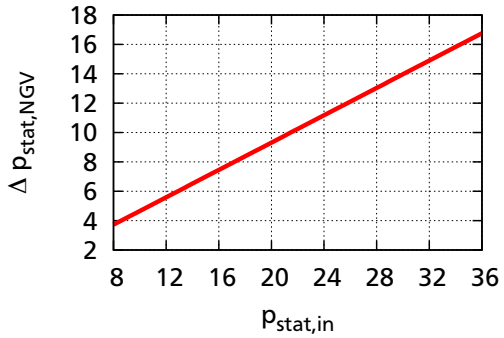

Figure 5.2.: Estimated static pressure drop in NGV of a high pressure turbine

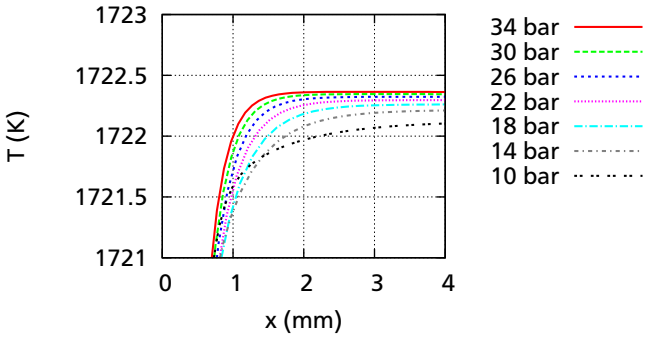

Figure 5.3.: Influence of higher pressures on flame temperature

Pressures of more than 30 bars at the NGV inlet (exit of the combustor) are common for high thrust engines. Accordingly, flamelets for higher pressures are shown in figure 5.3. For an estimated pressure drop of 14 bar at an inlet pressure of 30 bar the temperature deviation is around 0.4 K. Consequently the error by using only one pressure to set up the FGM table for simulating the combustor and NGV will always lie below 0.03 %, concerning temperature calculations. It must be pointed out, that the used mechanism is only validated for reactions up to 20 bar. Therefore, the accuracy of the results for the calculated flamelets for higher pressures is not known.

Influence of Unburned Mixture Temperature on Flame Temperature

When the flow is accelerated within the NGV the temperature of the fluid will decrease as thermal energy is transferred into kinetic energy. The mixture temperature with which flamelets within Chem1D are calculated should be adjusted. To estimate the influence of the unburned gas temperature on the flame (equilibrium) temperature, flamelets are calculated for different mixture temperatures accordingly. Figure 5.4 shows the flame temperature for a mixture with 800 K that is assumed as inlet condition. The expected temperature drop within the NGV is approximately 100 - 200 K. The influence of unburned mixture temperature is much higher than the influence of the pressure. If the FGM table is calculated using the combustor inlet temperature without taking the maximal expected temperature decrease into account, the calculated flame temperature would deviate around 150 K from the actual temperature, which is about 10 %.

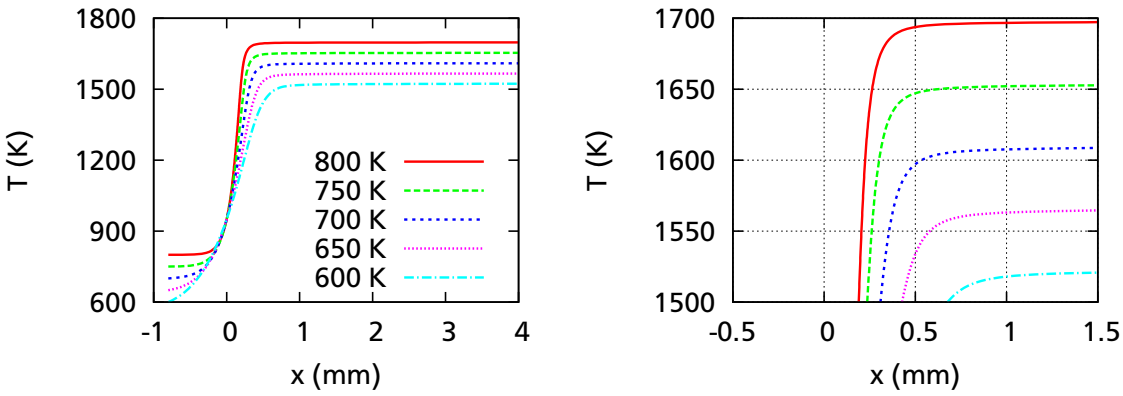

Figure 5.4.: Influence of mixture temperature on flame temperature, right plot zoomed, colormap same as in left plot

Combined Influence

The combined influence of temperature and pressure drop is shown in figure 5.5. A pressure drop of approximately 6 bar was assumed and a temperature drop of 200 K. Both the change in temperature and pressure are representative of what is expected within the NGV. The plot shows corroboration of the observations made by separately

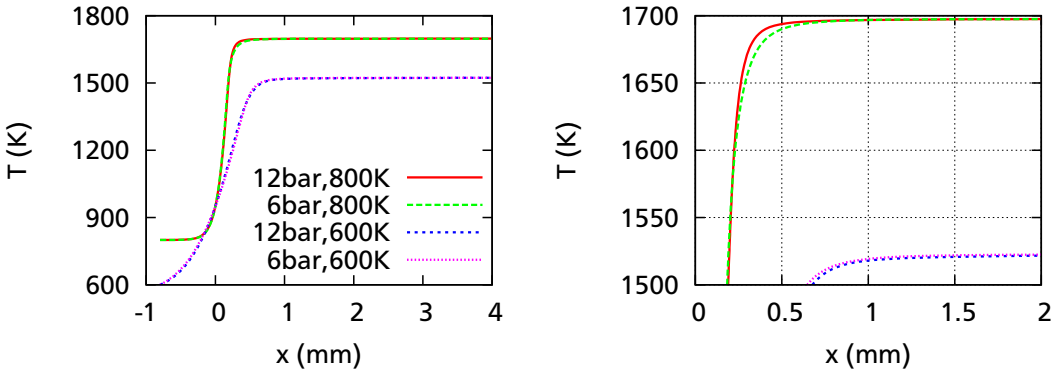

Figure 5.5.: Influence of pressure and mixture temperature on flame temperature, right plot zoomed, colormap same as in left plot

studying the influence of pressure and mixture temperature on the flame temperature. The removal of thermal energy from the flow within the NGV has a much larger impact on the reaction than the pressure drop.

Influence of Pressure on Reaction Rates

The influence of the pressure on the reaction rates is shown in figure 5.6 for CO_2 and in figure 5.7 for H_2O. The pressure was set to 12 bar, the mixture fraction to 0.025. For a pressure expected at the exit of the NGV, the maximum value of the reaction rate is only two thirds of the value for the pressure assumed within the combustor. For higher pressure levels, as plotted in figure 5.8, the influence is much smaller. For stoichiometric conditions (see Appendix) the ratio is around 1:2, while for a mixture fraction of 0.04525 the influence is in between. In the context of CTI calculations it means, that the reaction rate of the gaseous mixture will steadily decrease while it is passing through the NGV. The farther the unburnt mixture is reaching into the NGV's passages, the more the reaction rate will decrease. This effect becomes more pronounced if the mixture is non-uniform and areas of higher mixture fraction enter the NGV.

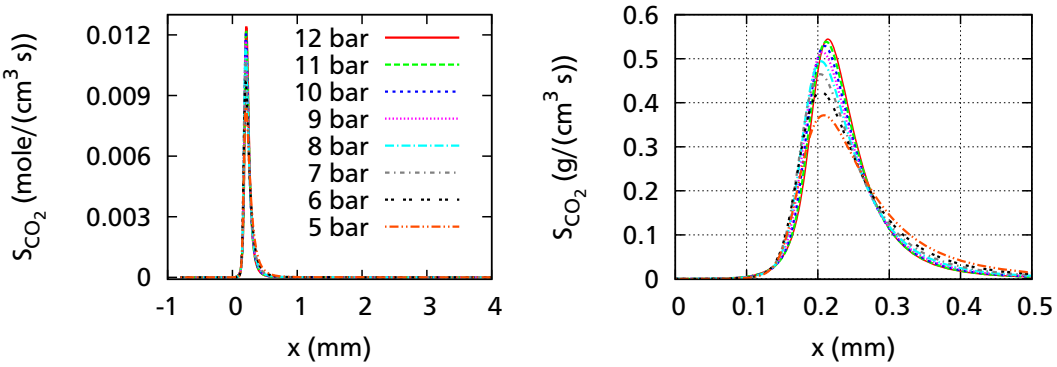

Figure 5.6.: Influence of pressure on CO_2 source term, right plot zoomed and converted into $g/(cm^3 s)$, colormap same as in left plot

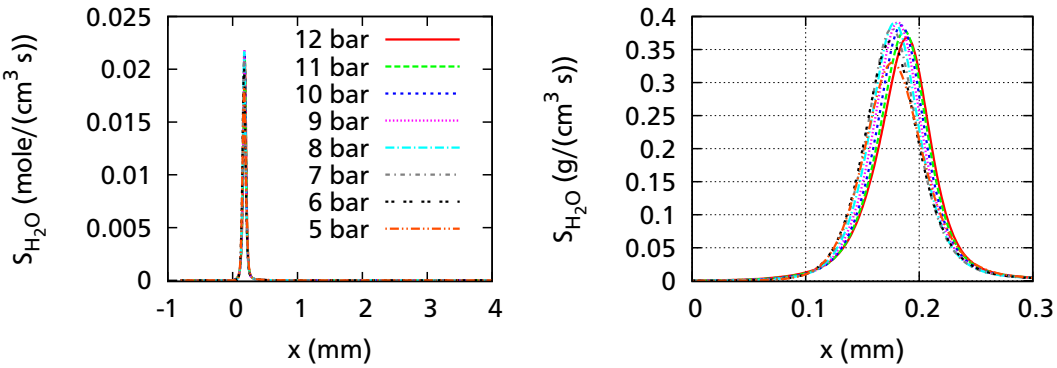

Figure 5.7.: Influence of pressure on H_2O source term, right plot zoomed and converted into $g/(cm^3 s)$, colormap same as in left plot

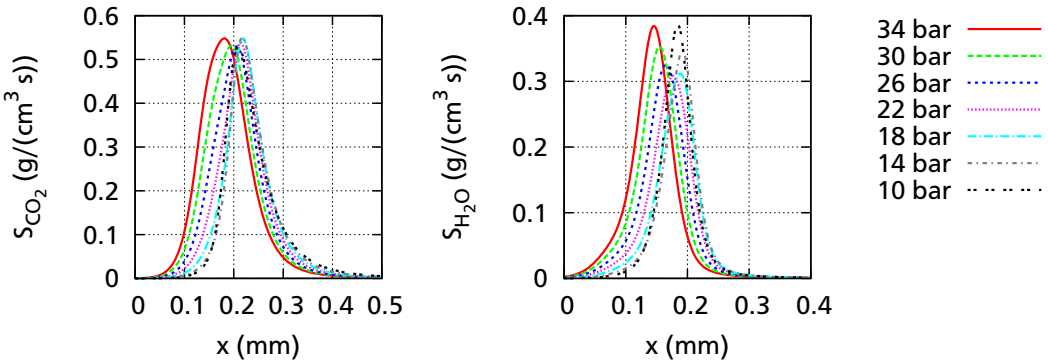

Figure 5.8.: Influence of higher pressures on CO_2 source term, left plot and H_2O source term, right plot

Influence of Mixture Temperature on Reaction Rates

The influence of enthalpy drop on the reaction rate is shown in figure 5.9 and 5.10. Again the influence of the mixture temperature is higher than the influence of pressure. For decreased mixture temperature the reaction rates will also decrease. For a temperature reduction of 100 K the peak value of production of CO_2 drops by 80 %. The influence on the production rate of H_2O is of the same order. The reaction zone at the same time becomes wider.

So by entering the NGV the progress of the reaction will be decelerated. The effect was to be expected as subtracting thermal energy from a flame is known as quenching, which slows down the reaction.

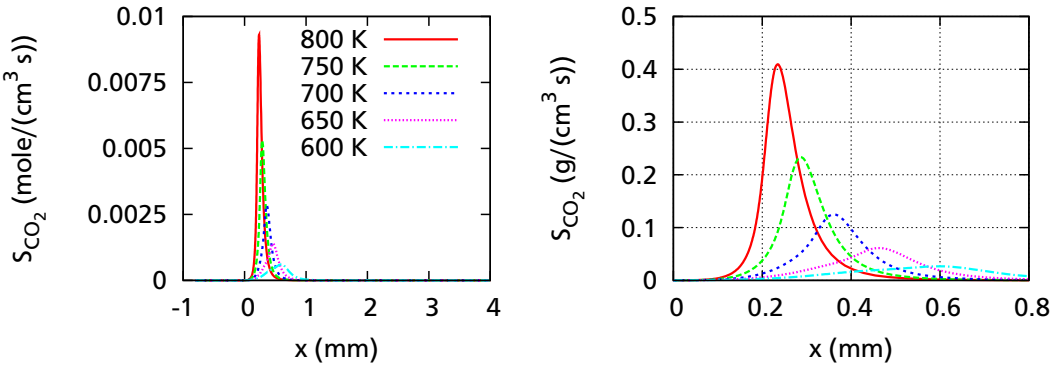

Figure 5.9.: Influence of mixture temperature on CO_2 source term, right plot zoomed and converted into $g/(cm^3 s)$, colormap same as in left plot

5.5.3 Influence of High Mach Numbers on Combustion

Another aspect is the influence of high Mach numbers on combustion. If the developed code was to be used for calculation of afterburners ram-jet or scram-jet combustors,

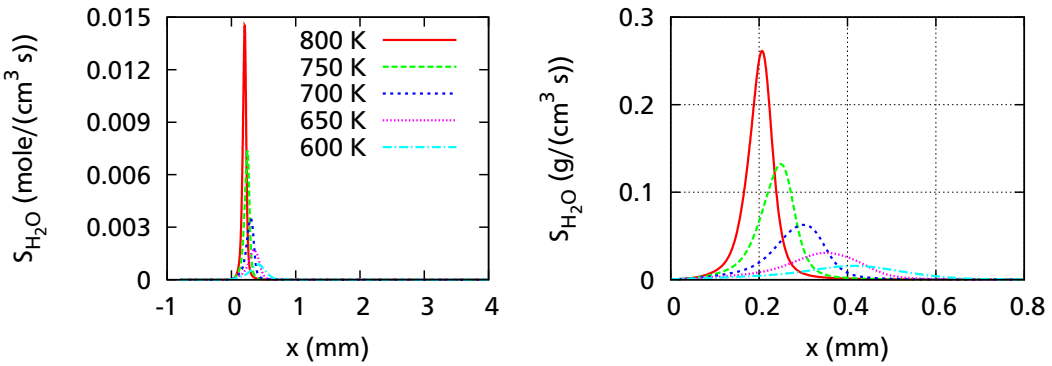

Figure 5.10.: Influence of mixture temperature on H_2O source term, right plot zoomed and converted into $g/(cm^3 s)$, colormap same as in left plot

these effects should be investigated. In these applications additional effects of compressibility on combustion are identified. The compressibility influences mixing processes and heat release [42], but also the reaction kinetics [54]. These effects however do not need to be accounted for in this thesis as such high Mach numbers are not reached in CTI context. Improved turbulence modeling is necessary, to model these influences, and also the turbulence chemistry interaction would have to be revisited. Concerning reaction kinetics probably alterations would have to be done within the chemical solver Chem1D or even needed to be added to the reaction mechanism.

5.5.4 Justification of Superposition Assumption

All the aforementioned influences are only relevant, if part of the mixture is not completely burned within the combustor before it enters the NGV. In jet-engines' design it is a requirement that the reaction has been completed before the gases enter the turbine. Burning efficiencies of combustors lie around 99.99 % for take-off condition (maximum power) and still above 99.9 % during climb and approach. Only during idle the combustion efficiency for unburnt hydrocarbons and carbon monoxide drops down to 99.8 % and 99.5 % respectively [106]. Therefore, the discussed influences will only act on less than 1 % of the reacting mixture and of course if the combustion is not as efficient as it should be.

5.6 Algorithm

The flowchart of the final algorithm compared to the non-reactive and incompressible version is shown in figure 5.11. One iteration is shown, as long as convergence is not reached the solver starts at the top again.

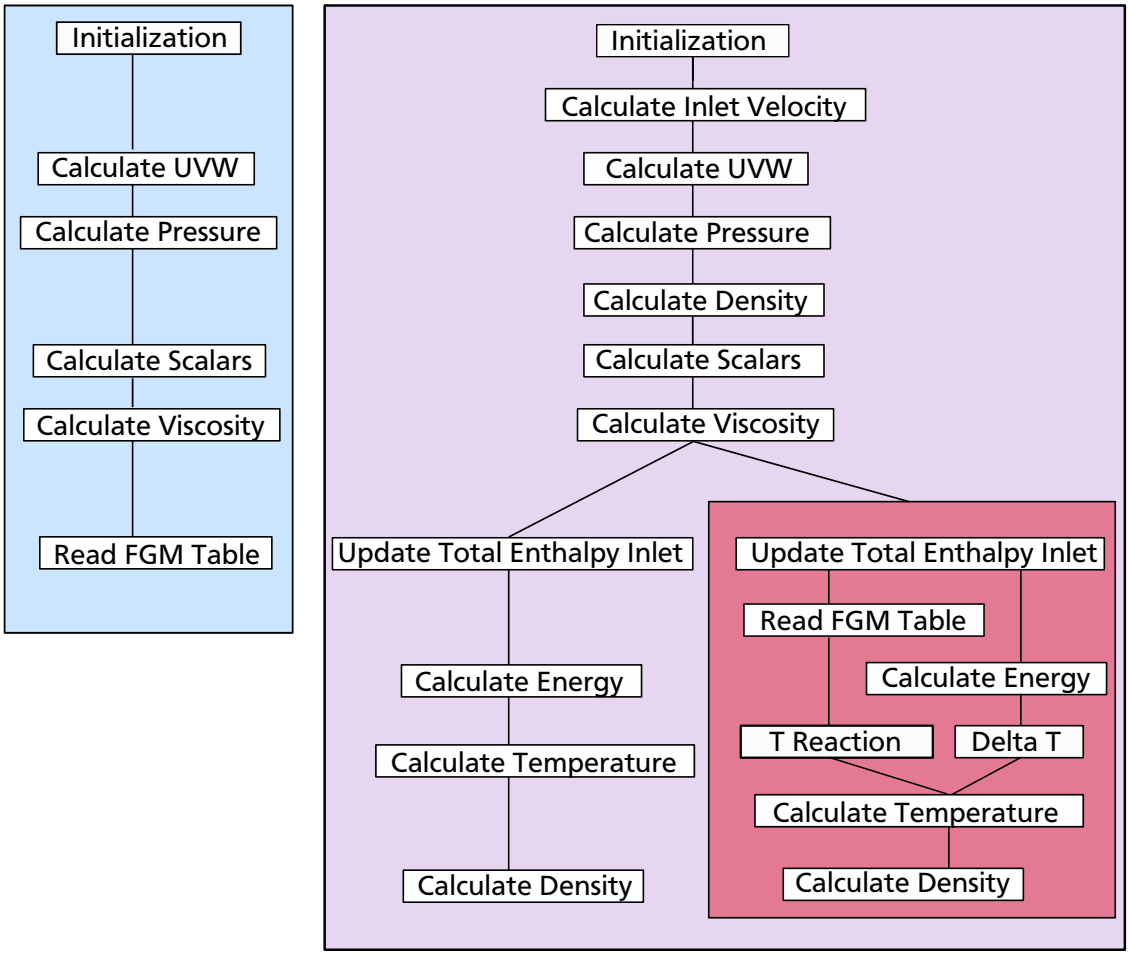

Figure 5.11.: Incompressible (blue), compressible (purple) and coupled algorithm (red).

6 Verification and Validation

6.1 Classification of Test Cases

Several test cases were chosen for verification and validation of the implementations for PUC described before. In the different test cases different criterions are focused. The order of the presented test cases is in order of increasing complexity. At first those cases are presented, in which the necessary changes to the code for calculating compressible flows are verified. Secondly, validation was performed by comparing results obtained with PUC to experimental data. Thirdly, the method for coupling the PPDF-FGM model with the extended SIMPLE algorithm is verified. Fourthly, the code was applied to real, complex geometries. Its performance is compared to other solvers and the solutions are validated using experimental data.

The software ANSYS ICEM was used for grid generation for all calculations, if not otherwise mentioned. The solution output generated by PUC can be processed in ParaView. ParaView was used to create the contour plots. The open source program gnuplot was used for plotting data profiles. The reference data were taken, if available, from tabulated data, which can be found as cited. If no tabulated data was available, the reference data were extracted from plots using g3data. In that case the exactness of the data is limited due to the extracting process by hand.

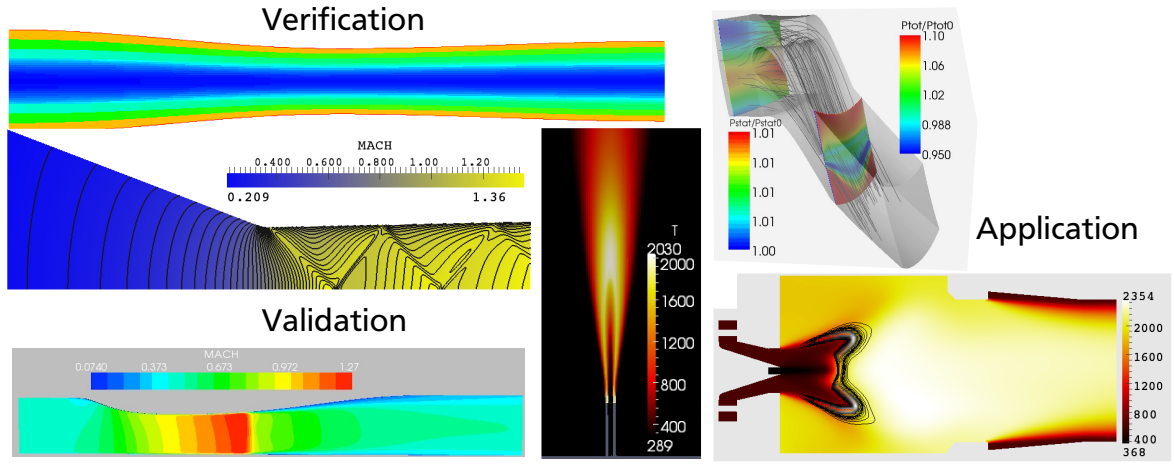

Figure 6.1.: Test cases

6.2 Verification of the New Cfd-solver

6.2.1 Converging-Diverging Nozzle

A converging-diverging nozzle (CDN) flow is suitable for the verification of different basic conditions, that have to be fulfilled according to compressible flow theory.

- The Mach number distribution can be calculated analytically. While for almost all technical flows an analytic solution to the Navier-Stokes equations is not known, here a solution is achieved using one-dimensional gas dynamics theory.
- The total pressure in an isentropic flow remains constant. The better this criteria is met, the less diffusive is the numerical implementation.

Theory of Converging-Diverging Nozzle Flow

The flow in a CDN can be calculated analytically. The one-dimensional theory for stationary isentropic compressible flow through ducts with variable cross section A can be found in many fundamental books (for example in [122], chapter 9.2). If subsonic flow enters a converging-diverging nozzle the flow will accelerate in the converging part. If the ratio of total pressure at the inlet over the static pressure at the outlet $\frac{p_{tot,in}}{p_{stat,out}}$ is high enough the flow will reach Mach=1 at the throat (smallest cross section). Depending on the pressure at the outlet the flow will become subsonic again, or will accelerate further and become supersonic. For different ambient pressures a shock will form inside or outside the nozzle. The Mach number distribution within a CDN can be calculated as a function of the nozzle's cross section distribution along the flow direction x by

$$\left(\frac{A_x}{A^*}\right)^2 = \frac{1}{Ma^2}\left[\frac{2}{\gamma+1}\left(1+\frac{\gamma-1}{2}Ma^2\right)\right]^{\frac{\gamma+1}{\gamma-1}}, \tag{6.1}$$

where A^* is the throat's cross section. The distributions of temperature, pressure and density can be determined as a function of the Mach number using the gas dynamic relations given in section 4.4, equation (4.11) and (4.13), and a respective relation for density:

$$\frac{\rho_{tot}}{\rho} = \left(1+\frac{\gamma-1}{2}Ma^2\right)^{\frac{1}{\gamma-1}} \tag{6.2}$$

Solving the equations above for a given cross section distribution would lead to implicit equations, which are uneasy to handle. Therefore, the temperature, pressure, density and cross section profiles are calculated for a given Mach Number distribution. The analytic solutions (see figures 6.4 to 6.6) were calculated using MATLAB 7.7.0.

Cross Sectional Profile

The cross section profile for the CDN is given as a function of the axial location x by:

$$A = \left[\frac{r_{in} - r^*}{2}\cos\left(\frac{x\,\pi}{x^*}\right) + \frac{r_{in} + r^*}{2}\right]^2 \pi \tag{6.3}$$

where r^* is the radius of the throat and r_{in} is the radius of the inlet cross section. x^* determines the axial position of the throat and is set to $10\,r^*$. To set up a nozzle with a smaller outlet cross section in the diverging part of the nozzle r_{in} is replaced by r_{out}. The nozzle generated is presented in figure 6.2.

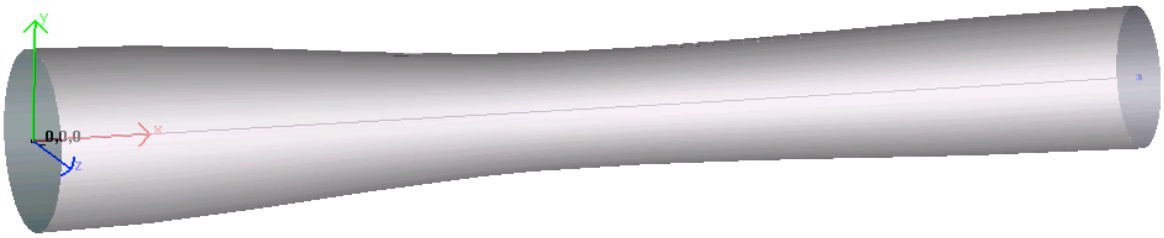

Figure 6.2.: Converging Diverging Nozzle Setup

Grid Generation

For meshing the nozzle an O-grid was chosen. In figure 6.3 the basic structure of such a grid is presented. On the right side of figure 6.3 a smoothing algorithm was applied that optimizes the angles of the grid to be as orthogonal as possible. Using the smoothing algorithm is beneficial, as the grid influence to the numerical solution can be minimized.

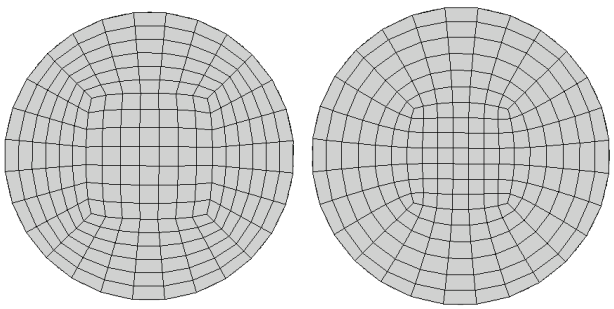

Figure 6.3.: Converging Diverging Nozzle Mesh, O-Grid, right side smoothed

The grid smoothing is done by ICEM CFD (which is a commercial tool and thus treated as a black box in the context of this thesis). It is possible to choose between different smoothing criteria but the actual final grid is controlled by optimization functions and not the user. Therefore, while conducting verification and validation, use of the grid smoother was omitted. For the test cases with more complex geometries the grid smoother was used.

Boundary Conditions - Case 1, 2 and 3

Three different flow cases were calculated for the CDN. The total pressure at the inlet was kept constant, while at the outlet three different static pressures were prescribed, with a ratio of exit pressure to total pressure at the inlet of 0.89 (case 1, figure 6.4), 0.75 (case 2, figure 6.5) and 0.16 (case 3, figure 6.6). In the first case the flow will stay subsonic throughout the nozzle, in the second case a shock will be present in the diverging part of the nozzle and in the last case the flow will reach Mach=1 at the throat and stay supersonic throughout the diverging part of the nozzle. In figures 6.4 - 6.6 two-dimensional sectional views of the Mach number for each of the three cases and the Mach number distribution along the centerline are shown. The analytical and different numerical solutions are shown, respectively. Calculations using different numerical schemes and grid resolution are given exemplary. In figure 6.5, left plot, both shown solutions do not represent the analytical solution of case 2 exactly. In this case a shock is present. The imperfect solutions are shown here to emphasize the additional attention necessary when calculating flows including shocks. The shock capturing capabilities of the newly implemented algorithm and necessary measures to improve shock resolution are to be discussed in section 6.2.2. Case 3 verifies the solving capabilities of the algorithm for flows entering the domain subsonic and leaving it supersonic. However,

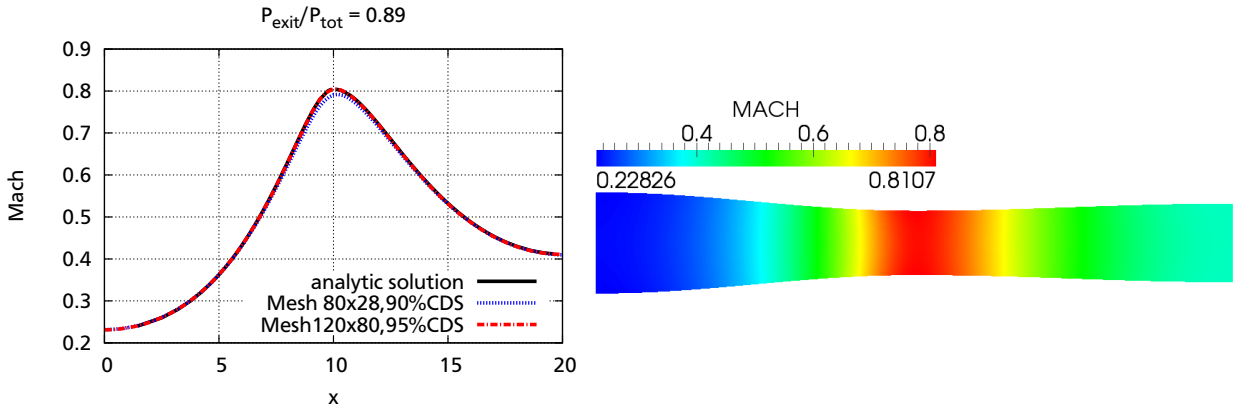

Figure 6.4.: Mach Profiles for Case 1, left side: comparison of calculations to analytical solution, right side: 2d - sectional view

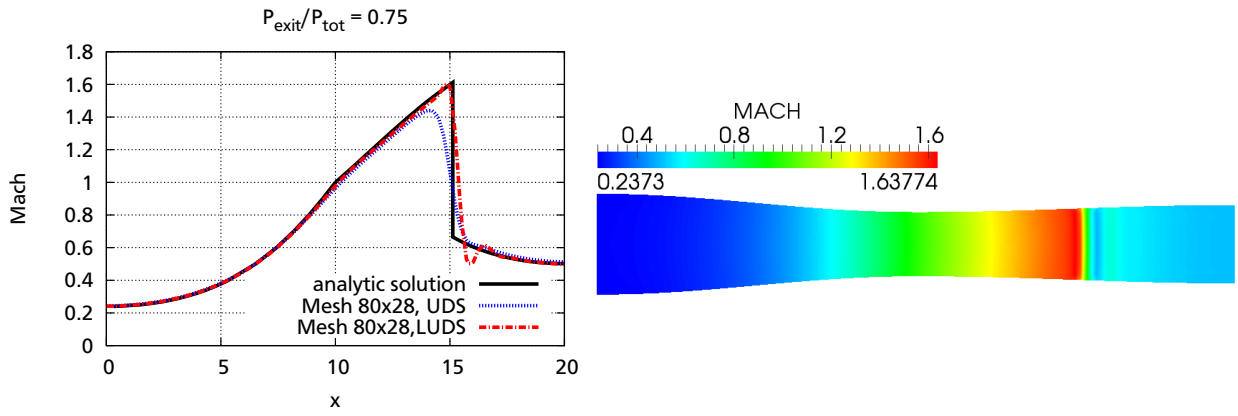

Figure 6.5.: Mach Profiles for Case 2, left side: comparison of calculations to analytical solution, right side: 2d - sectional view

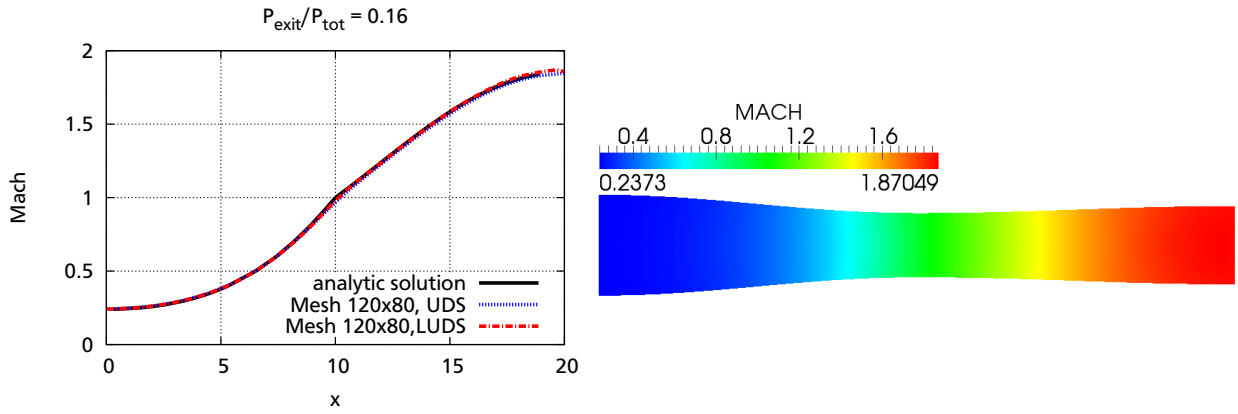

Figure 6.6.: Mach Profiles for Case 3, left side: comparison of calculations to analytical solution, right side: 2d - sectional view

here this feature shall not be discussed any further but be revisited in section 6.3.1. In principal case 1 and 3 are comparable concerning the demands on grid resolution and discretization scheme as one-dimensional gas dynamics considers the flow in both cases to be isentropic. Therefore, in the following sections different influences on the numerical solution are discussed in detail only for case 1.

Influence of Viscosity

The one-dimensional gas dynamics are deduced for isentropic flow. It is assumed that there are no losses due to friction. Therefore, the laminar viscosity was set to 1e-20 in all following simulations presented for the CDN. Case 1 was calculated with μ_{lam}= 1e-5 for comparison to investigate the influence of laminar viscosity on the total enthalpy distribution. The results are shown in figure 6.7. For this case the total enthalpy is equal to approximately $302000\,\mathrm{kJ/kg}$, so that a difference of $\Delta h = 0.86\,\mathrm{kJ/kg}$ is equal

to a difference of approximately 0.00028%, which is very low. In the calculation for the upper plot the laminar viscosity was set to μ_{lam}=1e-5 while in the lower plot the result using μ_{lam}=1e-20 is presented. It is visible that a diffusion of total enthalpy is present in the first case, while in the second case the streamline tubes (neighboring cell rows along flow direction) do not exchange energy in radial direction.

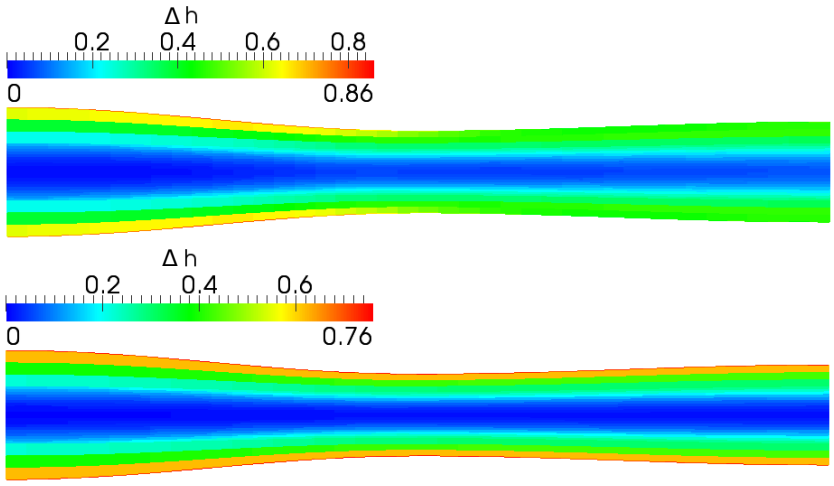

Figure 6.7.: Influence of laminar viscosity on total enthalpy diffusion, μ_{lam}= 1e-5 in the upper plot and μ_{lam}= 1e-20 in the lower plot

Sensitivity of Solution to Grid Spacing and Discretization

Two main aspects influence the solution when solving the Navier-Stokes equations numerically. On the one hand there is the influence of grid spacing. The finer the grid, the smaller the deviation to the analytic solution will (should) be (chapter 3). On the other hand, the solution is influenced by the order of the used discretization scheme.

In case 1 and 3 the flow is entirely isentropic as there is no shock within the nozzle. In theory there is no total pressure loss for such a case. If there existed a total pressure loss somewhere in the numerical solution it would be an indicator for numerical diffusion. For case 1 nine simulations were performed to study the different influences of grid spacing and convection scheme on the numerical diffusivity by evaluating the total pressure deviations within the flow domain. In figure 6.8 sectional views of the relative total pressure loss according to equation (6.4) are plotted for three different grids with three different numerical schemes used for each case.

$$\Delta_{p_{tot,rel}} = (1 - p_{tot}/p_{tot,in}) \cdot 100 \tag{6.4}$$

In the upper row calculations using UDS for each grid are shown. In the second row 90 % CDS with 10 % UDS blended and in the third row 100 % CDS was used for the

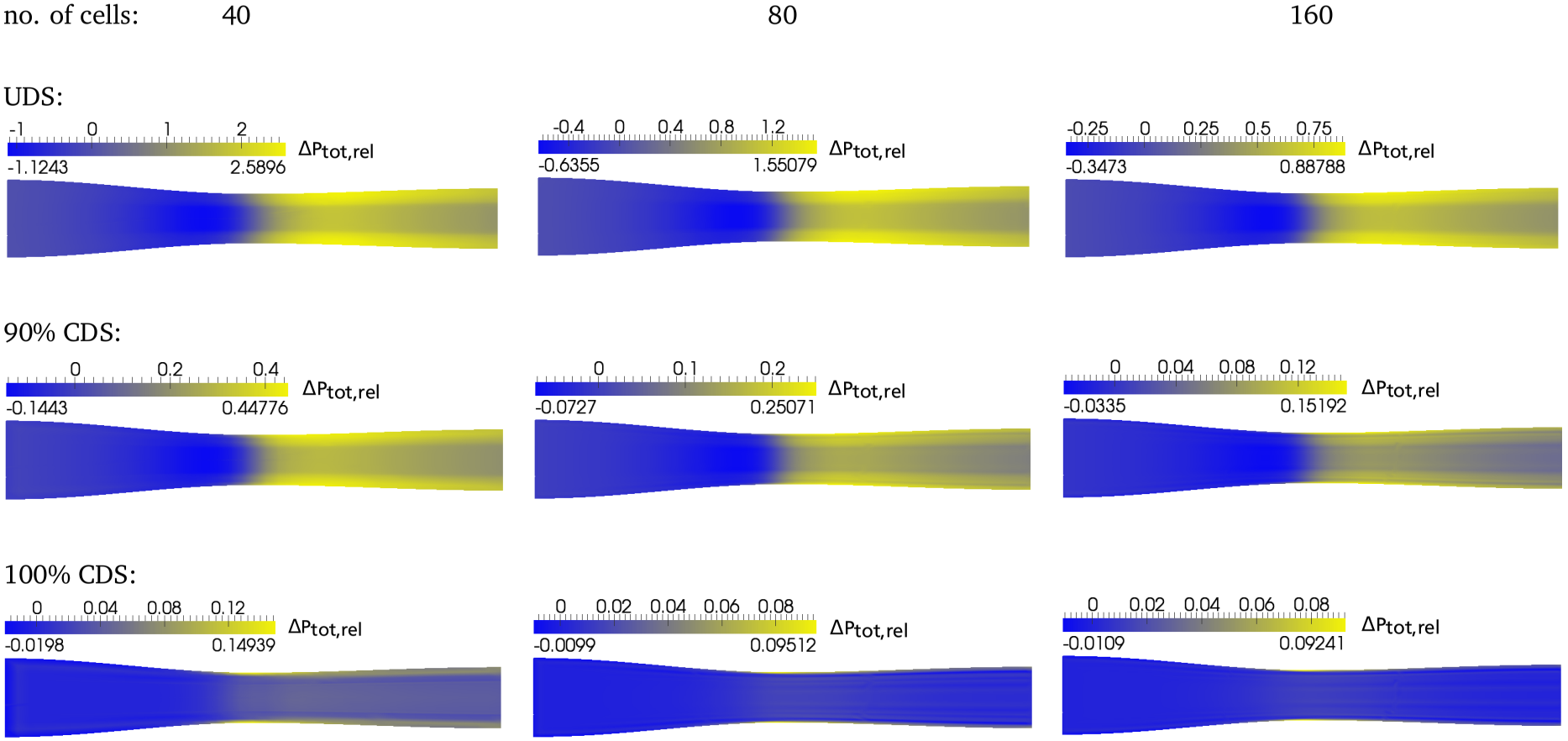

Figure 6.8.: Relative total pressure loss for different grid spacing and discretization schemes.

discretization of the convective terms. All results presented in the first column are obtained on a grid with 40 cells in stream wise (x) direction. The results in the second and third column show results from calculations on grids with 80 and 160 cells in x-direction, respectively. The number of cells in radial direction was kept constant. With increasing grid size the deviation to the analytic solution reduces, as expected. A second interesting observation can be deduced from the plots. By comparing the total pressure loss for the coarsest mesh using 90% CDS and the finest mesh using UDS it becomes obvious that increasing the discretization scheme is much more profitable than just reducing the grid spacing. With the same computational effort a much better solution is obtained.

Order of Discritization

Calculations with the three different discretization schemes were performed on a forth's grid with 320 cells in flow direction. The total pressure loss at the outlet was averaged for all grids and discretization schemes used. If the calculated error for different grids is plotted over the grid spacing (x), the slope of the line connecting the errors will give the actual order of the discretization scheme used [115]. In figure 6.9 the results for the amount of total pressure loss is shown for the three different discretization schemes used for case 1. Obviously, the UDS is not entirely first order. This may be a result of only refining the grid spacing in the flow direction.

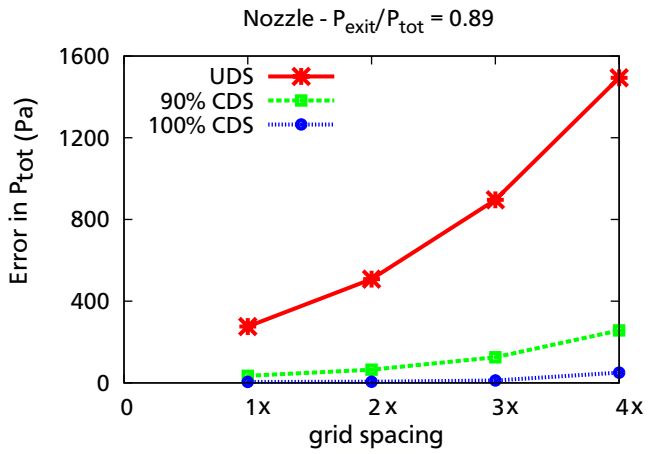

Figure 6.9.: Actual order of discretization schemes obtained for case 1

6.2.2 GAMM Bump

The GAMM Bump series, presented at the GAMM workshop in 1981 [104], was chosen for further verification of the implementation of the extended SIMPLE algorithm and the necessary boundary treatment (section 4.4). With different boundary conditions for different compressible regimes (subsonic, transonic, supersonic), these test cases are often used to validate the accuracy of the numerical schemes used to solve compressible flow. Part of the results presented here were published in [64]. The subsonic flow case is not presented here. For investigations on behavior of PUC within the subsonic regime, the CDN test case was extensively discussed in the previous section.

The GAMM bump geometry consists of a channel, of which the length is 3 times its height. Midway on the lower wall a circular arc bump is placed. Its height is 10 % of the channel's height for the transonic case. In the supersonic case the height is only 4 % of the channel's height. A schematic of this test case is given in figure 6.10.

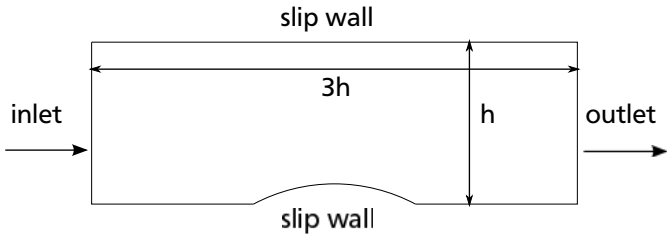

Figure 6.10.: GAMM test case setup

The flow is inviscid, thus only the Euler-equations are to be solved and at the upper and lower wall slip conditions are set. PUC is based on the Navier-Stokes equation, which describe viscous flow. Inviscid flow conditions were established by setting the viscosity to 1e-20, which is well below machine precision. Turbulence modeling was switched off. The flow conditions are determined by the flows Mach number at the inlet. For the transonic case Ma=0.675 and for the supersonic case Ma=1.65 are given as benchmark values. To reach these values in the calculation the ratio of total pressure at the inlet to static pressure at the outlet has to be prescribed as boundary condition. Assuming ideal gas properties equation 4.11 can be used to determine the needed values at inlet and outlet. The values used within this thesis are given in table 6.1.

Solution Strategy

The field was initialized with 150 m/s in the main flow direction. This value is close to the final value. The lower this value is chosen, the longer the solver needs to reach a converged solution. But the lower this value can be chosen, the higher is the robustness

Table 6.1.: Boundary conditions for GAMM test cases

	transonic	supersonic
Ma	0.675	1.65
P_{tot} at inlet	135,694 Pa	457,886.347 Pa
P_{stat} at outlet	100,000 Pa	extrapolated from inside

of the code concerning the given initial field. During the studies it was observed, that if a value lower than 50 m/s was chosen as initial velocity for the whole field the code would diverge. As convergence criterion a maximal residuum of 1e-14 for all variables was set.

Influence of Grid Refinement and Discretization Schemes

The results of Demirdzic et al. [28] were chosen as reference. This reference was chosen because Demirdzic et al. used the same test case to verify the extended simple algorithm used in this thesis. For both cases the Mach number profiles at the lower and upper wall of the channel are to be compared. Also the overall Mach number contour plots are given as reference. A grid refinement study was performed using ANSYS ICEM CFD Meshing Software for constructing the grids. All distances are given as ratios to the bump's chord. The computational domain was devided into three blocks in flow direction (x), one in front of the bump (block 1), one including the bump (block 2) and one behind the bump (block 3). The cells in x-direction were evenly distributed within block 2. For block 1 and 3 the first cell next to block 2 was spaced accordingly and a geometric law was used to spread the cells in direction of inlet and outlet. The cells in normal direction were spaced setting the first cell to a resolution of $\Delta y = 0.005$ and a geometric law was used to distribute the rest of the cells. The grid resolution at the shock location in flow direction is given in table 6.2.

Transonic Case - Influence of Grid Spacing

A Mach contour plot of the transonic case is given in figure 6.11. The reference values for the transonic test case were calculated with 90 % CDS blended with 10 % UDS while for PUC calculations of the transonic test case a second order upwind differencing, LUDS (linear upwind difference scheme), was used for momentum equations and the MinMod Scheme was used for the total enthalpy equation. The results are shown in figure 6.12. Using PUC they converge to the reference values for increasing grid resolution. They are

Table 6.2.: Grid resolution data for transonic GAMM test case

Mesh	Δx at shock	no. of cells in block 1/3 in x-direction
40x30	0.05	10/10
60x30	0.033	15/15
90x30	0.02	20/20
140x30	0.01	20/20
280x50	0.005	30/50

in overall good agreement with the expected results. Especially behind the bump the resolution needs to be sufficiently high to maintain a low grid diffusion. With increasing shock resolution, the steepness of the shock increases. The location of the shock is not influenced by the cell spacing.

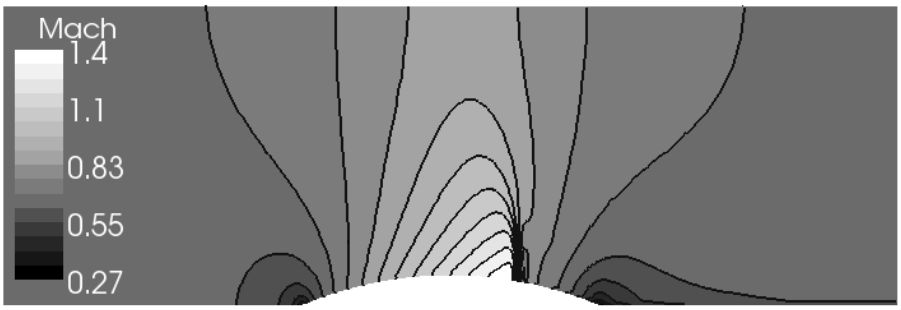

Figure 6.11.: Mach contour plot for transonic GAMM test case

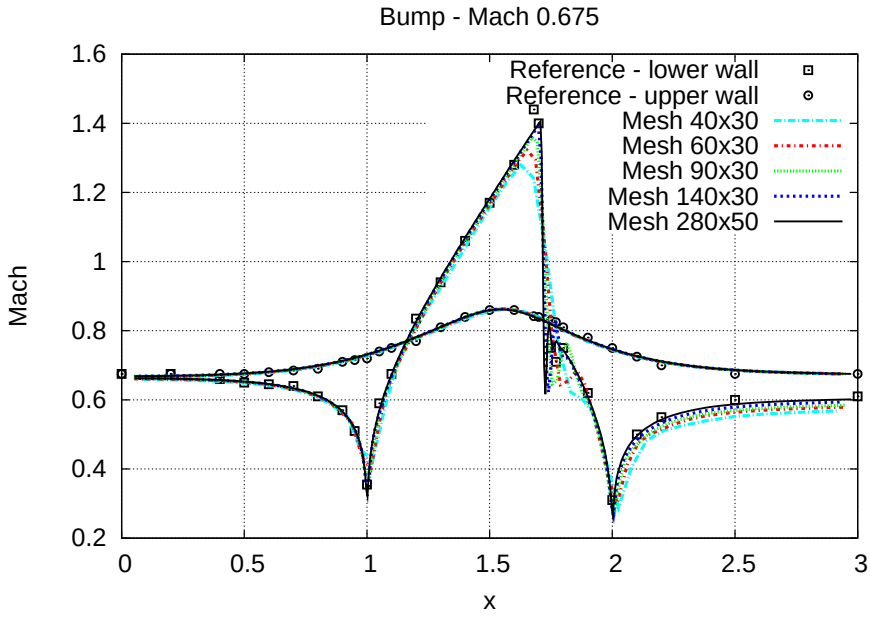

Figure 6.12.: Mach contours along upper and lower channel wall, transonic case

Supersonic Case - Influence of Discretization Scheme

The influence of different discretization schemes was investigated (UDS, 50 % CDS blended with 50 % UDS, 90 % CDS blended with 10 % UDS and LUDS) using the supersonic test case. All results presented were obtained on a comparatively fine mesh with 420x160 cells. The grid has 60 cells in block 1, 160 cells in block 2 and 200 cells in block 3 in x-direction. It is refined near the edges of the bump with a spacing of $\Delta x = 0.001$. Additionally the grid line angles were obliqued to improve shock resolution. Mach iso-contours from calculation with 90 % CDS are shown in figure 6.13. The results for different discretization schemes used are shown in figure 6.14.

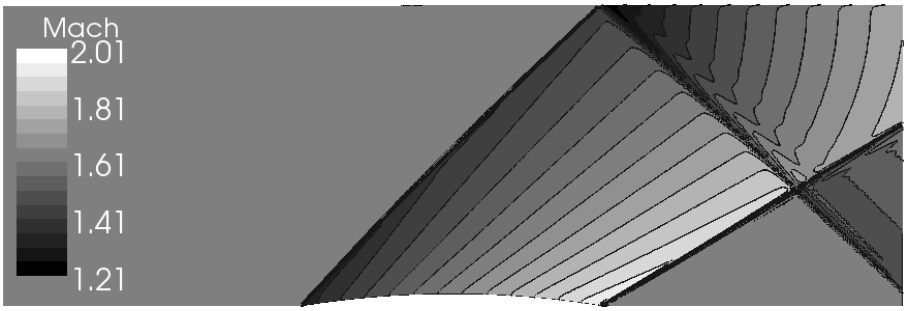

Figure 6.13.: Mach contour plot for supersonic GAMM test case

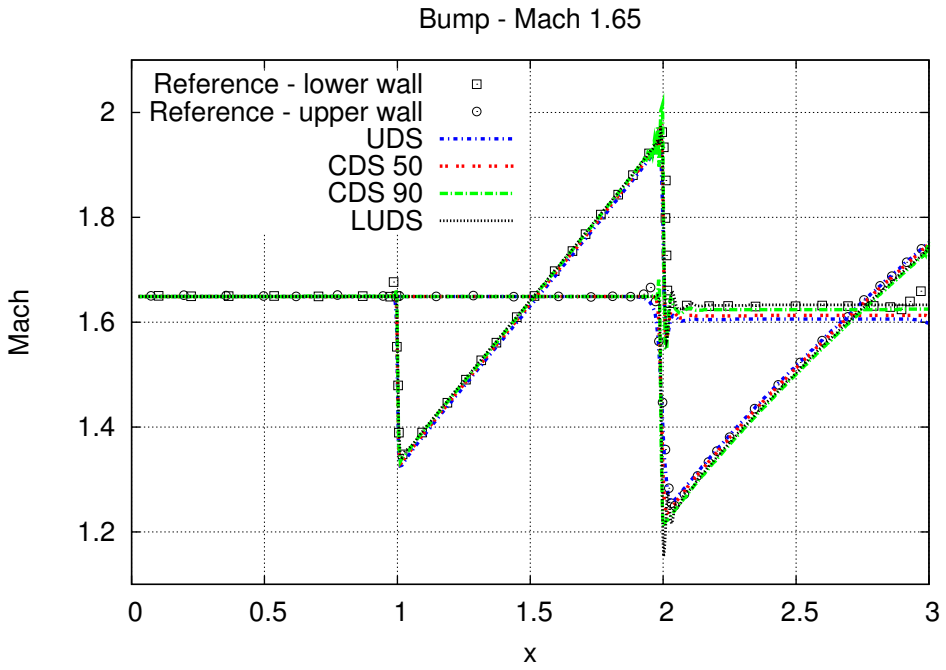

Figure 6.14.: Supersonic bump results using different discretization schemes, reference taken from [28]

With increasing order of discretization, oscillations around the shock locations increase. The strongest oscillations are obtained with LUDS at the upper wall where the shock is reflected. It reaches the same Mach number behind the shock as is obtained for discretization with 90 % CDS at the upper wall, while at the lower wall the Mach number behind the rear edge of the bump is higher. Here the discretization with 90 % CDS exhibits the strongest oscillations. The influence of numerical diffusion while using pure UDS is relatively small as the grid is sufficiently fine. Still, the Mach number behind the bump at the lower wall is the lowest using UDS and increases successively with higher order of discretization.

6.2.3 Discussion of Verification

The CDN and GAMM test case showed that the new code is able to calculate inviscid flow correctly, for subsonic as well as for supersonic inflow and outflow conditions. Shock occurring in the computational domain as well as shocks crossing the outlet boundary can be handled. The implemented boundary conditions are verified to allow the calculation of flows with the combination of boundary conditions given in table 6.3. Mach numbers up to 2.0 were verified. The ability to calculate flow with higher Mach numbers was not verified, but it is to be expected that the general solvability is not influenced. Still it should be mentioned that for highly compressible flows additional treatment of turbulence and heat transfer needs to be considered, if the flow is not assumed inviscid any more.
The verification was performed by comparing the numerical results with the analytic solutions and known Mach number profiles at channel walls from reference. The Mach number captures, due to its definition, influences of energy (temperature) and velocity. As a next step the results need to be validated to experimental data. Here, velocity profiles need to be analyzed in detail and also pressure profiles have to be investigated.

Table 6.3.: Combinations of inlet and outlet flow conditions verified for PUC

Inflow	Outflow
Subsonic	Subsonic
Subsonic	Supersonic
Supersonic	Supersonic

6.3 Validation with Experiments

The capability of the CFD-solver was tested using one-dimensional theory. Also the numerical behavior was investigated. It was shown, that the solution is sensitive to the grid spacing and the discretization scheme used. In the vicinity of a shock a proper resolution is of high importance while in regions with moderate gradients also coarser grids give good results while using second-order discretization. Now, the code shall be validated against experimental data.

6.3.1 Subsonic - Supersonic Nozzle

A two-dimensional nozzle flow was chosen for the first test case. It was studied experimentally by Mason [78] using pressure probes, measuring the pressure distribution along the walls of a supersonic nozzle. In figure 6.15 the upper half of the nozzle is shown. The geometry is more complex than just a channel with a bump, as it exhibits a sharp edge (with small radius). The flow is entering the nozzle subsonic, an obliqued shock forms at the throat that is reflected at the walls of the diverging part of the nozzle, forming a rhombic pattern. The flow stays supersonic until the outlet of the nozzle. The boundary conditions for this test case are given in table 6.4.

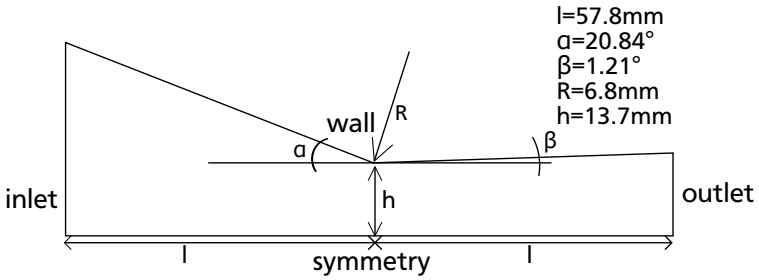

Figure 6.15.: Experimental setup of Masons diffusor

Table 6.4.: Boundary conditions for the Mason test case

P_{tot}	$P_{stat,out}$	T_{tot}	$T_{stat,in}$
199000 Pa	100000 Pa	304.79 K	239 K

Numerical Setup

Only the upper half of the nozzle was calculated, applying symmetry condition at the centerline. Calculations were performed on three different grids using inviscid assump-

tion by switching off the turbulence model and setting the viscosity to 1e-15. The finest grid 'A' has 516 cells in stream-wise direction and 80 cells in height. The middle grid 'B' has 276x50 and the coarsest grid 'C' has 177x50 cells. On each grid one calculation was performed using 90 % CDS blended with 10 % UDS and one calculation using LUDS for discretization of the convective term. Only results using the CDS blend are presented here, as no difference could be observed between the two discretization schemes. The capability of calculating viscous flow was also investigated. For the coarsest grid the spacing near the wall was adjusted to y^+-values between 30 and 70, and viscous flow was calculated using the k-ϵ model.

Solution Process

It was observed that the numerical solution process follows very much the temporal evolution of such a flow phenomena in experiments. The rhombic shock pattern behind the throat is not formed immediately but develops during the iterative process. The flow was initialized with a velocity well below Mach 1. The flow accelerates in front of the nozzle until it reaches Mach=1 at the throat due to the engaged pressure drop. The flow in the rear part stays supersonic while it forms a rhombic shock pattern. This evolution of the solution is shown in figure 6.16 by plotting the pressure distribution along the upper wall for different iteration steps (inviscid calculation using CDS blend on grid 'A'). On the right side of the same figure the according residuals are shown. The final pressure distribution is reached after 12,200 iterations. The residuals have dropped by 5 orders then. The overall mass conservation is met by 0.07 %. Another 10,000 iterations will lead to an error in mass conservation of less than 1e-11 %. This is close to the machine precision.

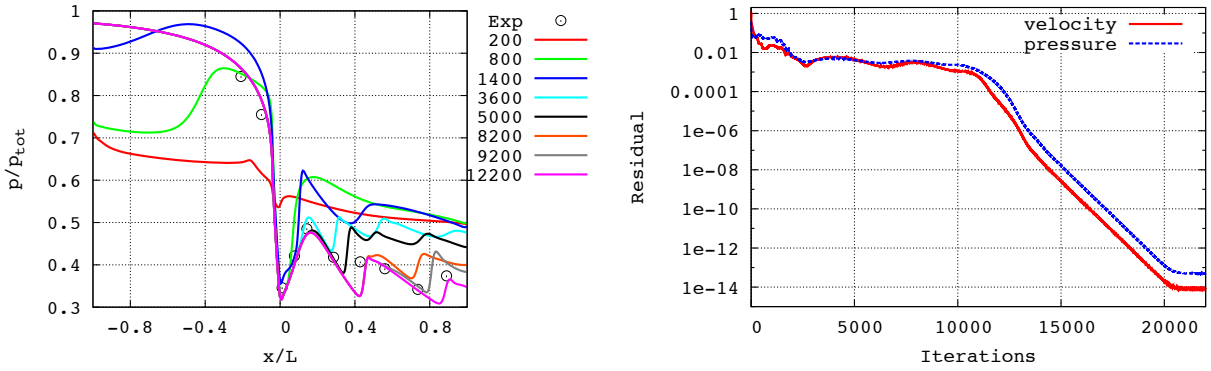

Figure 6.16.: Pressure distribution along wall for different iteration steps (left). Evolution of the solution during the computation for increased iteration steps can be followed. Residual plot for according calculation (right).

For the simulations on the coarser grids 'B' and 'C' less iterations (around 8,000 and 6,000 respectively) were necessary to reach the final pressure distribution, for the inviscid calculation as well as for the viscous calculation. Here, the pressure information needs less time to travel through the numerical domain from the outlet to the inlet which is necessary to determine the flow behavior in the front part of the nozzle. Once the first shock has established slightly behind the throat the remaining number of iterations needed for convergence scale with the number of cells behind the nozzle.

Comparison to Reference

The experimentally measured pressure distribution along the wall of the diffuser are given as reference. It was measured by static-pressure orifices along the diffuser's flaps.

Pressure Profile Along Wall

In figure 6.17 it can be seen that the calculated profiles do match the experimental pressure distribution quite well for the inviscid calculations. The solution changes slightly for the different grid resolutions. For increasing number of cells the pressure gradients at the locations at the wall, where the shocks are reflected (x/L≈0.42 and x/L≈0.85), are predicted to be steeper. The best match for the inviscid calculations is obtained on grid 'B'. It seems that in this case the numerical inaccuracy does balance the viscous dissipation that is neglected while solving only the Euler - equations. But for an increasingly fine mesh the solution should converge to the real solution, therefore viscous effects need to be taken into account. For the viscous solution less steep pressure gradients are predicted, also shown in figure 6.17. Very high resolution of the domain would be necessary for viscous flow calculations of crossing shocks. The solution of the viscous equations is further investigated in the next section.

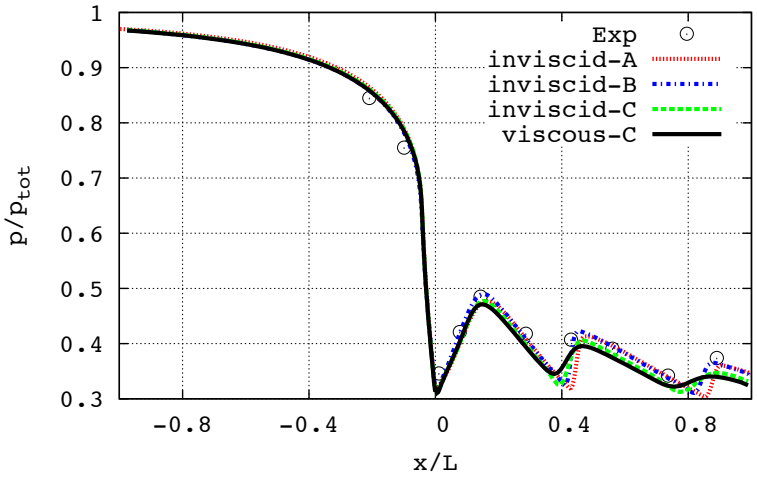

Figure 6.17.: Pressure profile along wall

Mach Number Distribution

In figure 6.18 the Mach number distribution is shown as calculated on grid 'A' and on grid 'C'. With increased grid resolution, the iso-contours lie closer together, which implies steeper gradients. The calculated shocks are smeared out on the coarse grid, especially in the rear part of the nozzle. This effect is the same as the less steep pressure gradients that were observed in the pressure profiles along the upper wall.

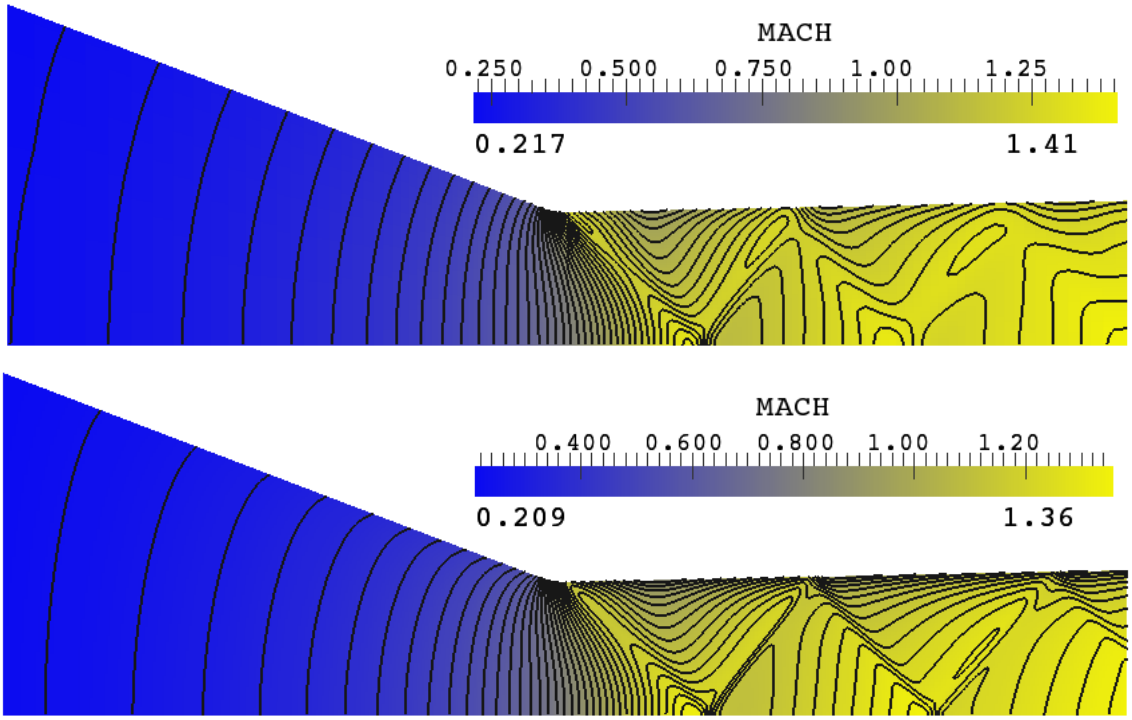

Figure 6.18.: Mach number distribution for fine mesh 'A' (bottom) and coarsest mesh 'C' (top) mesh, Mach iso-contours ranging from 0.2 to 1.4 in 0.03 intervals for both plots

6.3.2 Transonic Diffusor

The Euler assumption may be justified for airfoil design (the speed is so high that the convective term dominates the diffusive one by far) and satisfying for calculating the pressure field around the body. For combustor flows this assumption is not reasonable. Viscous effects, i.e. turbulence, dominate the flow, especially in swirling and jet flows.

One vastly explored validation test case for transonic, internal flows is the converging-diverging diffusor experimentally investigated by Sajben et al. [110, 16].

The test case is well documented on the NASA homepage [85] where different computational studies are presented, performed by Towne, Yoder, Slater and Mohler comparing different CFD-solvers and different turbulence models. In general there are three se-

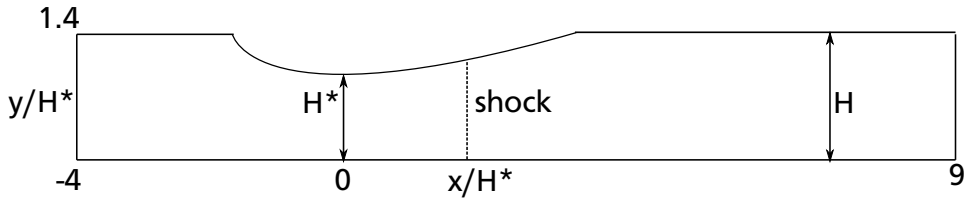

Figure 6.19.: Geometry for the Sajben transonic diffusor

tups for this flow case. One exhibiting no shock, one with a weak shock and one with a strong shock located within the diffusers throat. The strength of the shock is controlled by the static pressure at the outflow. The setup of this test case is illustrated in figure 6.19.

For this thesis the weak shock flow case was chosen, as no separation is induced by the shock. Flow separation is not representable with the code at hand, as the boundary layer is modelled with a log-law. The corresponding boundary conditions are given in table 6.5 and are taken from [85]. In the reference all values are given in american units and are converted to metric system here. The static temperature at the inlet is not a boundary condition for the calculation, but adjusts to the presented value during the solution process. A calculated Schlieren image of the flow is presented in figure 6.20, to give an impression on the flow characteristic.

The pressure distribution along the upper and lower wall are given for validation. They were measured with pressure probes. The velocity profiles at distinct locations ($\frac{x}{H^*}$) along the diffuser were measured with Laser Doppler Velocimetry [110]. This technique is calibration free and the accuracy due to 'slip' between particle and gas phase is around 1 %. Four locations are available via [85].

Table 6.5.: Boundary conditions for the weak shock sajben flow condition

p_{tot} at inlet	134999.348 Pa
T_{tot} at inlet	292 K
T_{stat} at inlet	280.14 K
angle of attack	0°
p_{stat} at outlet	110660.855 Pa

Figure 6.20.: Schlieren image of transonic diffuser test case

Solution Strategy

For reaching a converged solution in this case not much additional effort was necessary. The initialization of the field was set to 150 m/s in the main direction. But also for lower values convergence could be achieved. The given turbulence characteristics at the inflow largely influenced the results. To reach the same gradients for the velocity profiles as measured in the experiments, the intensity of turbulent kinetic energy at the inlet was set to 1 % and the turbulent length scale was set to 0.01 mm which is about one seventh of the channel height at the inlet. From the experiments it is known, that the shock is oscillating. As convergence criterion a residual of 1e-14 for velocity and pressure was chosen. Next to that the overall mass conservation was observed.

Investigation of Grid Influence

At first, the influence of grid refinement on the discretization error was investigated. For this, three different meshes were generated using ANSYS ICEM CFD Meshing Software. The grids were uniformly spaced in mean flow direction (x), with a successively doubled number of cells, from 200 to 800 cells. The spacing of the finest grid reached $\Delta \mathrm{x} \approx 0.7$ mm. In y-direction, the spacing was chosen by the following procedure: The spacing at the wall was set to $\Delta \mathrm{y} \approx 0.2$ mm to place the first cell centre within the log-layer of the boundary layer. This is equal for all three grids. The rest of the cells were distributed so that for each successively higher number of cells the grid spacing was bisected. Figure 6.21 shows a representative grid with 100 x 24 cells.

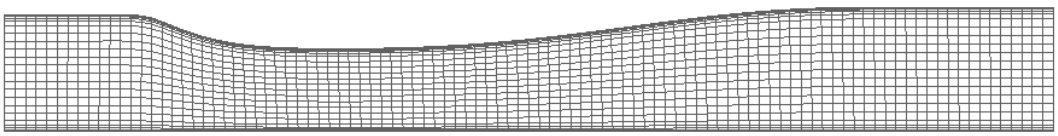

Figure 6.21.: Representative grid for Sajben diffuser test case

Pressure Calculation

Figure 6.22 shows the pressure profile along the upper and lower wall using the realizable k-ϵ model. For all grid resolutions the experimental values are matched very good. To calculate the correct pressure distribution the coarsest grid is already sufficiently fine.

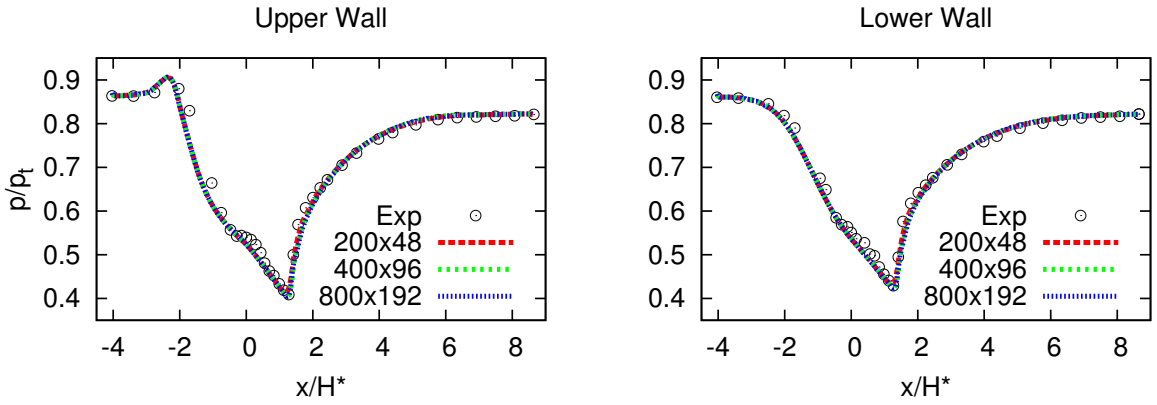

Figure 6.22.: Pressure profiles along walls for different grid sizes

Velocity Calculation

Figure 6.23 shows velocity profiles for the meshes at four distinct locations in x-direction behind the shock. The deviation to the experimental data is lower than 5% at all locations. This is in accordance with other comparisons presented on [85]. There are also results available using algebraic turbulence models and Low-Reynolds-number k-ϵ models in [39]. The results are closer to the experiments in some regions than they are in the present study, but overall comparable results (about 5 % lower velocities compared to the experimental values) are reported for this test case. Figure 6.24 shows close-up views of the velocity profiles for the different grid spacings at locations x/H^*=2.882 and x/H^*=7.493. They show that the discretization error will slightly influence the shape of the velocity profile in the region between the boundary layer and core flow. The difference in velocity between the middle and the finest grid at x/H^*=2.882 is about 0.4 m/s in this region, which is about 0.17 % of the mean velocity. In the core region the deviation is only about 0.2 m/s which is less than 0.09 % of the mean velocity. Here, an increased grid resolution will lead to a lower core-velocity. At x/H^*=7.493, far away from the shock, the difference in the core region and the region between boundary layer and core-flow for the middle and the finest grid is about 0.2 m/s, which is about 0.12 %. Between the coarsest and the middle grid the difference is about 1.3 m/s, which is about 0.7 %. For the locations x/H^*=4.611 and 6.340, the difference between middle and finest grid is less than 0.12 %. As the grid size was refined uniformly by bisecting the cells successively it is possible to perform a Richardson extrapolation to calculate the deviation to the grid-independent solution. A mean discretization error of about 0.1 % for the finest grid can be estimated for different locations.

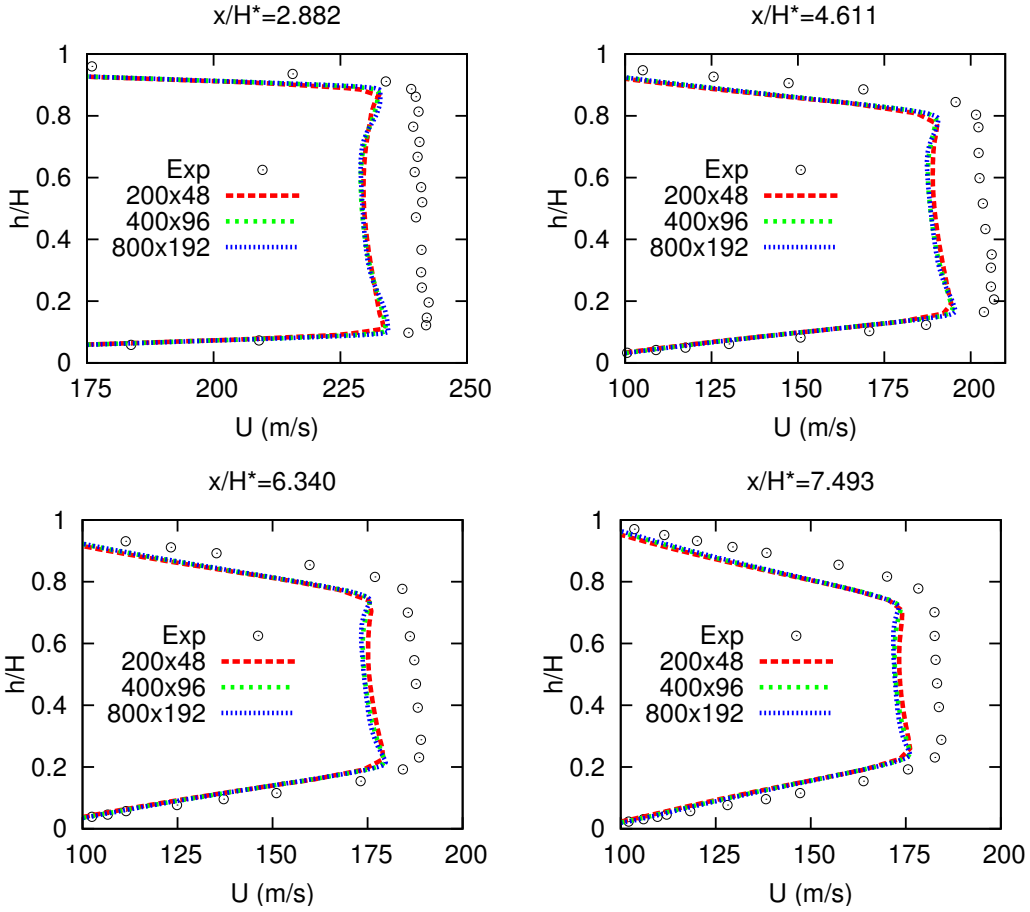

Figure 6.23.: Velocity profiles at x/H* for different grid sizes

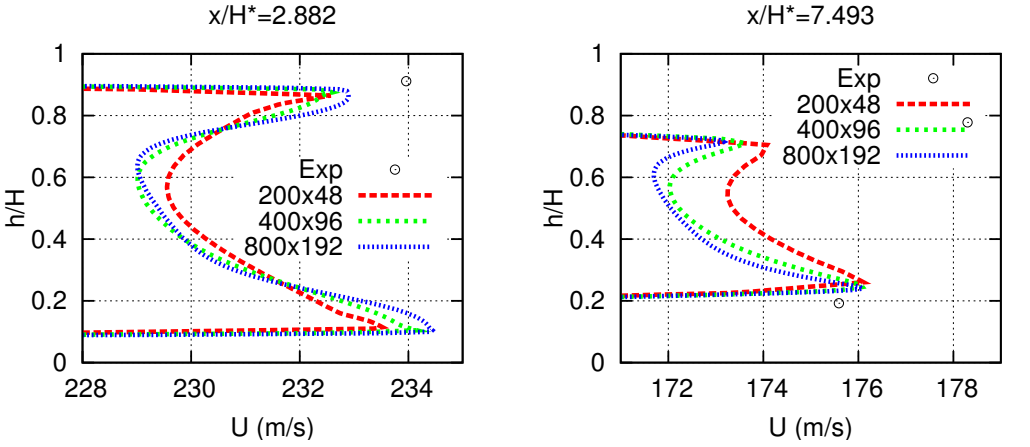

Figure 6.24.: Velocity profiles at x/H* for different grid sizes, close up view

Temperature

Density is a function of pressure, while temperature is a function of pressure and density. For incompressible calculations the temperature may be treated as a transported scalar. In the present code it is calculated using equation (2.16). While the influence of

pressure dependence can experimentally be seen in the velocity profile (which depends on the density), a closer look at the temperature profiles is beneficial to investigate the implementation of the diffusive terms in the total enthalpy equation. A calculation with Fluent (ANSYS FLUENT 12.0.16) was carried out for comparison, as experimental data are not available for temperature profiles.

The results are shown in figure 6.25. Close behind the bump there is a small deviation of 0.65 % between the maximum value of axial velocity at location $x/H^* = 2.882$. Further downstream the velocity gradient at the upper wall is slightly lower while using PUC. The temperature profiles show in general good agreement. The velocity deviation at location $x/H^* = 2.882$ leads to a temperature deviation of 0.3 K of the maximum temperature. This is about 0.1 % of the total value and in accordance with equation (2.16), used to calculate the temperature, keeping in mind that the total enthalpy remains constant. The gradients of temperature boundary layers are the same for both codes at the lower wall, while at the upper wall, where the gradient of the velocity is predicted to be a little smaller with PUC, the gradient of the temperature is consequently slightly under-predicted with PUC. The coupling between velocity and temperature profiles is in accordance with equation (2.16). This implies that the diffusion term of the total enthalpy equation is correctly implemented.

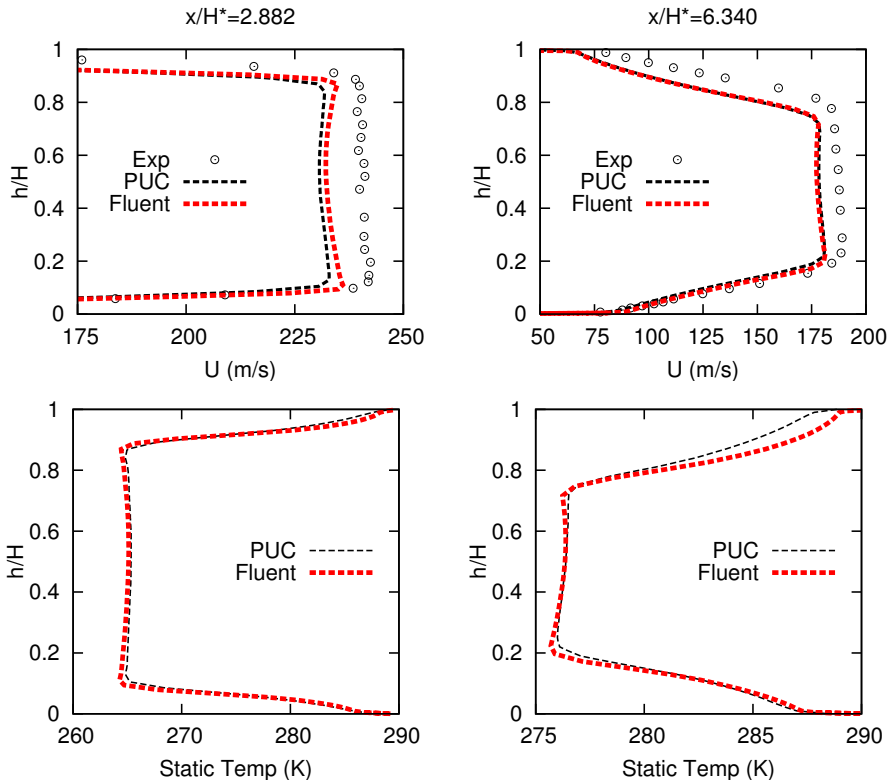

Figure 6.25.: Sajben test case - temperature and pressure profiles, comparison to Fluent

The pressure distributions along the upper and lower walls is presented in figure 6.26. They are better represented with PUC. The Fluent calculations predict the shock location slightly more downstream than the experiments. This causes the deviation in velocity and temperature profiles at location $x/H^* = 2.882$.

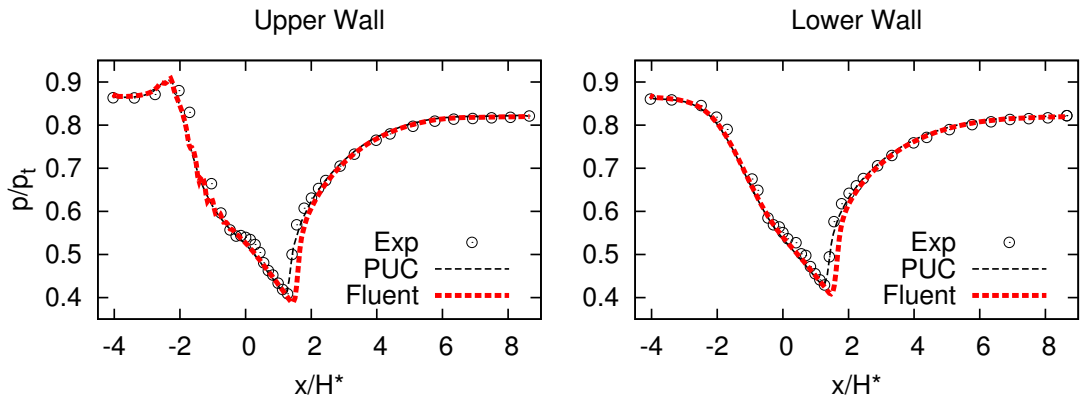

Figure 6.26.: Sajben test case - pressure profiles along walls, comparison to Fluent

Conclusion for Sajben Test Case

The obtained results for the new PUC code are in general very convincing. The deviations to the experiments are in accordance with deviations reported by other authors. There are some small differences between the profiles shapes of the results compared to Fluent. This might be expected, as small difference in numerical implementation, e.g. the interpolation of cell values onto the faces, can cause variation in the results.

6.3.3 Discussion of Validation

The Sajben and Mason test case showed that the new code gives good results for standard experiments commonly used to validate compressible codes. The pressure profile along solid boundaries is accurately predicted, even on comparatively coarse meshes. With the help of the Mason test case it was shown, that the resolution is a key factor when shocks are to be resolved. Long calculation time is necessary to obtain a converged solution for calculations of flows with complex shock patterns.
The influence of grid resolution on the calculation of velocity and temperature profiles was investigated. Richardson Extrapolation was performed to identify the grid-independent solution, which compared well to the experimental data available.
The implementation of the diffusive term in the enthalpy equation was validated by comparing results obtained with PUC to results obtained with a commercial solver. Here, it would be helpful to extend this validation with suitable data from experiments.

6.4 Verification of Tabulated Chemistry in Compressible Solver Context

Two generally separate regions can be distinguished, to verify the implemented changes for using FGM coupled with the all-Mach number SIMPLE algorithm and the total enthalpy equation. Firstly, the region of reaction. In combustor-turbine interaction the flow in this region of the combustor is assumed to be incompressible. The progress variable raises from 0 to 1. The temperature difference due to compressibility effects is equal to zero. Secondly, the compressible region behind the combustion region. In combustor-turbine interaction context this corresponds to the part of the domain, in which the fluid enters the NGV. Here, the combustion processes are assumed to have finished, i.e. $\mathcal{Y} = 1$. The temperature is only varying due to compressibility effects.

6.4.1 Reacting Flow in Incompressible Region

A standard incompressible flame was chosen for the verification of the incompressible reactive flow. The Flame D from the TNF series [6] is a non-premixed flame. A round jet is surrounded by a pilot to stabilize the reaction. Measurement data in radial direction are available up to a height of 60 diameters, d, above the outlet of the burner. The outlet boundary of the numerical domain was set 125 diameters away from the burner, which is far enough downstream to not affect the numerical result.

Application of the PPDF-FGM model in RANS context to this flame is presented by Ramaekers in [102]. He pointed out that using the k-ϵ model for this configuration does not correctly predict the magnitude of the turbulent kinetic energy. Furthermore there are some deviations in the simulated and measured reaction progress variable in his study of using premixed and non-premixed flamelets for building the FGM table. Here, premixed flamelets are used for building the FGM table. This is noted to be disadvantageous when calculating non-premixed flames with only moderate turbulence levels. Therefore, in this case it is not to be expected that the calculated profiles will match the experimental results. However, the difference between the calculated profiles and profiles known from experiments will mainly origin in the use of the k-ϵ model for a round jet flow surrounded by a pilot flow. The focus of the investigated configuration is oriented towards the comparison of the two different used SIMPLE algorithms and their respective coupling with the PPDF-FGM model, not towards the ability of predicting the velocity field correctly.

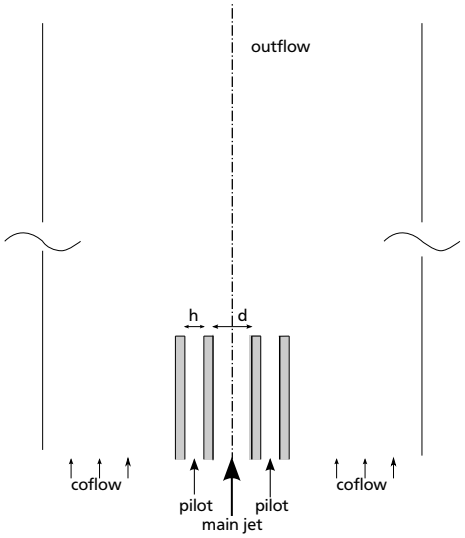

Figure 6.27.: Setup of Flame D: diameter of inner tube: d = 7.2 mm, width of pilot: h = 5.25 mm, wall thickness of inner and outer tube: 0.25 mm, 0.35 mm.

Setup

The set-up of Flame D is shown in figure 6.27. The main-jet is composed of 25% CH_4 and 75 % air by volume. This is a rich mixture, outside the flammability limits. The pilot-stream has an equivalence ratio ϕ of 0.77. The flame burns as a non-premixed flame with a single reaction zone near the stoichiometric mixture [6]. The main-jet exits the tube with a bulk velocity of 57 m/s, the pilot with 14 m/s. In the experiments the jet has a turbulent velocity profile. Thus, the pipe was included into the domain to also obtain a turbulent velocity profile in the simulation. The length was set to 13.89 pipe diameters (= 100 mm).

Boundary Conditions and Solver Settings

The Flame D is an open flame that operates at atmospheric conditions. The side boundaries of the co-flow are modeled as slip walls. There was no influence on the flow field from the side boundary, as it was placed in a sufficiently far distance. At the outflow boundary a 'von Neumann' condition (zero-gradient) is used for the incompressible flow calculation and a 'Diriclet' boundary condition (given static pressure) is used for the compressible calculation. In both calculations it is therefore necessary to place the outlet boundary far enough downstream of the domain of interest.
The flame was calculated with the incompressible SIMPLE algorithm coupled with FGM and the compressible SIMPLE algorithm coupled with FGM. The intent of performing these two variants of calculation, is to show that both approaches will lead to the same

results. It is important to apply the same boundary conditions in both simulations, so that any difference in result can be accounted to differences in the used numerical schemes. These boundary conditions include the mass-flow relation of pilot and main-jet stream as well as the velocities and the turbulence level at the exit of the burner. The difference in handling inlet boundary conditions for incompressible and compressible flows leads to difficulties in calibrating them. For incompressible simulations the velocity is given at the inlet, as well as turbulence quantities. The density, and consequently the mass flow, is a function of mixture fraction and progress variable and is read out from the FGM table. For compressible flows total pressure and total temperature are given at the inlet and static pressure is prescribed at the outlet. The velocity at the will be a result of the calculation (see section 4.4). The density is calculated via the ideal gas law.

The following procedure was therefore chosen to adjust the boundary conditions: At first, the compressible calculation was performed. Total temperature and total pressure were adjusted, so that the velocities at the inlet were as close as possible to the values given from experiments. These velocities were read out from the solution and taken as boundary conditions for the incompressible calculation. A difference however arose from the density. As explained in section 5.3 for the incompressible code the density is interpolated between the flammability limit and $\mathcal{Z} = 1$ using the mixture hyperbola. Furthermore the density is calculated within Chem1D according to the given reference pressure, that was set to 101325 Pa. For the compressible code the density is calculated via the ideal gas law at the end of each iteration. The Molar mass is interpolated linearly and the pressure at the inlet of the pipe is about 660 Pa higher than at the exit of the pipe where the combustion is taking place. For the same mixture fraction these differences caused a deviation in density of 0.69 % at the inlet. The pilot stream did not exhibit any deviation as the mixture is within the flammability limit.
To keep the mass flow constant for both calculations the velocity had to be adjusted in the incompressible calculation. The adjustments necessary to account for the difference in density at the inlet of the numerical domain were able to decrease the difference of the calculations by only a certain extend. For the incompressible calculation only one FGM table using a constant reference pressure is calculated at the beginning of the simulation and is used for the entire field, irrespective of the actual local static pressure. In the compressible calculation the local static pressure is always used for calculating the density. Therefore, somewhere in the domain there will always be a small difference between compressible and incompressible flow calculation. This is part of the incorrect assumption of constant static pressure used for the calculation of the FGM table. At the exit of the main jet finally the deviation in velocity was kept at 0.3 % and the deviation in density at approximately 0.18 %.

Results

The radial temperature profiles obtained using the incompressible and the compressible SIMPLE algorithm are shown in Figure 6.28. The experimental values are marked by triangles. The difference to the experimental values can be ascribed to using the k-ϵ turbulence model. The model is known to exhibit the Round-Jet/Plane-Jet Anomaly, that leads here to over-prediction of the spreading rate of the jet. Thus, this deviation

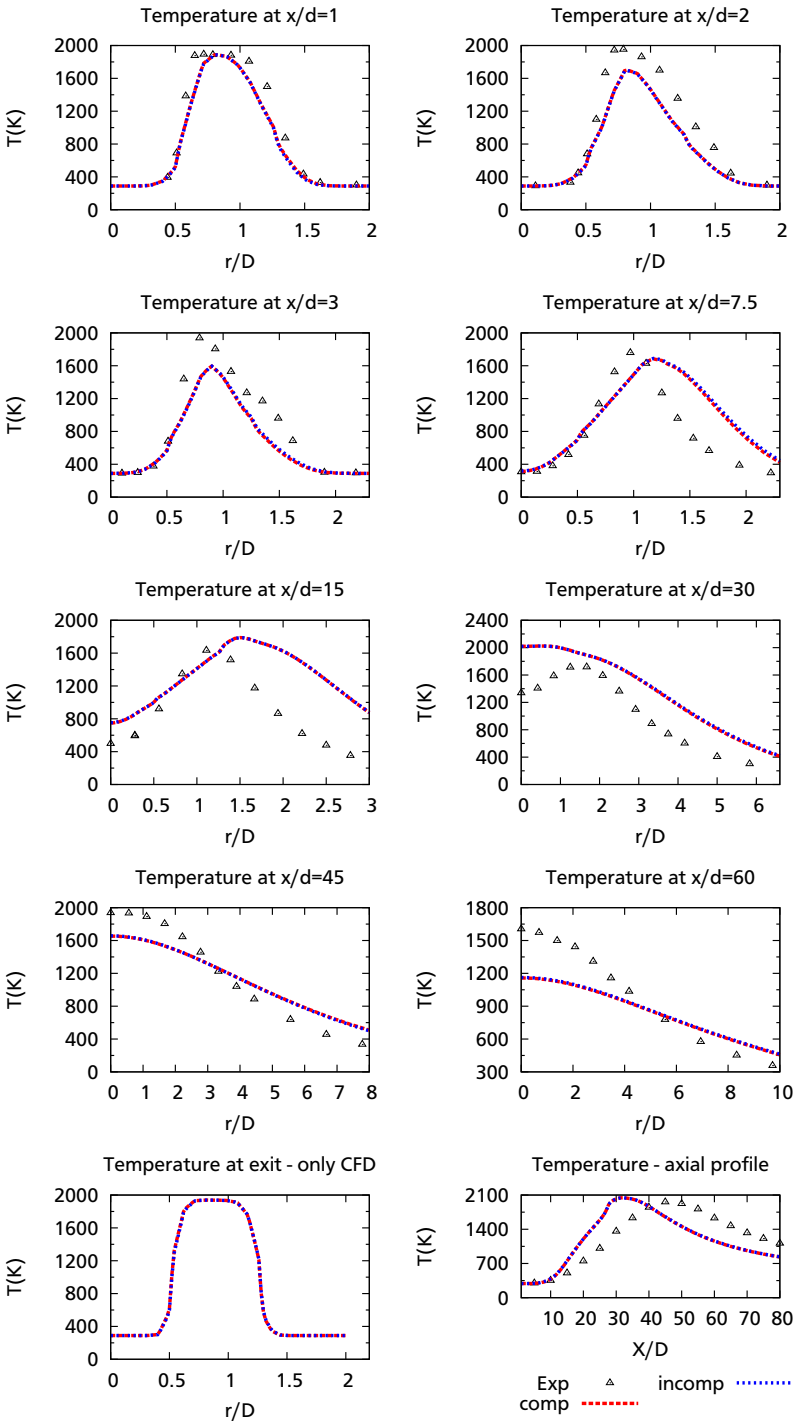

Figure 6.28.: Temperature profiles at different heights above burner exit of Flame D

was to be expected. The interesting detail of the two simulations is the congruence of the results with each other. The deviation in temperature calculation between using the standard incompressible approach and the newly developed compressible approach is well below 1 % for all measuring planes. This result was to be obtained as the Mach number is below 0.3, thus compressible effects can be neglected, and the solution algorithm should not lead to a difference in results.

6.4.2 Reacted and Non-reacted Compressible Flow

The transonic diffuser from the previous section was chosen for verification of the code in the compressible region behind a flame. Four different cases are to be considered. Two cases for non-reacted (unburnt) flow and two for reacted (burnt) gases.

Non-reacted Compressible Flow with Tabulated Gas-properties

The non-reacting flow from section 6.3.2 is re-calculated using the coupled FGM/ compressible SIMPLE algorithm (section 5). The progress variable $\mathcal{Y}$ was set to zero. For comparison with the non-reactive SIMPLE algorithm for compressible flow a second calculation was performed using matched boundary conditions and gas properties. The same procedure was used for calculating the 'burnt' case with the only difference, that here the progress variable was set to unity. The setup parameters for the two test cases are given in table 6.6.

Table 6.6.: Setup parameters for 'cold' test case

	using FGM table	standard approach
$\mathcal{Z}$	0.0427	-
$\mathcal{Y}$	0 / 1	-
M	from table M_{tab}	given as M_{tab}
γ	from table γ_{tab}	given as γ_{tab}
cp	from table cp_{tab}	given as cp_{tab}

Results

The Mach number is a function of the velocity, the temperature and the gas constant γ. For the correct calculation of the velocity the density has to be correct. The mass-flow rate is determined by the pressure drop from inlet to outlet. If the Mach number for the two calculations is the same, the mass-flow is equal. The Mach number profile at the

inlet is shown for the 'unburnt' and the 'burnt' case in figure 6.29. Within the domain the temperature should be the same for both cases. This is the case as shown in figure 6.30.

For both calculation methods, the standard compressible algorithm and the coupled FGM/compressible algorithm, exactly the same results are obtained. That shows, that the coupling algorithm works well in the compressible region in case of unburnt or fully burnt fuel/air mixture.

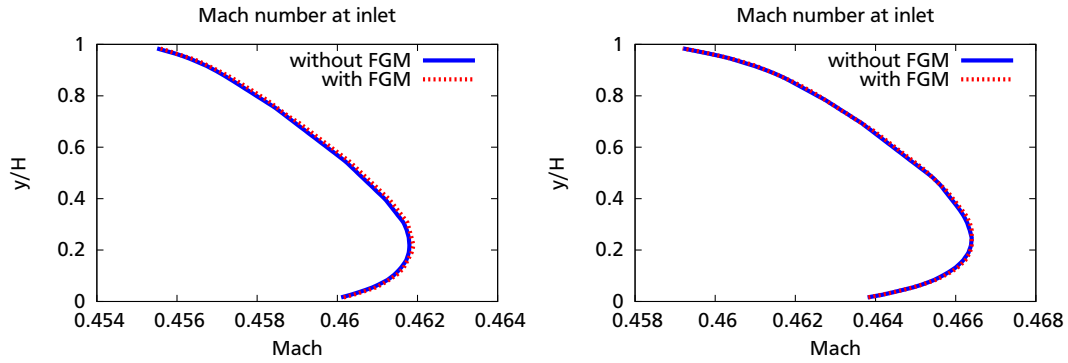

Figure 6.29.: Mach number profile at inlet of the diffuser, with and without using tabled chemical data, right: unburnt case, left: burnt case

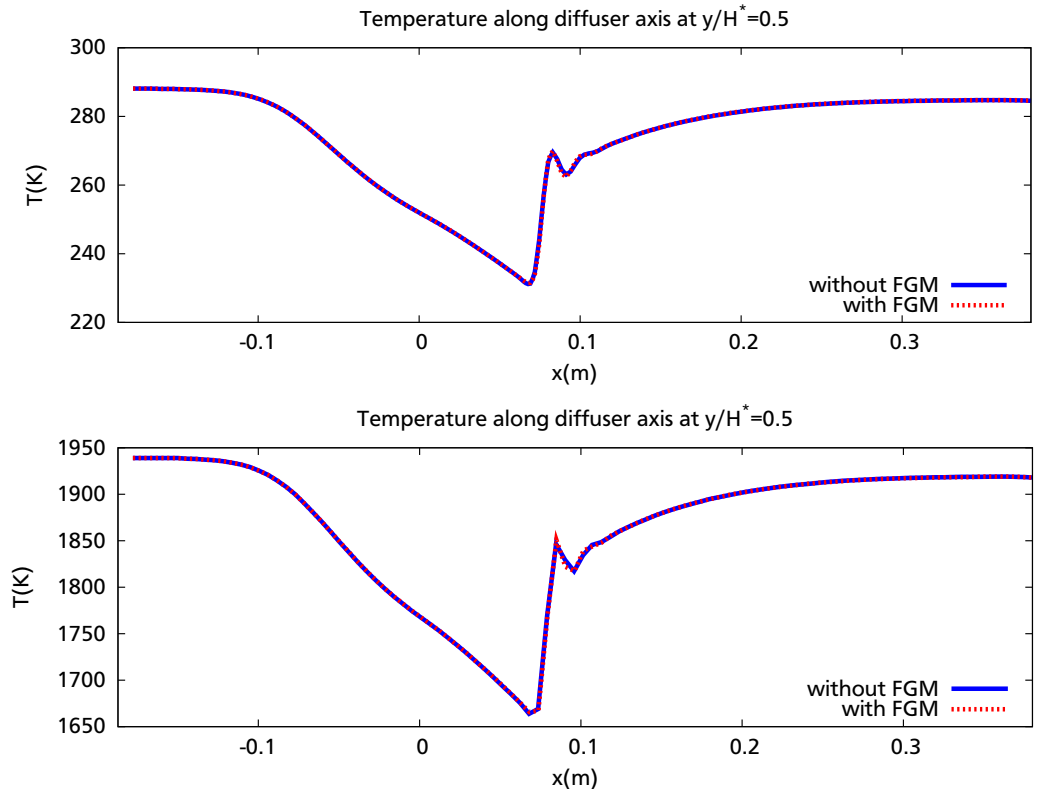

Figure 6.30.: Temperature profile along centerline of the diffuser, with and without using tabled chemical data, top: unburnt case, bottom: burnt case

6.4.3 Discussion of FGM/compressible SIMPLE coupling

The verification of the FGM/compressible SIMPLE coupling showed promising results. For the incompressible reactive flow the deviation between results obtained using the newly coupled algorithm and the standard incompressible FGM algorithm is less than one percent. The differences can be accounted to differences in inlet boundary conditions. The treatment of chemical reaction data for mixture fractions outside the flammability limits is a little different for both methods. This can lead to small deviations when using the two methods.

When calculating the premixed flamelets for the FGM table only one static pressure is given as boundary condition. The influence on the calculated flame temperature and the source terms of species was shown to be negligible in section 5.5. But a difference between local static pressure and preset static pressure for the FGM table generation will linearly affect the density calculation. For low mach number flows with low static pressure variation within the flow field this influence is small. When strong pressure differences are present within the calculated domain this influence will increase. Intrinsically the new code uses the correct static pressure as the density is always calculated at the end of each iteration.

Even though it was shown that the compressible code can also be used for incompressible flows it must be mentioned that the incompressible version is more suited for such applications. Given velocity profiles at the inlet are easier to handle than total pressure boundary conditions. Especially, if the total pressure is not known or given from experiments.

Within the compressible region the newly coupled code can be used in the same way as the standard compressible SIMPLE algorithm. Verification was only conducted for the two limit cases $\mathcal{Y} = 0$ and $\mathcal{Y} = 1$. The region in between could not be validated as appropriate experimental data was not available. Here, it is expected that the influence of compressibility on the flame has to be taken into account by additional measures, especially in shock regions and for high Mach number flows.

6.5 Application of New Cfd-solver on Complex Geometry

6.5.1 Nozzle Guide Vane

To demonstrate that the newly developed code PUC is also suitable to model complex industrial geometries, an engine blade geometry was modelled: A Rolls-Royce Deutschland first stage high-pressure turbine NGV. As no measurements for the hot flow are available, PUC was benchmarked against two codes, Fluent, ANSYS FLUENT 12.0.16., and a Rolls-Royce plc turbomachinery in-house code, Hydra, version 6.01.03 [70]. Fluent calculations were carried out with the pressure-based option, while Hydra is density-based. The calculations with Hydra were performed by Stavors Pyliouras for preparation of [64].

Solver Setup

To ensure comparability, steady computations at simulated cruise conditions were performed for all three codes on the same mesh. The computational grid was generated with the Rolls-Royce plc in-house tool, Padram [116]. A dimensionless wall distance y^+ of approximately 35 was applied due to the use of wall functions. The cell distributions near the leading and the trailing edge are shown in figure 6.31. The geometry model (figure 6.32) contains one passage of a stator row with periodic boundary conditions applied at the circumferential boundaries. No film cooling was modeled. Identical boundary conditions for PUC, Hydra and Fluent were prescribed. Mean total pressure and mean total temperature values with purely axial directed flow angles were applied at the inlet. The turbulence properties k and ϵ were set to model inflow with 5 % turbulence intensity. A radial static pressure profile was used as the outlet boundary condition.

Evaluation

To create circumferentially mass-averaged radial distribution functions, all solutions from each code were imported into the postprocessor Tecplot. The solution was interpolated onto ijk-ordered planes at certain positions which allowed the axial cutting planes to be imported into Matlab and circumferential mass-averaging to be carried out. This scripted routine assures comparability by processing each flow result in the same way.

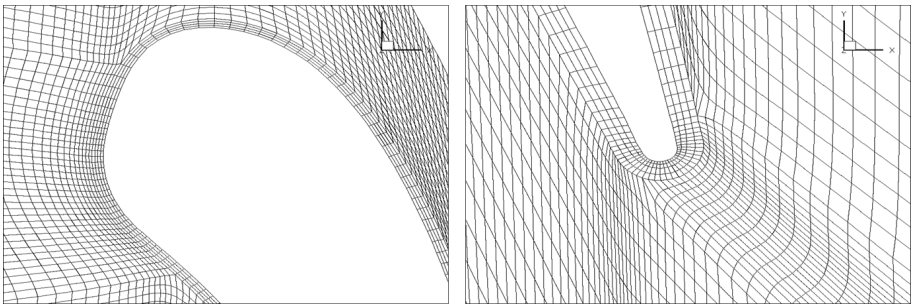

Figure 6.31.: NGV mesh near leading and trailing edge

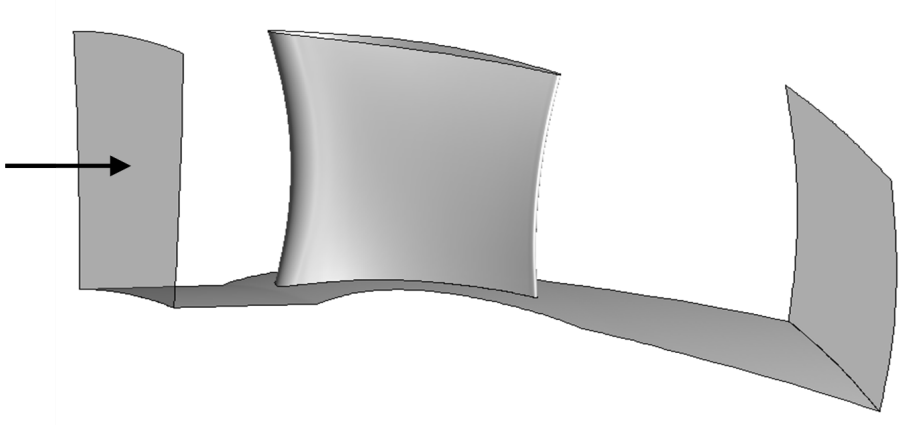

Figure 6.32.: NGV geometry

Results

Circumferentially mass-averaged results extracted at the inlet and outlet boundaries are displayed in figure 6.33 - 6.36. The results of all three codes qualitatively and quantitatively show very good agreement at both stations. It is of special interest that the flow variables coincide at the inlet. In an integrated simulation the outlet of the combustor is placed at this location. This is the place where any influence of the NGV would travel back into the combustor's domain. These flow variables are commonly varied to study the effects of non-uniformity in combustor outlet pressure and temperature profiles on the turbine's flow-field. Figure 6.33 demonstrates the comparability of all three codes as the Mach number curves match with a relative deviation of only 0.5 %. The agreement between PUC, Fluent and Hydra is very good at the outlet (figure 6.34 - 6.36). The influence of secondary flows is evident in all curves towards end walls. The Mach number deficit is evident in figure 6.34 in the hub area up to approximately 15 % span and from 80 % span to the casing. Hydra predicts a slightly larger impact of the secondary flows on the Mach number deficit at hub and casing. Analyzing the total pressure ratio at outlet (the local total pressure referenced to the maximum total pressure at outlet,

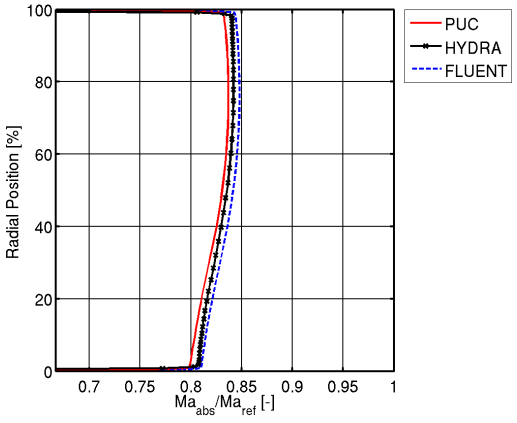

Figure 6.33.: Comparison of Mach number at inlet

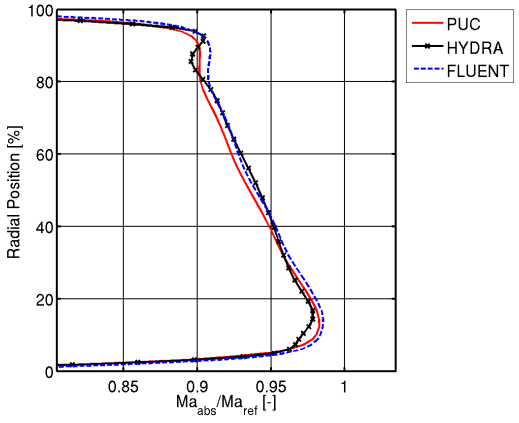

Figure 6.34.: Comparison of Mach number at outlet

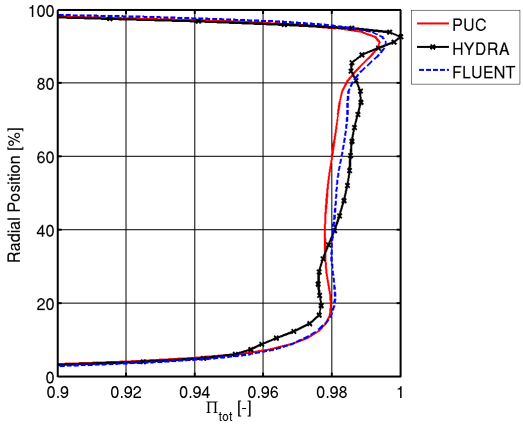

Figure 6.35.: Comparison of total pressure at outlet

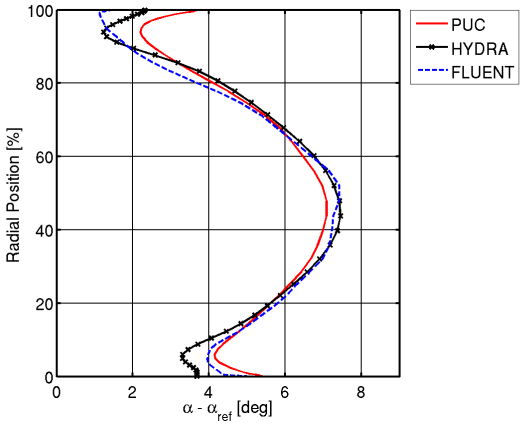

Figure 6.36.: Comparison of whirl angle at outlet

$\Pi = \frac{p_{tot,out}}{p_{tot,max,out}}$, figure 6.35), Hydra predicts even more pronounced secondary losses, with further propagation in span wise direction, up to 30 % span near the hub. All three codes predict different mid-span total pressure levels. PUC and Fluent, which use the same numerical methods, give similar results while the total pressure distribution predicted by Hydra is more inhomogeneous. The distortion of the whirl angle in figure 6.36 corroborates the trends observed previously. The contour plots of the total pressure loss $\zeta = \frac{p_{tot,in,mean} - p_{tot,out}}{p_{tot,in,mean}}$ at the outlet (in the plot referenced to the maximum ζ at outlet) are displayed in figure 6.37 for all three codes. It can be seen clearly that the PUC and Fluent predictions of total pressure loss are in very good agreement. Results obtained with Hydra indicate less mixing of areas with low and high total pressure loss. Additionally, the area of high total pressure loss propagates further towards mid span, which supports the conclusions drawn before based on the circumferentially averaged flow quantities.

PUC:

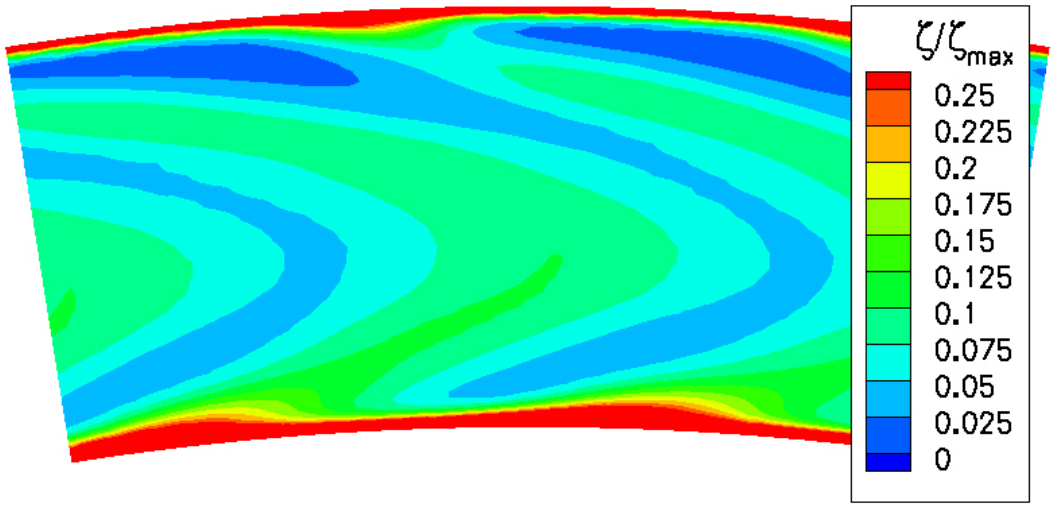

Fluent:

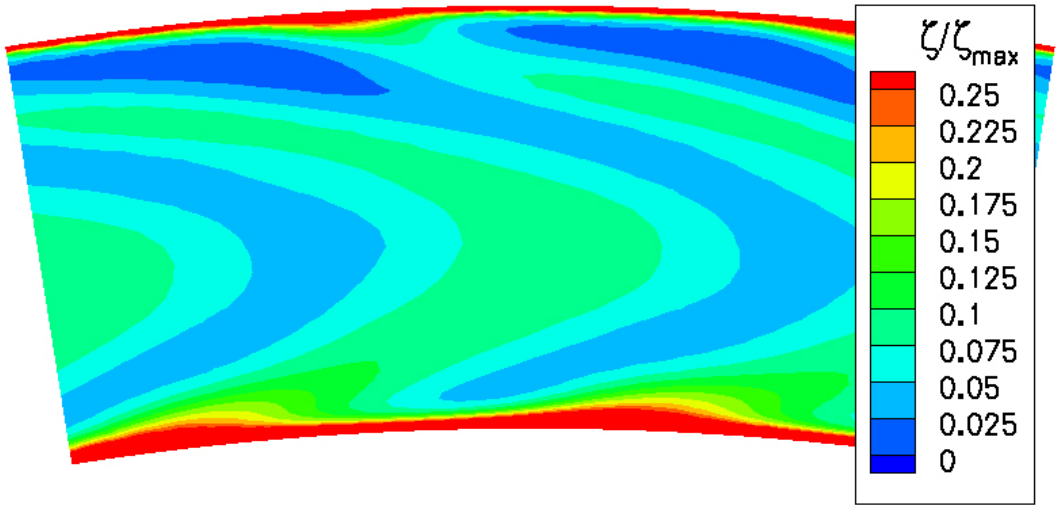

Hydra:

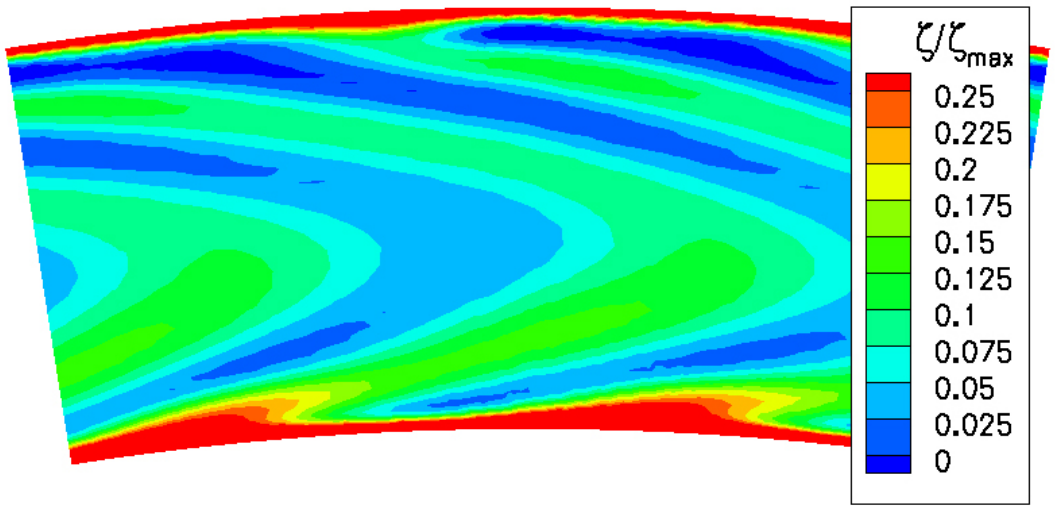

Figure 6.37.: Comparison of total pressure loss for PUC, FLUENT, and Hydra

6.5.2 Swirling Reacting Flow In Model GT Combustor

The present test case was performed to check, whether it is possible to calculate lifted flames with the developed FGM/compressible coupling. Lifted flames are present in gas turbine combustors. In contrast to piloted flames like the Flame D, the reaction is stabilized by a recirculation zone within the flow. It is induced by a high swirl flow. Due to the swirl, and due to the flow expansion into the combustor, a recirculation develops, that circulates the flow back up-stream so that a stagnation region is formed. Within this region the velocity of the flow balances the flame velocity. For premixed combustion this stabilizing mechanism must be utilized, as the typical flow velocities are higher than the flame speed of the used fuels. Until today, most aviation combustors feed the fuel into the combustion chamber as a liquid. It is blasted by special atomizers[1] into the combustion chamber and vaporizes in there. Thus, no flammable mixture exists upstream, which could auto-ignite or be dangerous if a flashback occurs.

The described phenomena (complex flow structure stabilization of the flame, spray vaporization) are of high interest to combustion chamber developers. Only, if the processes and their interaction effects are understood the reaction process can be improved to control burn-out and emissions and of course flame stability. To study those effects, a model gas turbine (GT) combustor was developed by Janus in 2005 [55] at the Institute of Energy- and Power Plant Technology at the TU Darmstadt. It provides optical access to the flame in order to allow for the use of non-intrusive laser-optical measurement techniques. With those it is possible to characterize the flow, spray and flame behavior. The setup of the chamber is given in figure 6.38.

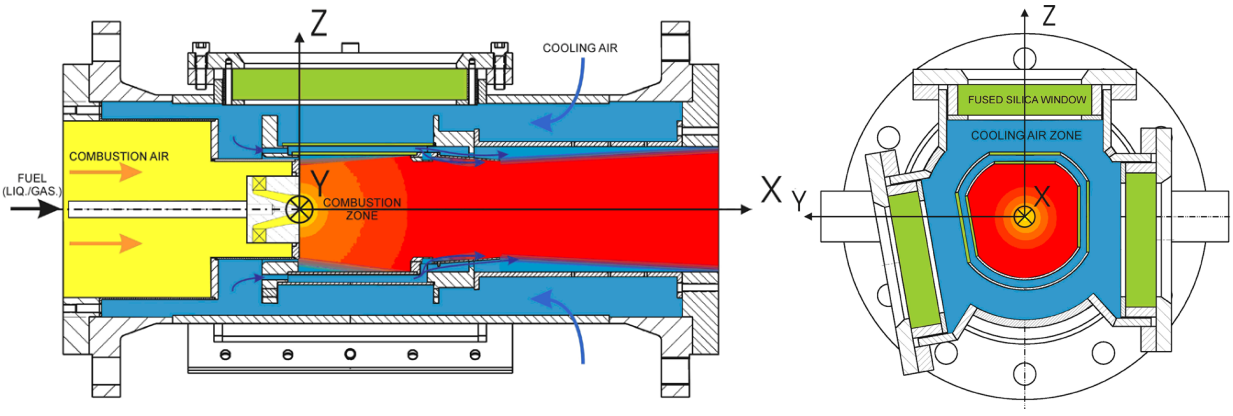

Figure 6.38.: Setup of generic gas turbine combustor, [55]

The experiments that are referred to in this thesis are the non-reacting and reacting flow cases at 2 bar published in Janus et al. [56]. The model GT combustor can be equipped

[1] different technologies exist, an overview can be found in [75]

with different kinds of nozzles to study different kinds of fuel supply techniques. In this investigation a single swirl nozzle was used that feeds pure methane into the combustion chamber, surrounded by a swirling air stream. The nozzle is shown as part of the numerical grid in figure 6.39. The combustion air and the methane are mixed by the swirl. Due to the recirculation mechanism outlined above a region of flammable mixture forms that can be ignited. A stable burning mode was adjusted, by adjusting the swirl and main-jet velocity. The velocity field was measured using Laser Doppler Anemometry.

Numerical Setup and Remarks on Solution Strategy

Numerical Setup

The numerical grid consists of 389,636 cells. It is shown in figure 6.39. The smallest cells at the exit of the main-jet have an edge-length of approximately 0.84 mm in axial direction and 0.21 mm in radial direction. The upper edge of the nozzle is resolved using two cells in radial direction. The cells within the swirl generator have an edge-length of approximately 1 mm. This resolution was maintained until the end of the front part of the combustor. The rear part of the combustor is resolved with cells of 1-5 mm in edge-length. At the wall boundaries the cells were spaced, so that the *law of the wall* could be used.

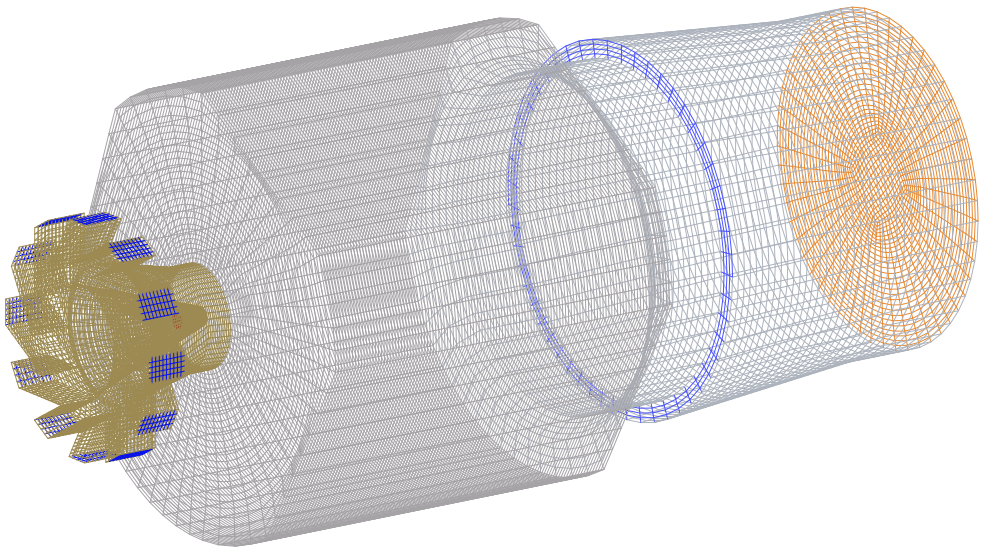

Figure 6.39.: Numerical grid of model GT combustor; grey: combustor wall, beige: nozzle, blue: air inlet, orange: outlet

From the experiments the mass-flow rate, the velocity conditions and the pressure inside the chamber are known. The total boundary conditions had to be adjusted following

the procedure given in section 4.4, so that the given mass flow rate was met as well as possible. The main-jet pipe in the center of the nozzle was simulated with a shortened length of three diameters. This length is too short for a turbulent velocity profile to self-adjust. Therefore, at the inlet the total pressure was prescribed using the 1/7-power law for the velocity profile characteristic of a turbulent pipe-flow. The final settings are given in table 6.7. At the swirler inflets the flow angles were aligned with the direction of the vanes of the swirler. The static pressure at the outlet was prescribed by a constant pressure field, knowing that this was most probably not the case in the experiments. The FGM table was calculated using the GRI 3.0 mechanism. The overall ratio of air to fuel mass-flow is given from experiments by the equivalence ratio of $\phi = 0.8$. Turbulence was modeled using the k–ϵ model. The convective terms were discretized by using 50 % CDS blending.

	Experimental data			reactive	non-reactive
	$\dot{m}$	T	T_{tot}	p_{tot}	p_{tot}
Swirler Inlet	0.03 kg/s	623 K	625 K	205080 Pa	204600 Pa
Fuel Inlet	0.01392 kg/s	368 K	372.6 K	208700 Pa	207920 Pa
Cooling Air Inlet	≈0.03 kg/s	623 K	623.61 K	201660 Pa	201700 Pa
Exit (p_{stat})				201480 Pa	201560 Pa

Table 6.7.: Boundary conditions of model GT combustor

Solution Strategy

Two calculations were performed, one non-reacting and one reacting flow case. In both calculations the coupled algorithm was used. For the reacting calculation the flow was numerically ignited by setting the progress variable to 1 inside a “spark” region with the center at (x,y,z)=(20,0,0) and a radius of 20 mm for 10 iterations. After that the flame stabilized inside the domain without further numerical support. The total boundary conditions were adjusted to match the given mass-flow rate from the experiments as given in table 6.7. The cooling flow is not exactly known from experiments, as some of the cooling flow is passing outside the exit duct of the model combustor and some is used for cooling inside. The exact split is not given in the reference.

Discussion of Results

Calculated and experimental data of axial, radial and tangential velocity profiles are given in figure 6.40 for the non-reacting and in figure 6.41 for the reacting case. The

dots and the triangles represent the experimental data and the red and blue lines the results of the reacting and non-reacting numerical simulation, respectively.

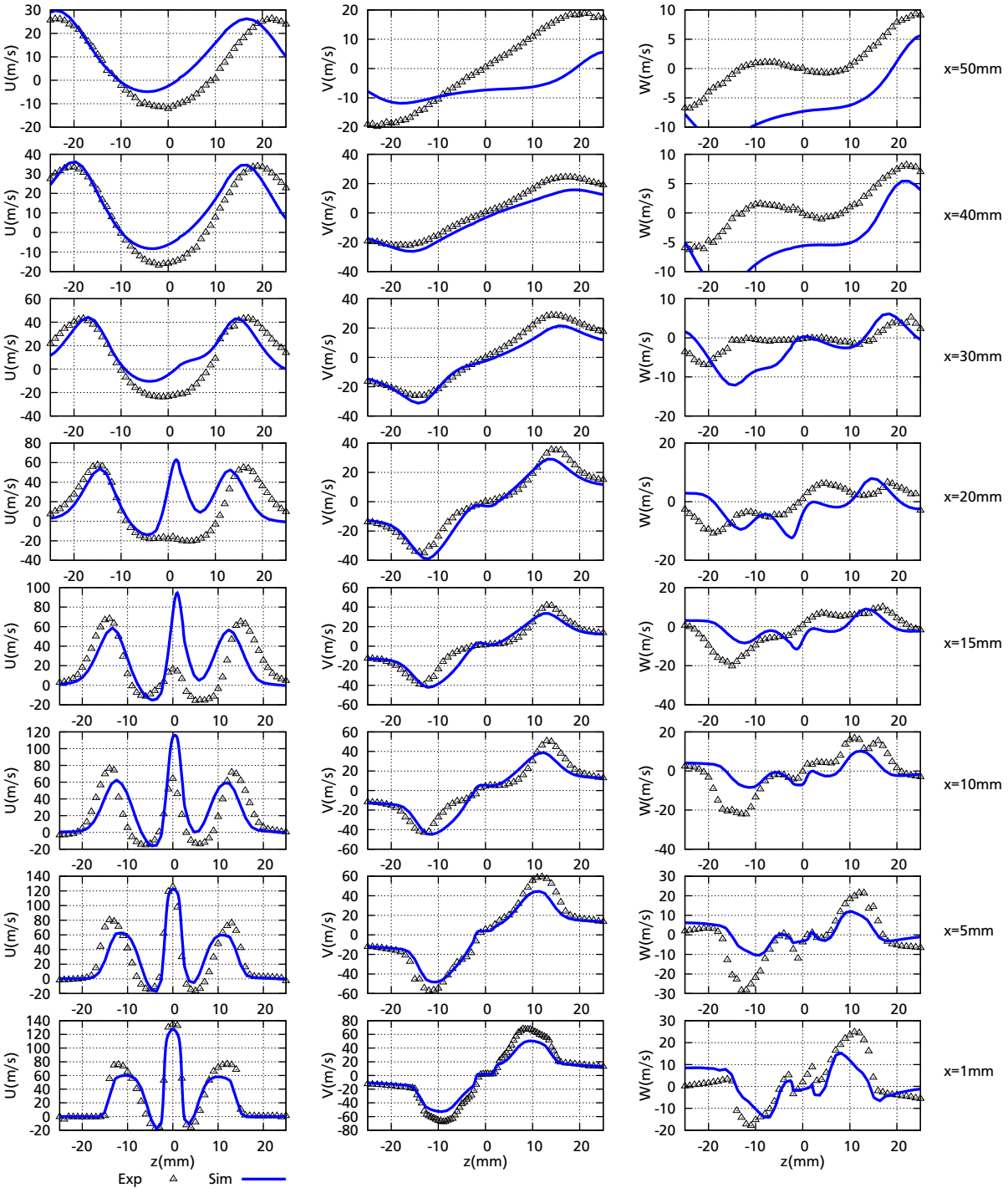

Figure 6.40.: Axial (left), tangential (middle) and radial (right) velocity profiles for model GT combustor, non-reacting flow

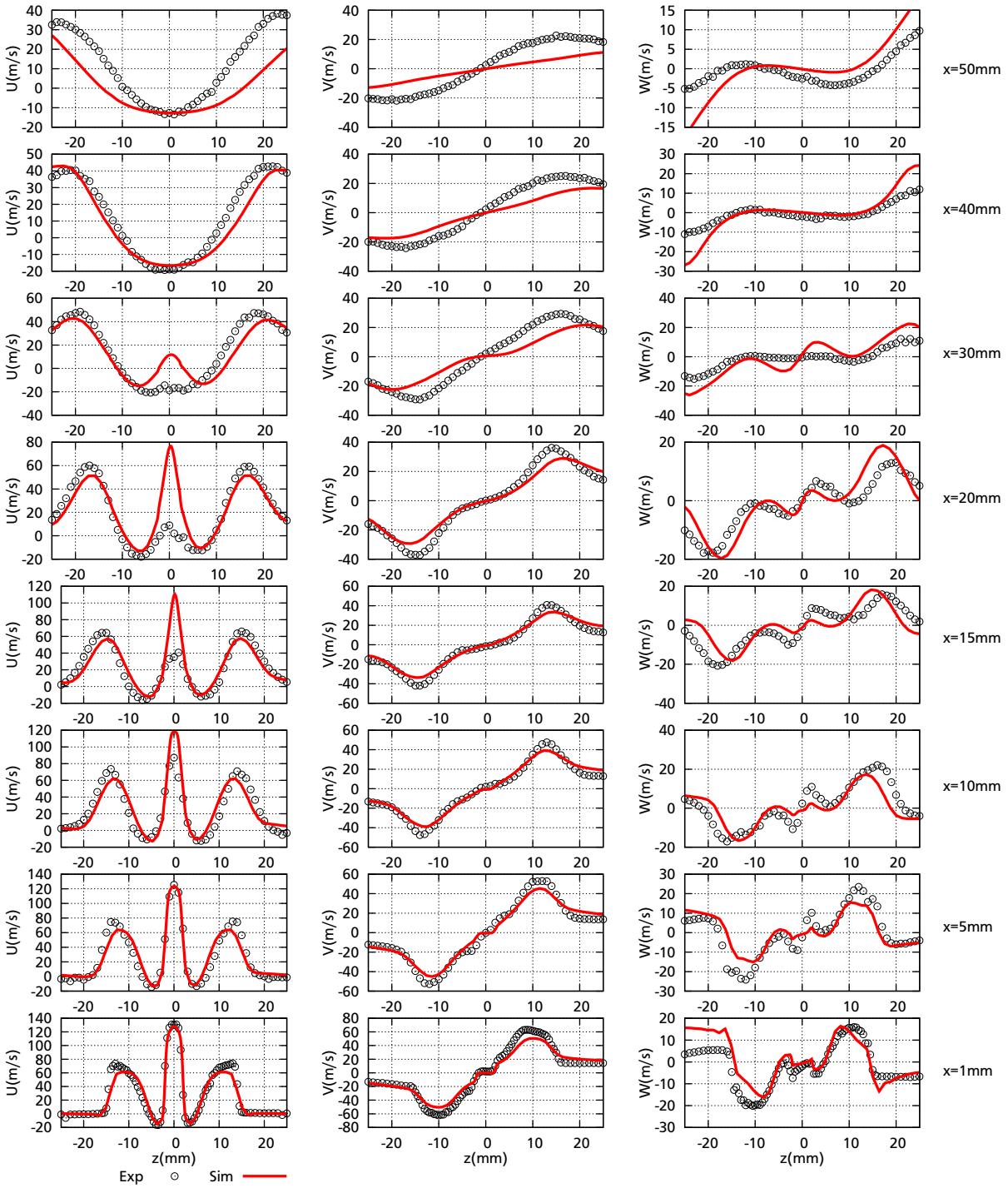

Figure 6.41.: Axial (left), tangential (middle) and radial (right) velocity profiles for model GT combustor

Non-reacting Flow

The general features of the flow are captured. The axial velocity profiles (figure 6.40, left column) show that the spreading of the outer swirl is under-predicted at the height of x=5 and 10 mm. The penetration length of the main jet is highly over-predicted for

x=10, 15, and 20 mm. It is obvious that the used turbulence model is not well-suited to calculate this flow. In the planes for x≥15 mm a pronounced asymmetry of the calculated axial velocity profiles can be observed. This asymmetry is less pronounced in the experimental data. The asymmetry in the calculations increases with increasing distance to the nozzle's exit. The deviations to the experimental data are due to the asymmetry more prominent on the positive z-axis. During the adjustment of the boundary conditions it was observed that the extend of this asymmetry was influenced by the cooling air mass flow rate injected in the rear part of the combustor. The more cooling air was injected into the combustor, the more pronounced the asymmetry becomes. A similar influence was reported by Hahn [44]. He observed, that the mass of injected cooling flow and the geometry of the exhaust gas duct influenced the recirculation zone and the penetration length of the main jet. The calculated circumferential velocity profiles match the experimental data quite well, except in the height of x=50mm. The radial velocity profiles only poorly conform to the experimental data.

Reacting Flow

An impression of the reactive flow is given in figure 6.42. The underlying color-map shows the temperature present in the combustor. The overlying iso-contours quantify the production rate of CO_2. They can be used to locate the reaction zone.

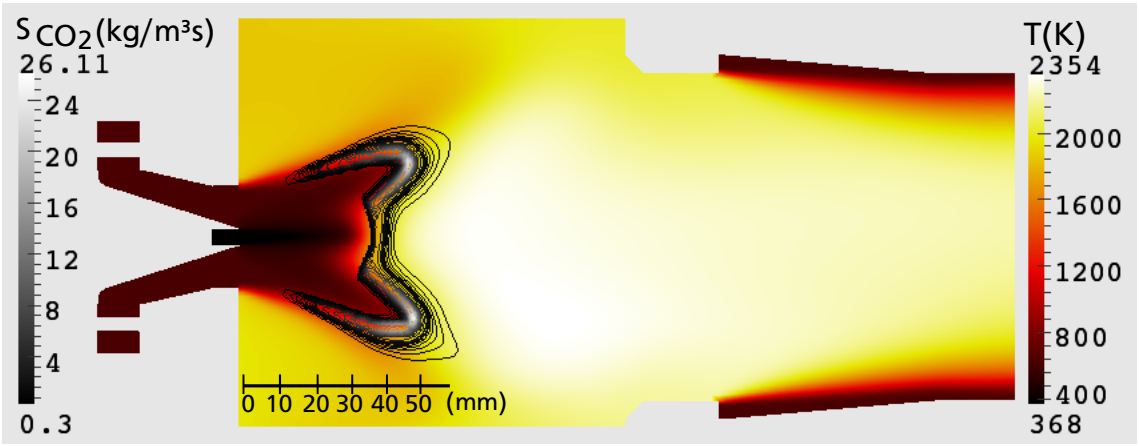

Figure 6.42.: Temperature distribution and iso-contours of source term of CO_2 of model GT combustor, y-axis-normal plane

In the inner region of the main jet the flame is stabilized at a height of around 30 mm, which is about 10 mm higher than reported from experiments. This can be addressed to the over-estimation of the main-jet penetration into the combustor. In the outer region of the swirl the flame reaches upstream towards a height of 10 mm.

The axial and tangential velocities of the swirl are represented quite accurately up to the height of 20 mm (Figure 6.41). This is the region were the flame stabilizes. The asymmetry observed for the non-reactive calculation is less pronounced in the reactive calculation. Here, the influence from the recirculation zone in the rear part of the combustor is attenuated. The axial velocity of the main jet is highly over-predicted, especially at the heights of 10, 15 and 20 mm. This can be attributed to the underestimation of turbulence of this area. The k-ϵ model is obviously not able to predict the deceleration of the jet.

Comparison of Reacting and Non-reacting Flow

The influence of the combustion model is investigated by comparing the two cases with each other. Two main changes to the flow field due to the reaction can be observed in the experiments: The penetration depths of the main jet increases for the reactive flow by approximately 5-10 mm, which can be deduced from the measurements taken at 15 mm, 20 mm and 30 mm height (figure 6.40 and 6.41) In Figure 6.43 the velocity profiles of both cases, for simulation and experiments, respectively, are given. The velocity of the main jet is increased in these heights by approximately 20 m/s according to the measurements. The same difference can be observed for the calculation.
The reaction causes an increased spreading rate of the outer swirl in the experiments. This trend is also observable in the calculations. The quantitative extend of this shift is the same for both experiment and calculation. This is especially visible for the values for x=20 mm on the negative z-axis (Figure 6.43, right side), but also for the x=15 mm measuring plane. On the positive z-axis this trend was smaller in the experiments, but it is larger for the simulations. The reason for this difference is the strong asymmetry in the non-reactive calculation at these heights.

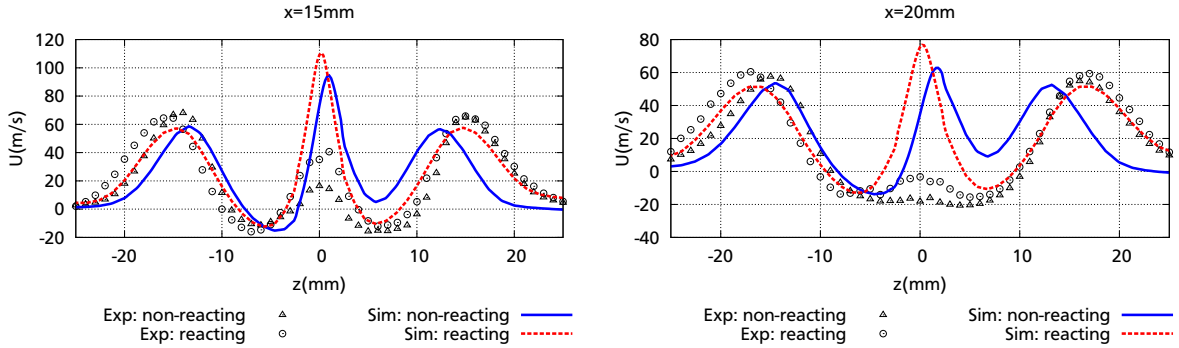

Figure 6.43.: Comparison of reactive and non-reactive calculation with experiments

7 Integrated Simulation of Combustor-Turbine Interaction

The final test case is an integrated simulation of the reactive, compressible flow in the combined domain of combustor and NGV. The geometry is a BR710 combustor including BR715 NGV's from Rolls-Royce Deutschland. The combustor is an RQL combustor with twice the number of NGV's as injectors. Only a sector of the annulus was simulated. The setup of the integrated domains is shown in figure 7.1.

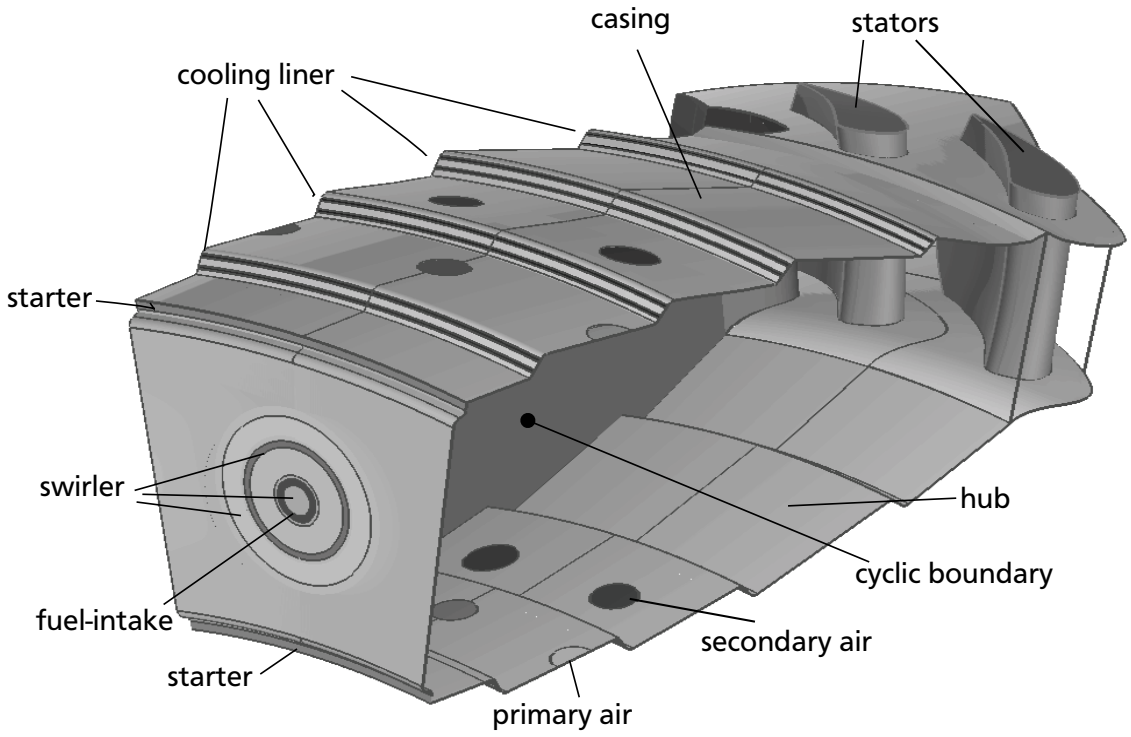

Figure 7.1.: Setup of integrated simulation, distorted view, the cyclic boundary plane at the front is left out to allow the view inside of the chamber

Grid Setup

The numerical domain consists of 1,876,821 cells. Approximately 1.05 mio cells were located inside the combustor domain and approximately 800,000 cells were used for meshing the NGV passages. The number of cells was kept small by using the wall-function to bridge the viscous sub-layer and buffer-layer of the turbulent boundary layer.

A $y^+ \approx 35$ was established. Figure 7.2 shows the front view on the numerical inlet representing the swirler flow (red, pink and light green). Figure 7.3 shows a view on the hub-mesh of the integrated domain.

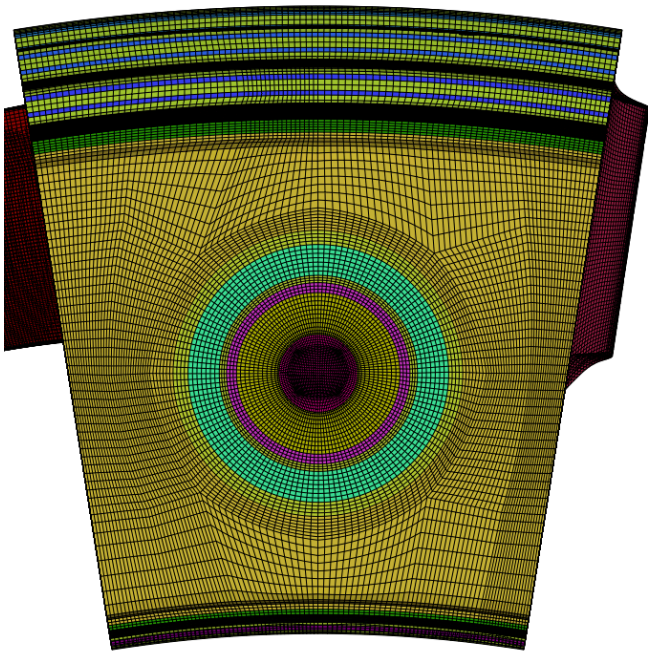

Figure 7.2.: Front view of integrated domain, inlet of swirler - red, pink and light green

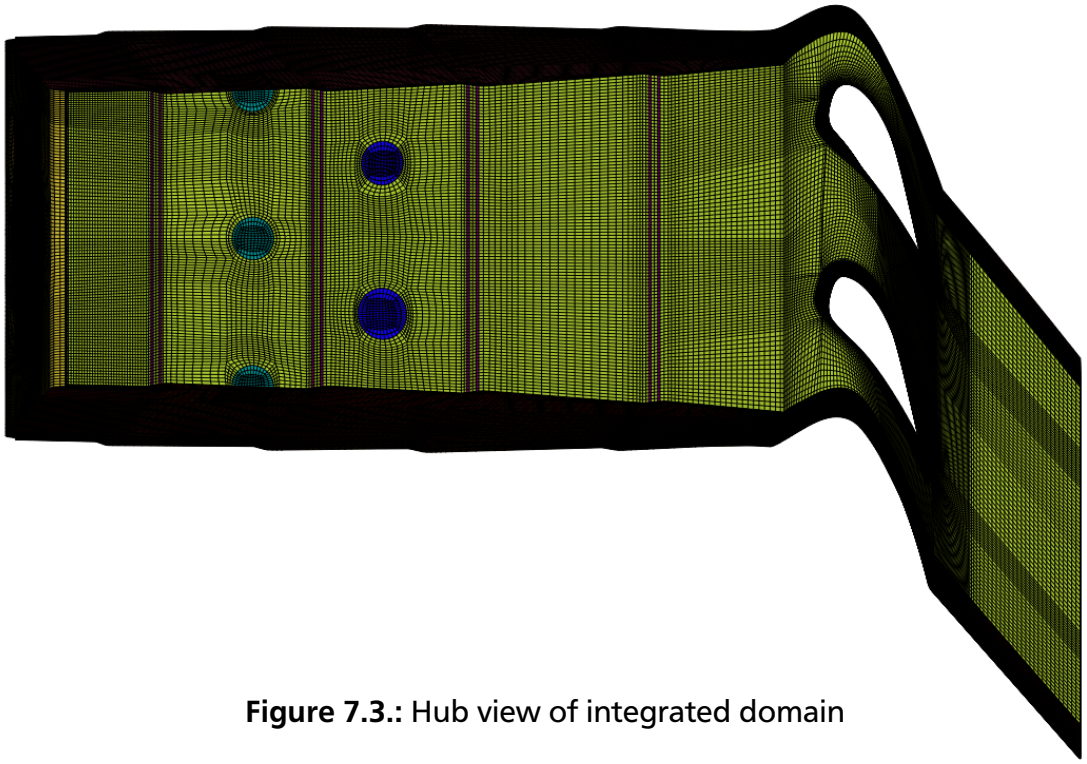

Figure 7.3.: Hub view of integrated domain

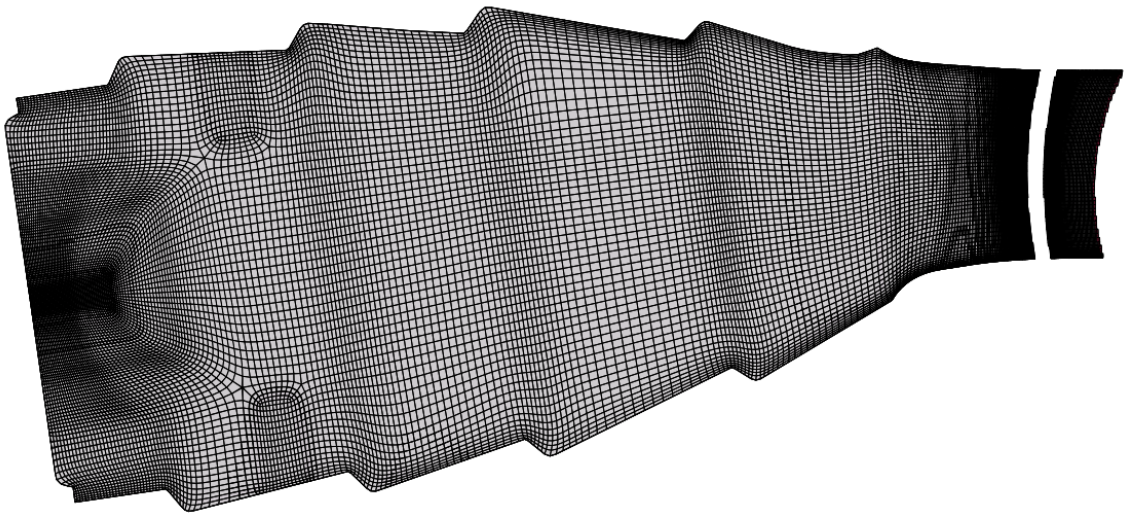

Figure 7.4.: Radial cut of mesh of integrated simulation

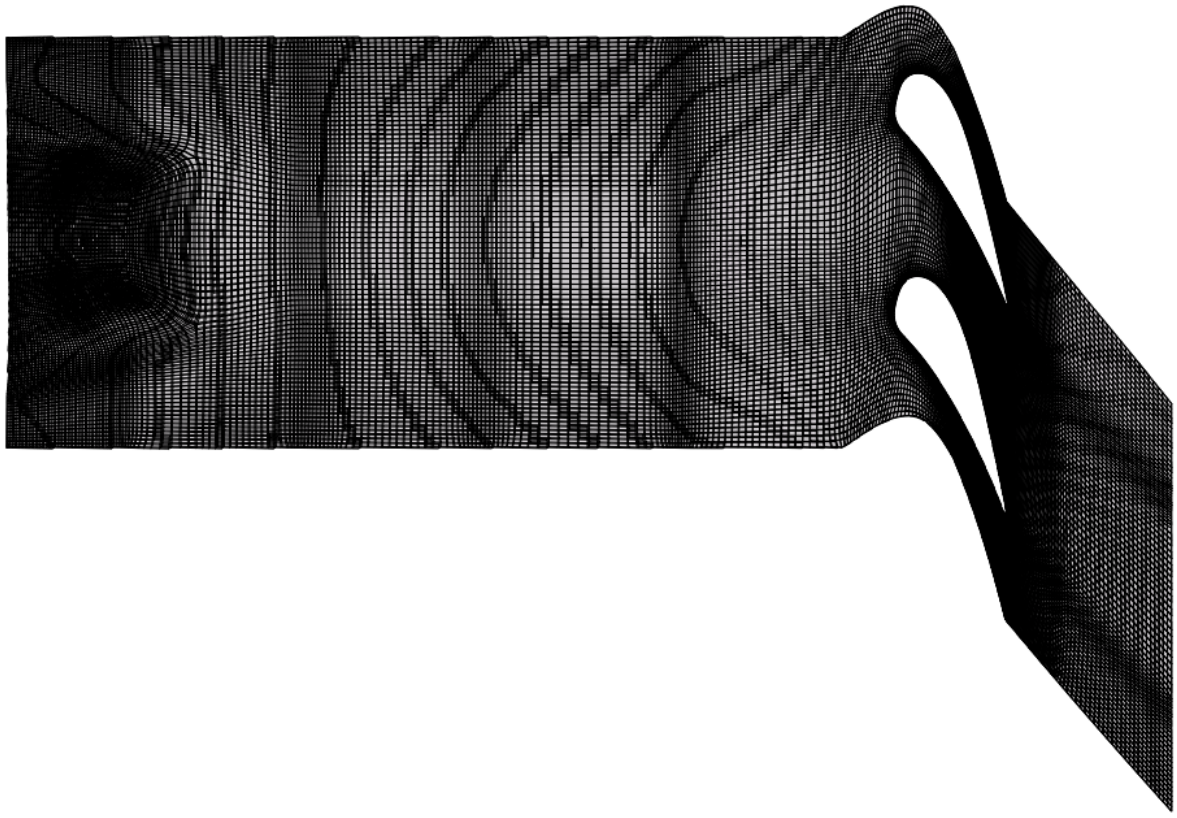

Figure 7.5.: Circumferential cut of mesh of integrated simulation

Figure 7.4 shows the mesh within the combustor using a radial cut through the center position of the swirler. Figure 7.5 shows the mesh in a circumferential cut. Here the NGV passages are visible.

7.1 Solver Setup and Solution Strategy

The geometry as well as the boundary conditions used for the simulation were provided by Rolls-Royce Deutschland. It is a simulated take-off condition for which experimental measurements of the RTDF at the combustor outlet exist, obtained from a full annular high pressure test at the DLR-Cologne facilities. The boundary conditions for the starter, the liners and the swirler were given by means of velocity profiles. The total pressure conditions were subsequently adjusted. The resulting velocities however did not exactly match those used by RRD for their own simulations of the same combustor, due to the difficulties in inlet boundary condition adjustment, explained in section 4.4. Furthermore, some simplifications were made, when setting up the test case. In the standard incompressible simulations effusion walls are used to model the liner air intakes. Effusion walls were not implemented into PUC, thus inflow boundaries were used instead while keeping the inflowing amount of air as close as possible to the reference conditions. At the outlet behind the NGV a radial pressure profile was applied. Overall the same AFR at the combustor exit was established.

Kerosene Modelling

In the real engine a kerosene spray is injected into the combustor with an air-blast atomizer. The incompressible version of PRECISE-UNS offers the possibility to use a spray model. This spray model would add another complexity to the integrated simulation and was thus omitted within this thesis. Instead, the kerosene was injected fully evaporized, mixed with air at the position were the spray cone would be injected. For the calculation of the FGM tables the kerosene mechanism was used. The mixture temperature of the reference state FGM table was set 200 K less than for the standard table, according to section 5.1.

Initializing the Flow Field

To obtain a converged solution several measures have to be taken for such a complex simulation. The initial flow field needs some special attention. The inlet velocities depend on the ratio of total pressure and local static pressure. The local static pressure depends on the given static pressure at the outlet. These differ by a factor of approximately 1.5, caused by the static pressure drop within the NGV. If the whole field was initialized with the pressure at the exit boundary (which is the default setting), the inlet velocities would be far too high at the beginning of the iteration process and the code would diverge. Therefore, the static pressure was set to an estimated pressure inside the combustor while for the NGV domain a decreasing pressure distribution was initialized

from the front of the NGV until the exit. Accordingly, the velocity field was initialized with increasing velocities towards the outlet. For non-reactive simulations this initialization is sufficient. For reactive flow the mixture and temperature conditions need to be adjusted as well. For the simulation of the model GT combustor it was possible to ignite the flow, after the stabilizing swirl had adjusted. For the integrated simulation, the flame must already be burning at the beginning of the simulation, otherwise the temperatures within the NGV would be far too low and thus the density too high, to establish the desired mass flow. Hence, the field was initialized with the mixture fraction according to the target exit AFR and the progress variable was set to unity in the core of the combustor domain and throughout the NGV passages.

Solution Strategy

Within the initial phase of a simulation the velocity field becomes more in-homogeneous than the final converged flow field. Especially, when higher order discretization schemes are used the iteration process can produce fluctuating values, exhibiting unrealistic velocity peaks in areas of high shear. The resulting overestimated velocity gradients cause strong, over-predicted turbulent kinetic energy at the beginning of the iterative solution process. Generally relaxation factors are used to damp these influences. In the compressible algorithm the turbulent kinetic energy couples back to the total enthalpy equation and to the static pressure field. If these disturbances are too high, especially at the outlet of the numerical domain, where the static pressure is preset as boundary condition, this may lead to divergence. Hence, the velocity and pressure field were calculated first with the turbulence model switched off. Slip wall conditions needed to be applied at the walls. Additionally, the laminar viscosity was raised by two orders of magnitude to introduce some damping. With these settings it was possible to establish a sufficiently smooth velocity and pressure field, which could be used as initial solution for the actual calculation.

7.2 Separation of Reaction Zone and Compressible Flow Region

In figure 7.6 the source term of CO_2 is shown. All cells, in which the value of the source term is lower than the threshold value (1 in left plot, 4 in right plot), are not shown in the figures. Most of the reaction has finished when the flow enters the NGV, but some burn-out is still present near the hub and casing of the NGV. The left plot of figure 7.7 illustrates, that the cooling flow entering at the last cooling liner is the reason for these un-burnt areas. In the same figure on the right side the temperature

difference ΔT due to compressibility effects is shown for the same area. In the regions were the reaction progress variable is between 0.8 and 0.9 there is no influence due to compressibility. Further downstream a temperature drop of up to 50 K is present in the area, in which the reaction variable is between 0.9 and 1. Proceeding reaction in regions of compressibility effects is not in agreement with the assumption that the flow entering the NGV is fully burnt. In chapter 5 is was outlined, that this assumption is important for the coupling approach that was used for the PPDF-FGM chemistry model. For this near wall flow this assumption is not satisfied for this calculation and consequently the reaction progress is overestimated within the NGV. The quantitative error is difficult to estimate. In this region the mixture fraction is in the region of the lean flammability limit. Quenching effects might occur. They are not accounted for in the PPDF-FGM table.

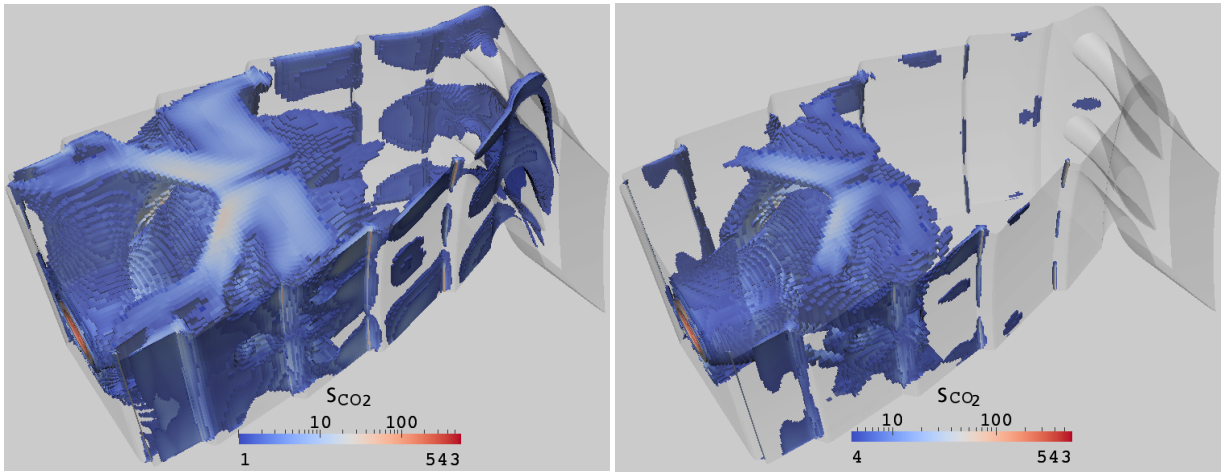

Figure 7.6.: Source term of CO_2 (g/cm^{3}s), using a lower threshold of 1 (left) and 4 (right)

7.3 Influence of NGV on Combustor Flow Field

A second calculation was performed, to identify the influence of including the NGV into the computational domain on the combustor-turbine interface. The NGVs were removed from the computational domain, so that an open annulus remained behind the combustor. A constant pressure field was prescribed as boundary condition at the outlet, which was adjusted to obtain the same mass flow as was present in the simulation with NGV. All other conditions (e.g. all total pressures at inlets) were kept the same. Finally, the overall mass flow rate for the case without NGV ('w/o') was 0.6 % less than for the case with NGV ('w'). It was observed, that the difference in mass flow in general splits over all inlets. But the balance between the inlets was different for the two calculations. The mass-flow rate of the fourth liner was disproportionately higher in the case 'w' compared to the other inlets. As the mass-flows of the two calculations could not be

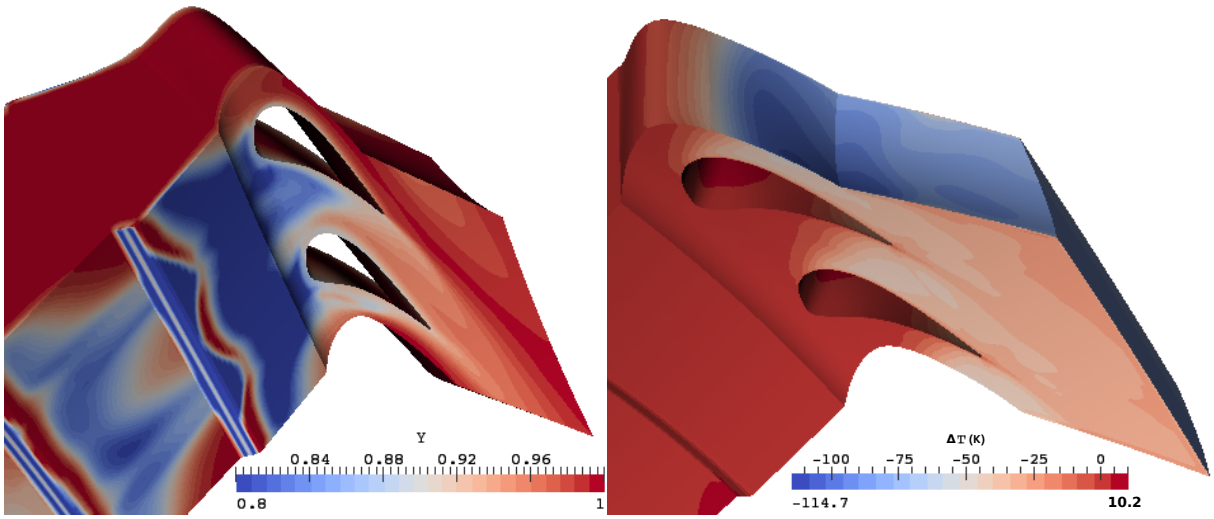

Figure 7.7.: Progress variable and temperature difference due to compressibility in the rear part of integrated simulation; note that the lower limit of the progress variable is 0.8 in the figure.

matched exactly it can not be assured, that this influence would vanish if they were. But as this difference is exceptionally high (7 %), it is believed, that at least some of the difference remains for calculations with 100 % matched overall mass-flow rates. The balancing of mass flow rates of the combustor seems to be influenced by its outlet boundary condition. For the two simulations presented here, the overall air mass flow was 0.58 % smaller for case 'w/o' while the fuel mass flow rate was 0.69 % larger. This summed up to a percentage discrepancy in total AFR of 1.28 % (all percentages are referenced to the value of case 'w/o').
It is favorable to use as high discretization orders as possible for all variables. While performing several calculations with increasing order of discretization, it was observed that the 'w' case is less sensitive to oscillations due to the mixture fraction discretization. While for the 'w' case LUDS could be used for discretizing the mixture fraction equation, the case 'w/o' would diverge for this setting. Thus, the comparison presented here was calculated with 50 % CDS for the mixture fraction for both calculations. For the momentum equations LUDS was used.

7.3.1 General Comparison

The averaged temperature difference was consistently between 8 to 10 K at all investigated radial cuts for the two simulations. That can be addressed to the deviation in overall AFR. All data are non-dimensionalized using the according average values in the following sections. Figure 7.8 shows the distribution of the velocity magnitude at a circumferential cut for both calculations. In the plots the two black lines denote the radial

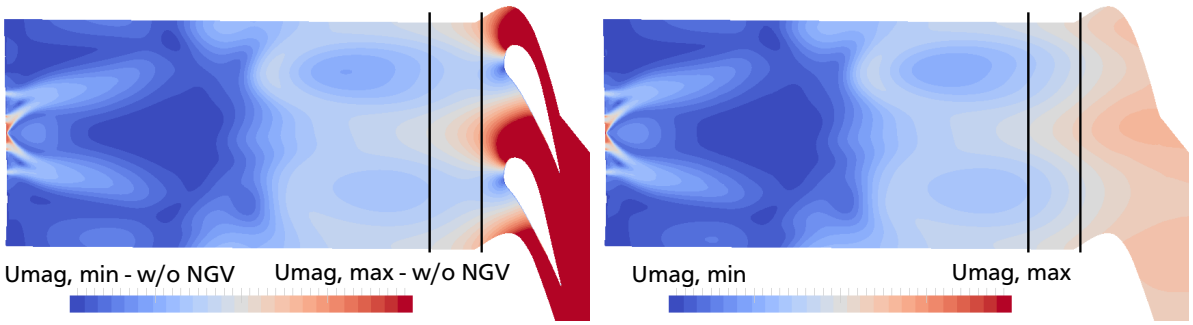

Figure 7.8.: Distribution of velocity magnitude, circumferential cut; blue: low velocity, red: high velocity; scaled from lowest to highest velocity of calculation without NGV (right side) for both plots; black lines: location of radial cuts at a distance of 100 % axial chord length (acl) and 25 % acl to leading edge of NGV

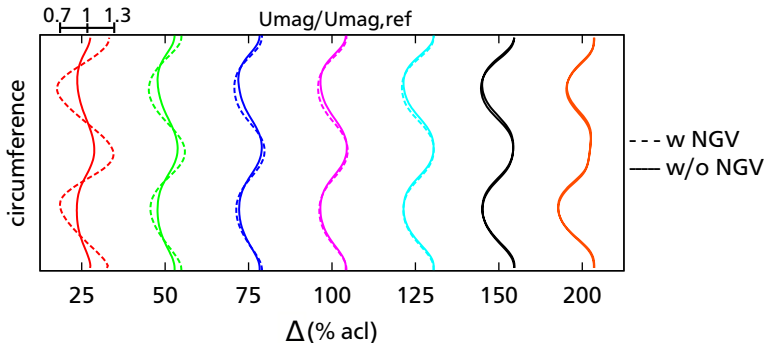

Figure 7.9.: Velocity profiles (velocity magnitude, U_{mag}) at different distances to the leading edge

planes at which the distribution of total pressure and temperature are to be discussed. They are placed in a distance of 100 and 25 % of axial chord length (acl) of the stators in front of the leading edge. The velocity distribution in the front part of the combustor is comparable. There are some small deviations present in the two calculations but it could not be assured that they were induced by the NGV. Deviations in the rear part of the combustor can clearly be addressed to the influence of the NGV. In figure 7.9 the profiles of non-dimensionalized velocity magnitude (U_{mag}) distribution in circumferential direction at different upstream distances to the leading edge, are shown. The distance to the leading edge is measured in % of acl. The profiles were taken at a radial position approximately midway between hub and casing. At a distance Δ of 200 % acl no distinct deviation is present. With decreasing distance to the NGV the difference becomes more pronounced. For a distance Δ of 25 % acl a significant difference of 25% in velocity magnitude is present.

7.3.2 Influence on Total Pressure and Velocity at Combustor Exit

The total pressure fields for the two planes under investigation are shown in figure 7.10.

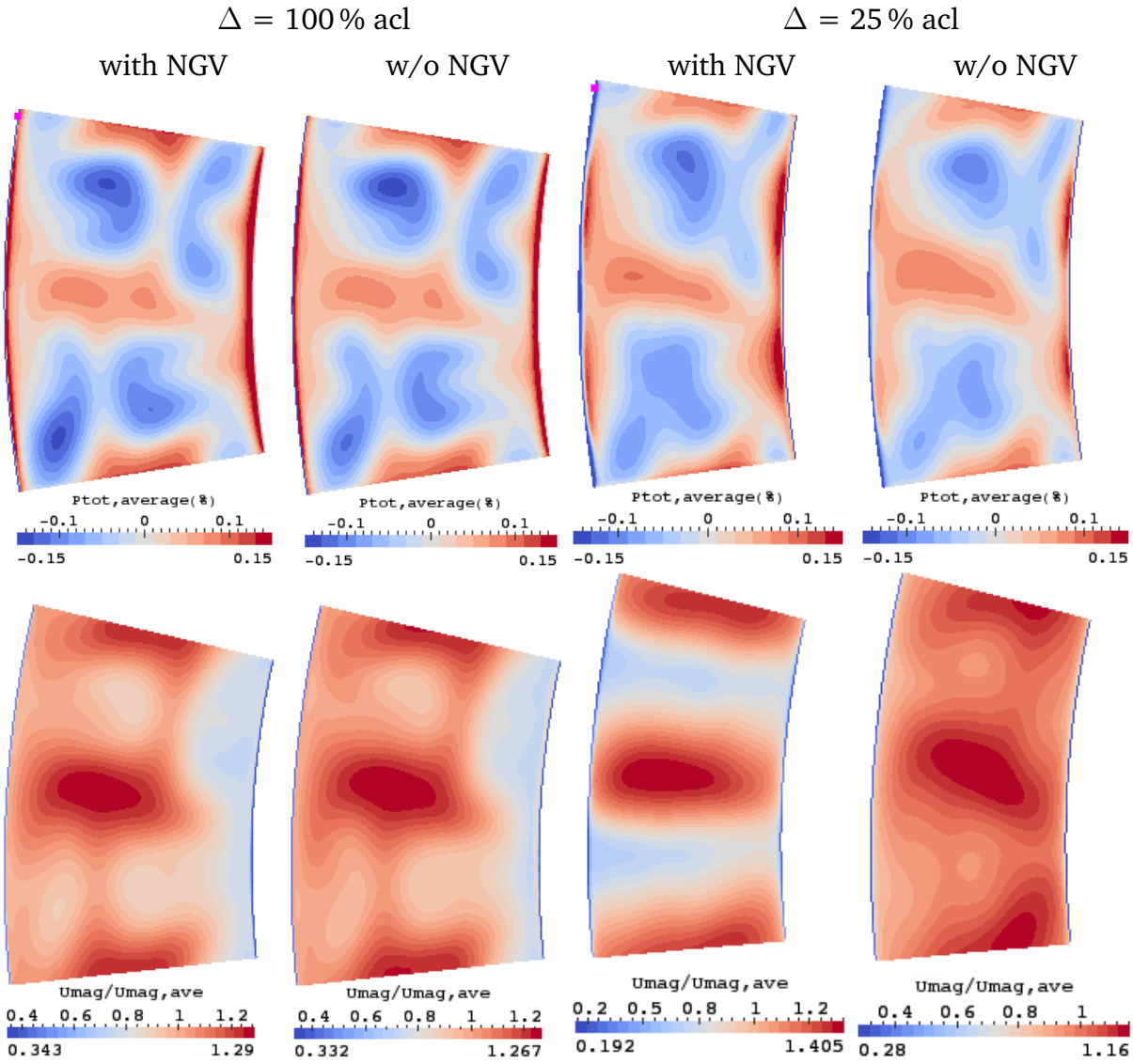

Figure 7.10.: Top: Total pressure distribution $((p_{tot} - p_{tot,average})/p_{tot,average} \cdot 100)$ - colormap not covering the whole range; bottom: Velocity distribution $(U_{mag}/U_{mag,average})$ for calculation with and without NGV for two distances Δ in front of the leading edge; acl - axial chord length

In the distance of one axial chord length the pattern is very similar for both cases 'w' and 'w/o'. The total pressure is higher in the regions of high velocity. The extension of these spots is a little larger for the calculation with the NGV for the plane very close to the NGV ($\Delta = 25\,\%$ acl). Here the influence of the NGVs is visible. The oval area of high velocity (figure 7.10, bottom left) is shaped by the shear forces induced by the secondary air jets. Close to the NGV (figure 7.10, bottom right) the influence of the

NGV on the flow is evident. The areas of high and low velocities are mixed out in the case 'w/o' while the pressure field of the NGV intensifies the amplitude. This influence was also noticeable in figure 7.9, in which one dimensional profiles were shown only.

7.3.3 Influence on Temperature Profile at Combustor Exit

Three different aspects were investigated for identifying the influence on the temperature distribution: the two-dimensional temperature distribution, the OTDF and the RTDF. The influences were investigated at different distances to the leading edge of the NGV.

Temperature Contours

The temperature contours at $\Delta = 100\,\%$ acl and $\Delta = 25\,\%$ acl distance to leading edge are shown in figure 7.11.[1] The averaged peak temperature between the two calculations

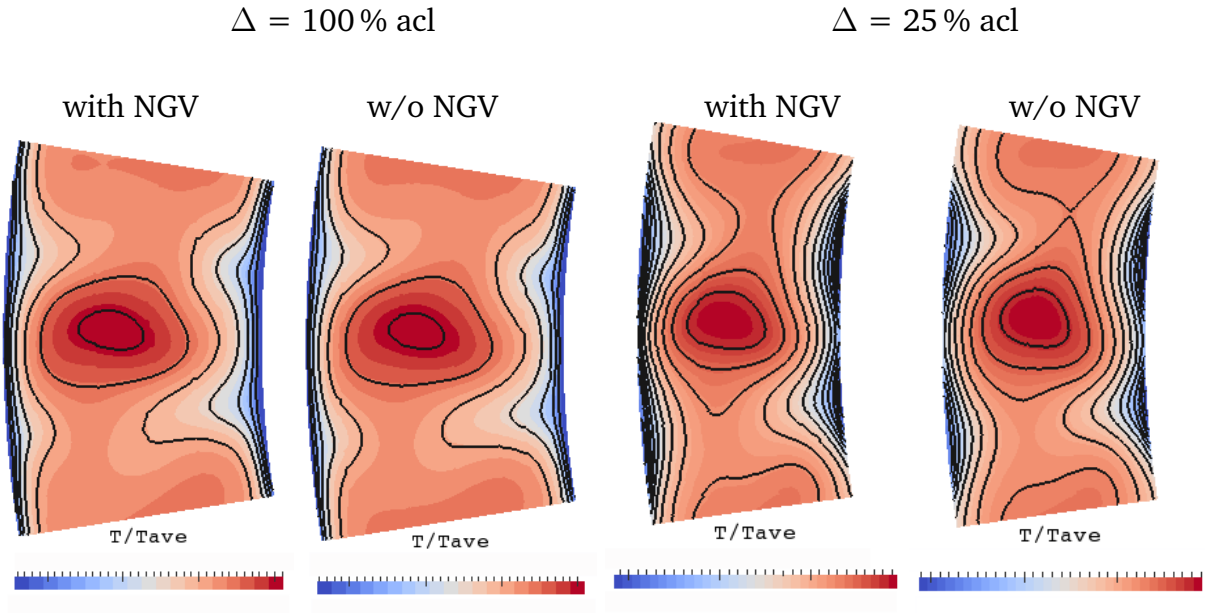

Figure 7.11.: Temperature distribution ($T/T_{average}$) for calculation with and without NGV for two distances Δ in front of the leading edge; acl - axial chord length; iso-contours: steps of 0.1 for Δ= 100 % acl and 0.05 for Δ= 25 % acl

differ for $\Delta = 100\,\%$ acl by 0.3 % percent and for $\Delta = 25\,\%$ by 1 %. Even though the average temperature was used for non-dimensionalization for each case, respectively, some extend of this difference might be attributed to the slightly different AFRs. But it is remarkable that the deviation for the two calculation increases with decreased

[1] The exact scale cannot be shown due to arrangement of confidentiality

distance to the NGV. The distribution is slightly different for the two cases close to the NGV. However, this difference is so small, that it can not distinctly be attributed to an influence from the NGV.

RTDF

The RTDFs for the two simulations are shown in figure 7.12 at three different distances to the leading edge. The plot is arbitrarily scaled while the zero point is shown at the correct position. The shape of the RTDFs is for all distances the same for both

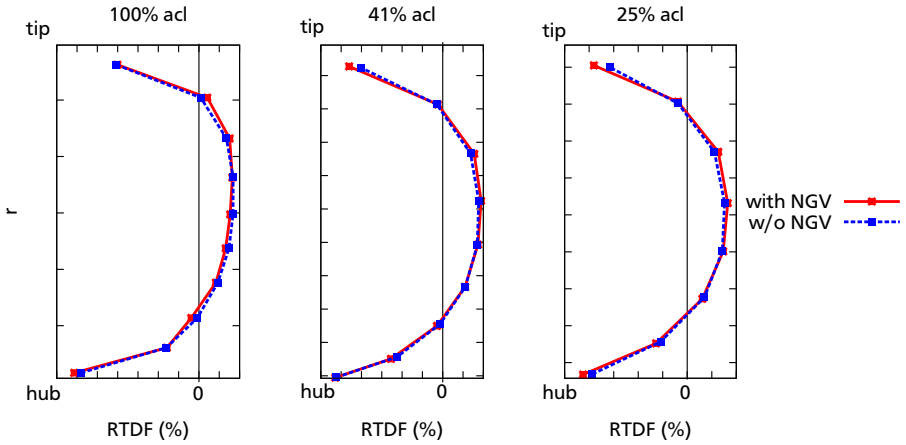

Figure 7.12.: RTDF at three different distances to the leading edge

calculations, 'w' and 'w/o'. Only slight differences can be observed for the two locations closer to the NGV. The RTDF is marginally higher for the calculation 'w' near midspan towards the hub. This is consistent with the observation of higher peak temperature values for that simulation. The value close to the hub is lower for the same calculation. This deviation is caused by the disproportionately higher mass-flow rate at the fourth casing liner for case 'w' (Recall the discussion on disproportional mass-flow deviation for the two cases at the beginning of this section).

OTDF

The difference in OTDF for the two simulations 'w' and 'w/o' is shown in figure 7.13. The OTDF is higher for the calculations with NGV at all axial locations. The peak temperatures for the two simulations are similar at each station while the average temperature is approximately 9 K lower for the case 'w'. This can be attributed to the higher overall AFR in that case. At $\Delta = 125\,\%$ acl the OTDF rises while it is lower again at $\Delta = 100\,\%$ acl. This is probably caused by the higher mass-flow rate at the fourth casing liner. The plane at $\Delta = 125\,\%$ acl is the first one, that takes mass-flow from the fourth

casing liner into account. The imbalance of the splits of mass-flow rates for the two cases seems to have a noticable impact on the OTDF.
Close to the NGV the difference of OTDF is up to twice as high as in the rest of the combustor. The average temperature in case 'w' at these planes is disproportionately lower compared to the temperature difference between the two cases 'w' and 'w/o' at the other planes. Unfortunately, due to the remaining difference in overall mass-flow rate of 0.6 % between the two cases, as mentioned before, the results cannot be definitely attributed to influences from the NGV. However, it is surprising, that the influence steadily increases towards the NGV while influence of the forth liner is already captured in the OTDF at Δ=125 acl and does not seem to be present in the OTDF at Δ=100 % acl anymore.

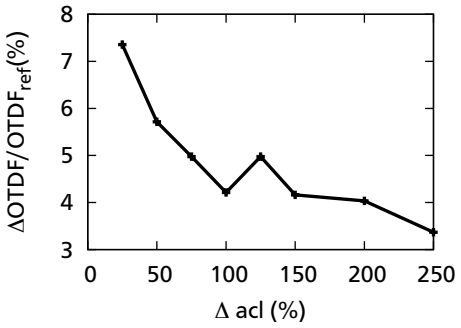

Figure 7.13.: Difference in OTDF (OTDF('w')-OTDF('w/o')) as function of distance Δ to the leading edge, given in % of axial chord length (acl)

7.3.4 Influence on Turbulence Intensities at Combustor Exit

The comparison of turbulence intensities at the five different planes in front of the NGV are shown in figure 7.14. The qualitative pattern is almost the same for the planes at Δ = 200, 150 and 100 % acl. At the distances Δ = 50 and 25 % acl the two intensity peaks are present, which are positioned approximately at the height of the stator's leading edges. While the intensity in case 'w/o' decays in direction of the NGV, it is enforced in calculation 'w'. A distinct impact of the NGVs on the turbulence field near the outlet of the combustor is present. However, this impact does not seem to reach further upstream into the combustor.

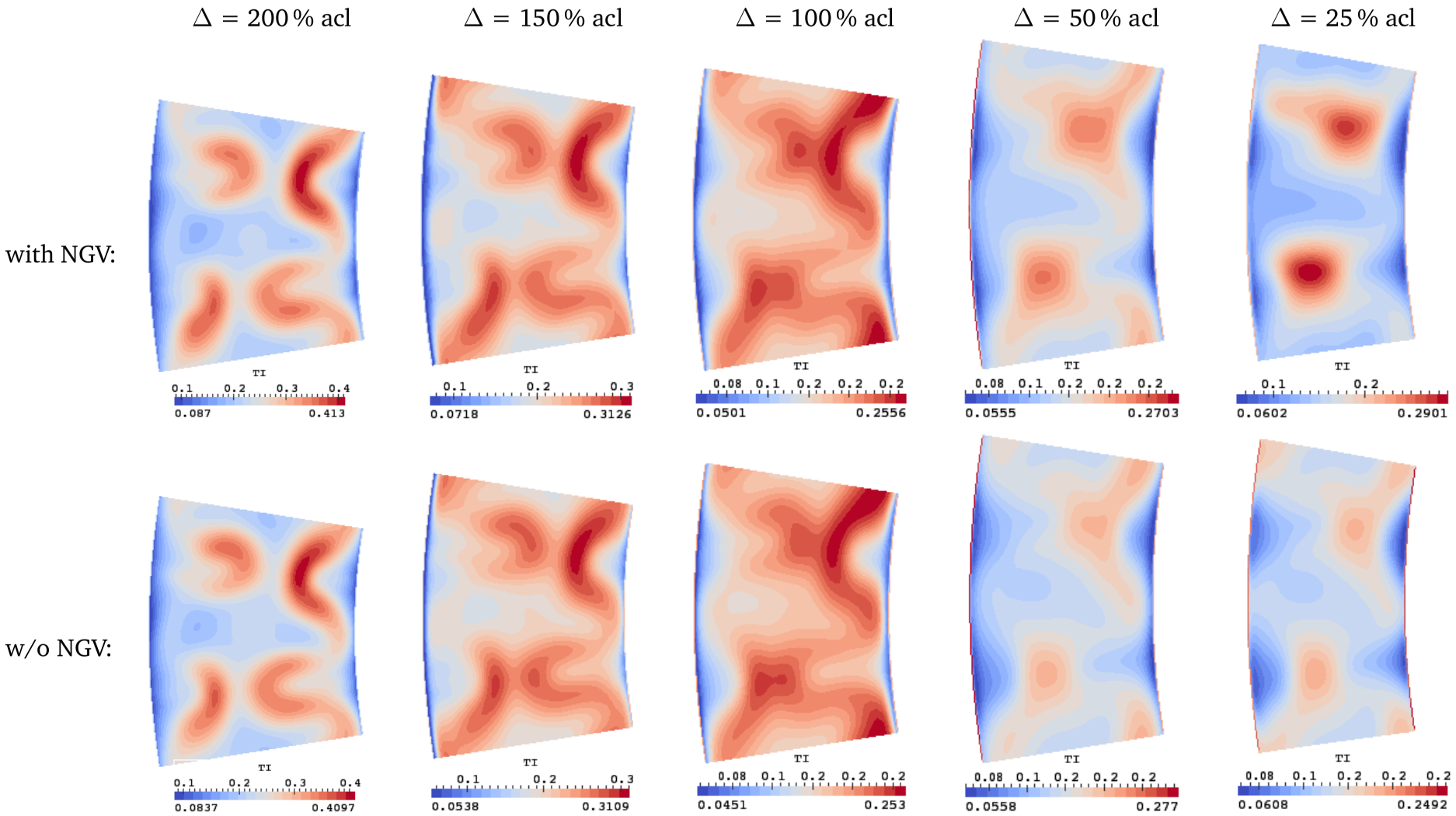

Figure 7.14.: Turbulence intensity distribution (TI = $\sqrt{2/3\,k}/\mathrm{U_{mag}}$) for calculation 'w' and 'w/o' NGV for five distances Δ in front of the leading edge; acl - axial chord length

7.3.5 Conclusion for Position of Combustor-Turbine Interface

As explained in the introduction, today, the influence of the combustor flow on the turbine's flow and heat transfer is numerically investigated by performing parameter variations at the turbine's inlet. The baseline inlet conditions are extracted from incompressible simulations of the reactive flow within the combustor. Within incompressible solvers an open annulus is used as outflow boundary. Influences from the NGV on the combustor flow are thus not accounted for. To ensure, that a combustor exit profile is used, which does not miss influences from the NGV, the data should be read out from the simulation at a plane with sufficient distance to the NGV leading edge. A common ad-hoc approach is the read-out at $\Delta = 100\,\%$ axial chord length. This assumption could be reviewed for the present case while it is suggested to place the read-out plane at a distance of 100 - 150 % axial chord lengths.

Remark: The present simulation was performed for a combustor based on the RQL technology. In Lean-Burn combustors the flow field is very different. Therefore, this result cannot be transferred directly to that technology, but an corresponding simulation of a Lean-Burn combustor should be performed.

7.4 Conclusion for Integrated Simulation

Using the developed code PUC, the reactive flow within a combustor and the compressible flow in the NGV could be simulated in *one* integrated simulation with *one* solver. While similar investigations are reported in the literature [107, 130], the advantage of the present simulation method is the employment of tabled chemistry (FGM), which reduces calculation time and offers the possibility to have a closer look at various reaction species.

8 Conclusion and Outlook

In this work a numerical tool for simulating combustor-turbine interaction was developed. For this purpose the incompressible combustion CFD code PRECISE-UNS was extended with a pressure correction method suitable for all-Mach number flows. For the application of the FGM combustion module a coupling strategy for the extended pressure correction was developed that enables accounting for both, compressible and reactive influence on the fluid temperature.

The first important part of this thesis was the implementation of the extended compressible algorithm into the given CFD code PRECISE-UNS. The treatment of the boundary conditions is of high importance in this context. The implicit treatment of the inlet boundary condition of the original formulation of the all-Mach number SIMPLE algorithm was adapted for three-dimensional calculations. The accuracy of the solver was demonstrated by comparing the results to analytic solutions. A remarkable congruence to the analytic solution could be obtained. The influence of grid resolution and discretization schemes was investigated for various test cases. LUDS was found to be a favorable scheme suppressing oscillations while at the same time maintaining second order accuracy. Validation of the new code PUC showed good comparison to experiments while deviations were consistent to deviations reported in the literature.

The second important part of this thesis was the coupling of the PPDF-FGM chemistry model with the compressible SIMPLE algorithm. A separation of regions with temperature change due to combustion and temperature change due to compressibility was adopted. The verification of this method was conducted for the two limiting regimes, i.e. incompressible reaction and non-reacting compressible flow. It would be favorable to extend this verification and use experimental data for the validation in the compressible reacting regime.

The purpose of PUC is the application to real, complex geometries, i.e. the combustor and NGV of a jet-engine. Therefore, the code was applied to a real NGV from Rolls-Royce Deutschland and its performance compared to that of commercial and in-house tools from Rolls-Royce. A good overall agreement was obtained. It would be favorable to extend the validation for NGV flow using experimental data to further quantify the performance of PUC. A model GT combustor was simulated using the coupled PPDF-FGM/compressible SIMPLE algorithm, and results were compared to experimental measurements. While the used turbulence model showed deficits in predicting all

aspects of the turbulent flow field, the influence of the reaction on the flow field, which were observed in the experiments, were captured well.

The reactive, compressible flow inside a combustor and its adjoining NGVs was successfully simulated in one integrated simulation, using the developed code PUC. Special consideration was given to the explanation of the solver set-up and the necessary initialization of the reactive flow field.

The influence of the NGV on the combustor flow was investigated by a comparison of the integrated simulation to a simulation with the stators removed from the domain. The following are the most important findings:
The calculation with NGV was less sensitive to fluctuations introduced by higher order discretization schemes for the mixture fraction. The mass-flow balance inside the combustor is influenced by the pressure field at its exit. The velocity field is distinctly influenced by the NGV up to a distance of one axial chord length in front of the stator's leading edge. The qualitative temperature distribution is only slightly affected in the rear part of the combustor. The turbulence intensities are largely affected close to the NGVs. The comparison of the two simulations implied that the turbine's inlet boundary condition should be read out from the combustor simulation at approximately 1.5 axial chord lengths for performing parameter variation studies of the turbine flow. Upstream of that plane no influence from the NGV was observed.

Combustor-turbine interaction has been investigated for the last 30 years, considering the aero-thermal effects of the combustor flow on the turbine's flow and heat conditions. The influence of the NGV on the combustor flow field is an emerging aspect under investigation, within this field. It was considered in this thesis, based on the implementations of the compressible SIMPLE algorithm and the PPDF-FGM/compressible SIMPLE coupling. At the moment all implementations have been performed for steady calculations only. The final goal within the nine year period of the graduate school GRK 1344 are unsteady simulations of the whole CTI system using reactive LES. Thus, the implementation of the unsteady terms and according boundary conditions should be the next step. Whether LES in the combustor will be coupled with unsteady RANS (URANS) in the NGV or a Detached Eddy Simulation approach for the whole domain should be favored, remains to be answered by the successor of this work.

A Influence of Flow Change on Reaction

Stoichiometric conditions:

AFR=20:

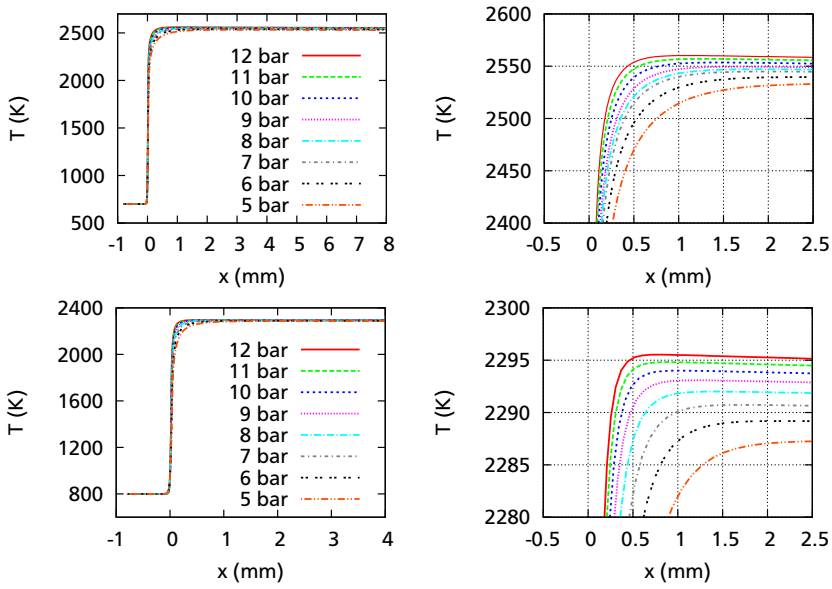

Figure A.1.: Influence of pressure on flame temperature, right plot zoomed, colormap same as in left plot

Stoichiometric conditions:

AFR=20:

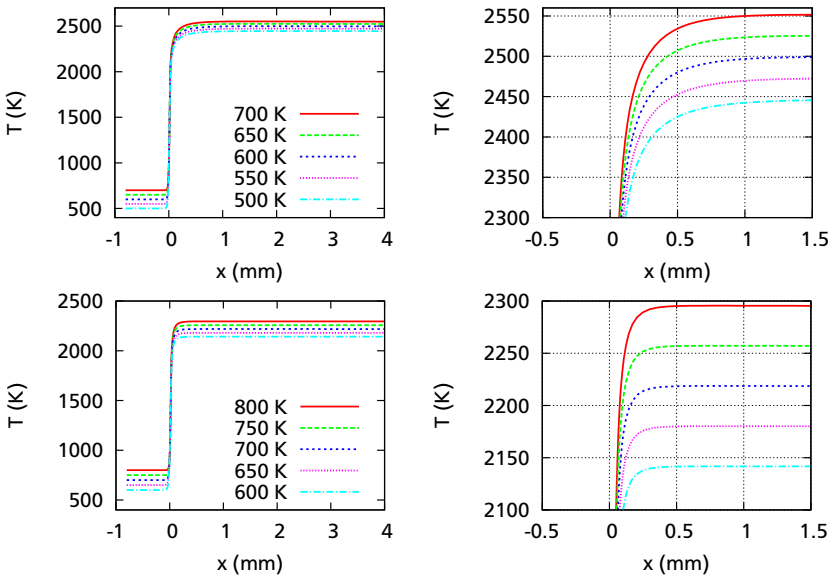

Figure A.2.: Influence of mixture temperature on flame temperature, right plot zoomed, colormap same as in left plot

Stoichiometric conditions:

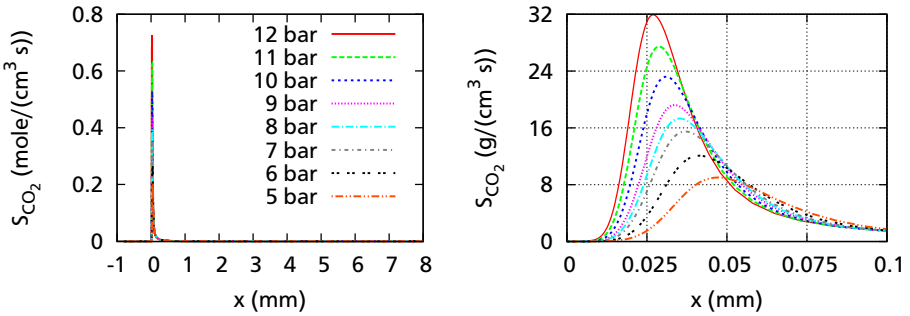

AFR=20:

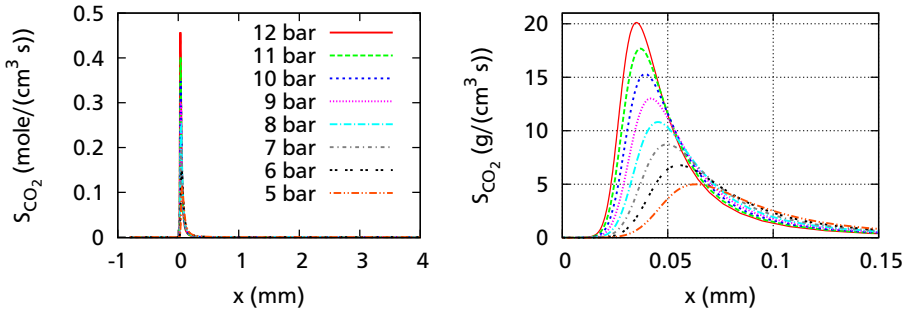

Figure A.3.: Influence of pressure on source term of CO_2, right plot zoomed, colormap same as in left plot

Stoichiometric conditions:

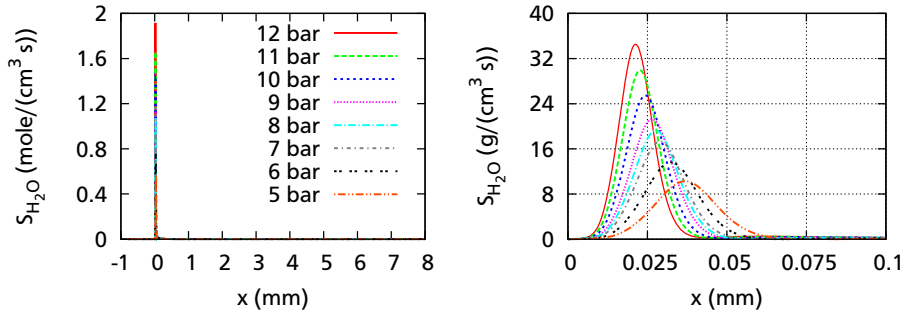

AFR=20:

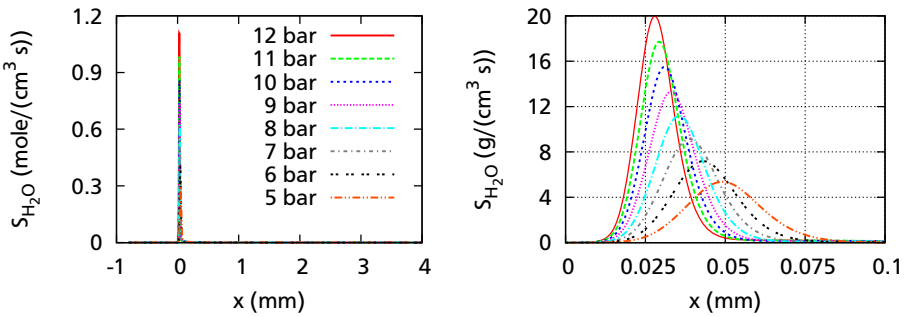

Figure A.4.: Influence of pressure on source term of H_2O, right plot zoomed, colormap same as in left plot

Bibliography

[1] ICAO Annex 16. International Standards and Recommended Practices, Environmental Protection, 2003. plus amendments.

[2] J. J. Alonso, S. Hahn, F. Ham, M. Herrmann, G. Iaccarino., G. Kalitzin, P. LeGresley, K. Mattsson, G. Medic, P. Moin, H. Pitsch, J. Schluter, M. Svard, E.V. der Weide, D. You, and X. Wu. CHIMPS: A High-Performance Scalable Module for Multiphysics Simulations. In *42nd AIAA/ASME/SAE/ASEE Joint Propulsion Conference & Exhibit*. AIAA, July 2006. AIAA-2006-5274.

[3] B.-T. An, J.-J. Liu, and H.-D. Jiang. Combined Unsteady Effects of Hot Streak and Trailing Edge Coolant Ejection in a Turbine stage. In *Proceedings of ASME TurboExpo 2009, Orlando, FL*, 2009. ASME Paper GT2009-59473.

[4] B.-T. An, J.-J. Liu, and H.-D. Jiang. Numerical Investigation on Unsteady Effects of Hot Streak on Flow and Heat Transfer in a Turbine Stage. *ASME Journal of Turbomachinery*, 131:031015–1–15, 2009. ASME Paper 2008.

[5] B. A. Bangert, A. Kohli, J. H. Sauer, and K. A. Thole. High Freestream Turbulence Simulation in a Scaled-up Turbine Vane Passage. In *Proceedings of the International Gas Turbine & Aeroengine Congress and Exhibit, Orlando, FL*, 1997. ASME Paper 1997-GT-51.

[6] R. Barlow and J. Frank. Piloted CH_4/Air Flames C, D, E and F - Release 2.0, 2003. `http://www.ca.sandia.gov/TNF`.

[7] R. Barlow, J. H. Frank, A. N. Karpetis, and J.-Y. Chen. Piloted Methane/Air Jet Flames: Transport Effects and Aspects of Scalar Structure. *Combustion and Flame*, 143:433–449, 2005.

[8] M. D. Barringer, O. T. Richard, J. P. Walter, S. M. Stitzel, and K. A. Thole. Flow Field Simulations of a Gas Turbine Combustor. *Journal of Turbomachinery*, 124:508–516, 2002. ASME Paper 2001-GT-0170.

[9] M. D. Barringer, K. A. Thole, and M. D. Polanka. Developing a Combustor Simulator for Investigating High Pressure Turbine Aerodynamics and Heat Transfer. In *Proceedings of ASME Turbo Expo 2004, Vienna, Austria*, June 2004. GT 2004-5613.

[10] M. D. Barringer, K. A. Thole, and M. D. Polanka. Experimental Evaluation of an Inlet Profile Generator for High-Pressure Turbine Tests. *Journal of Turbomachinery*, 129:382–393, 2007. ASME Paper GT2006-90401.

[11] M. D. Barringer, K. A. Thole, and M. D. Polanka. Effects of Combustor Exit Profiles on Vane Aerodynamic Loading and Heat Transfer in a High Pressure Turbine. *ASME Journal of Turbomachinery*, 131:021008–1–10, 2009. ASME Paper GT 2006-90277.

[12] M. D. Barringer, K. A. Thole, and M. D. Polanka. An Experimental Study of Combustor Exit Profile Shapes on Endwall Heat Transfer in High Pressure Turbine Vanes. *ASME Journal of Turbomachinery*, 131:021009–1–10, 2009.

[13] M. D. Barringer, K. A. Thole, M. D. Polanka, J. P. Clark, and P. J. Koch. Migration of Combustor Exit Profiles Through High Pressure Turbine Vanes. *ASME Journal of Turbomachinery*, 131:021010–1–10, 2009.

[14] T. B. Benjamin. Theory of the Vortex Breakdown Phenomenon. *Journal of Fluid Mechanics*, 14(4):pp.593–629, 1962.

[15] T. B. Benjamin. Some Developments in the Theory of Vortex Breakdown. *Journal of Fluid Mechanics*, 28(1):pp.65–84, 1967.

[16] T. J. Bogar, M. Sajben, and J. C. Kroutil. Characteristic Frequencies of Transonic Diffuser flow Oscillations. *AIAA*, 21(9):1232–1240, 1983.

[17] K. N. C. Bray, M. Champion, P. A. Libby, and N. Swaminathan. Finite Rate Chemistry and Presumed Pdf Models for Premixed Turbulent Combustion. *Combustion and Flame*, 146(4):665 – 673, 2006.

[18] I. N. Bronstein, K. A. Semendjajew, G. Musiol, and H. Mühlig. *Taschenbuch der Mathematik*, volume 7. Verlag Harry Deutsch, 2008.

[19] S. W. Burd, C. J. Satterness, and T. Simon. Effects of Slot Bleed Injection over a Contoured Endwall on Nozzle Guide Vane Cooling Performance: Part II - Thermal Measurements. In *Proceedings of ASME TurboExpo 2000, Munich, Germany*, 2000. 2000-GT-200.

[20] S. W. Burd and T. Simon. Effects of Slot Bleed Injection over a Contoured Endwall on Nozzle Guide Vane Cooling Performance: Part I - Flow Field Measurements. In *Proceedings of ASME TurboExpo 2000, Munich, Germany*, 2000. 2000-GT-199.

[21] T. L. Butler, O. P. Sharma, H. D. Joslyn, and R. P. Dring. Redistribution of an Inlet Temperature Distortion in an Axial Flow Turbine Stage. *Journal of Propulsion and Power*, 5:64–71, 1986. AIAA Paper 86-1468.

[22] N. D. Cardwell, N. Sundaram, and K. A. Thole. The Effects of Varying the Combustor-Turbine Gab. *Journal of Turbomachinery*, 129:756–764, 2007. ASME Paper GT2006-90089.

[23] L. Caretto, A. Gosman, S. Patankar, and D. Spalding. Two Calculation Procedures for Steady, Three-dimensional Flows with Recirculation. In Henri Cabannes and Roger Temam, editors, *Proceedings of the Third International Conference on Numerical Methods in Fluid Mechanics*, volume 19 of *Lecture Notes in Physics*, pages 60–68. Springer Berlin, Heidelberg, 1973.

[24] CHEM1D. A One-dimensional Laminar Flame Code. Eindhoven University of Technology, `http://www.combustion.tue.nl/chem1d`.

[25] W. F. Colban and K. A. Thole. Combustor Turbine Interface Studies - Part 1: Endwall Effectiveness Measurements. *ASME Journal of Turbomachinery*, 125:193–202, 2003. ASME Paper 2002-GT-30526.

[26] W. F. Colban and K. A. Thole. Combustor Turbine Interface Studies - Part 1: Flow and Thermal Field Measurements. *Journal of Turbomachinery*, 125:203–209, 2003. ASME Paper 2002-GT-30527.

[27] R. Courant, K. Friedrichs, and H. Lewy. Über die partiellen Differenzengleichungen der mathematischen Physik. *Mathematische Annalen*, 100(1):32–74, December 1928.

[28] I. Demirdzic, Z. Lilek, and M. Peric. A Collocated Finite Volume Method for Predicting Flows at all Speeds. *Int. Journal for Numerical Methods in Fluids*, 16:1029–1050, 1993.

[29] Doktoranden des Graduiertenkollegs 1344. Projektplanung zur Untersuchung instationärer Effekte in einem Flugtriebwerk am Beispiel von Windmill-Relight, 2009. Common project of the first generation of graduates from the DFG graduate school 1344.

[30] F. DiMare, W. P. Jones, and K. R. Menzies. Large Eddy Simulation of a Model Gas Turbine Combustor. *Combustion and Flame*, 137(3):278 – 294, 2004.

[31] P. Domingo, L. Vervisch, S. Payet, and R. Hauguel. DNS of a Premixed Turbulent V Flame and LES of a Ducted Flame Using a FSD-PDF Subgrid Scale Closure with FPI-Tabulated Chemistry. *Combustion and Flame*, 143(4):566 – 586, 2005. Special Issue to Honor Professor Robert W. Bilger on the Occasion of His Seventieth Birthday.

[32] D. J. Dorney, R. L. Davis, and D. E. Edwards. Investigation of Hot Streak Migration and Film cooling Effects on Heat Transfer in Rotor/Stator Interacting Flows.

Technical report, NAVAIR Final Report N00140-88-C-0677, 1992. Report 1 and 2.

[33] D. J. Dorney, R. L. Davis, D. E. Edwards, and N. K. Madavan. Unsteady Analysis of Hot Streak Migration in a Turbine Stage. In *Proceedings of 27th Joint Propulsion Conference and Exhibit, Sacraments, FL*, 1990. AIAA Paper 90-2354.

[34] D. J. Dorney and D. L. Sondak. Study of the Effects of Hot Streaks on Heat Transfer in Subsonic and Transonic Flows. In *Proceedings of 32nd Joint Propulsion Conference and Exhibit, Lake Buena Vista, FL*, 1996. AIAA Paper 96-2923.

[35] D. J. Durney, K. L. Gundy-Burlet, and D. L. Sondak. Survey of Hot Streak Experiments and Simulations. *International Journal of Turbo and Jet Engines*, 16(1):1–15, 1999.

[36] M. P. Escudier, A. K. Nickson, and R. L. Poole. Influence of Outlet Geometry on Strongly Swirling Turbulent Flow through a Circular Tube. *Physics of Fluids*, 18, 2006.

[37] B. Fiorina, O. Gicquel, L. Vervisch, S. Carpentier, and N. Darabiha. Premixed Turbulent Combustion Modeling Using Tabulated Detailed Chemistry and Pdf. *Proceedings of the Combustion Institute*, 30(1):867 – 874, 2005.

[38] M. Freitag. On the Simulation of Premixed Combustion Taking Into Account Variable Mixtures, 2007. Dissertation, TU Darmstadt.

[39] N. J. Georgiadis, J. E. Drummond, and B. P. Leonard. Evaluation of Turbulence Models in the PARC Code for Transonic Diffuser Flows. Technical Report TM-106391, NASA, 1994.

[40] VDI Gesellschaft Verfahrenstechnik und Chemieingenieurwesen, editor. *VDI-Wärmeatlas*. Springer-Verlag Berlin Heidelberg, 2006.

[41] J. Gikadi. Turbulence Modeling for Simulation of Combustor - Turbine Interaction in a Jet Engine. Master's thesis, TU Darmstadt, 2009.

[42] P. Givi, C. K. Madnia, C. J. Steinberger, M. H. Carpenter, and J. P. Drummond. Effects of Compressibility and Heat Release in a High Speed Reacting Mixing Layer. *Combustion Science and Technology*, 78:33–67, 1991.

[43] R. J. Goldstein, K. Y. Lau, and C. C. Leung. Velocity and Turbulence Measurements in Combustion Systems. *Experiments in Fluids*, 1:93–99, 1983.

[44] F. Hahn. Zur Vorhersage technischer Verbrennungssysteme im Hinblick auf flüssige Brennstoffe, 2009. Dissertation, TU Darmstadt, Institut für Energie- und Kraftwerkstechnik.

[45] C. W. Haldeman, M. G. Dunn, C. D. MacArthur, and C. G. Murawski. The USAF Advanced Turbine Aerothermal Research Rig (ATARR). In *NATO AGARD Propulsion and Energetics Panel Conference Proceedings 527, Antalya, Turkey*, 1992.

[46] L. He, V. Menshikova, and B. R. Haller. Effect of Hot-Streak Counts on Turbine Blade Heat Load and Forcing. *AIAA Journal of Propulsion and Power*, 23:1235–1241, 2007.

[47] K. S. Hermanson and K. A. Thole. Effect of Inlet Conditions on Endwall Secondary Flows. *AIAA Journal of Propulsion and Power*, 16(2):286–296, 2000.

[48] K. S. Hermanson and K. A. Thole. Effect of Nonuniform Inlet Conditions on Endwall Secondary Flows. *ASME Journal of Turbomachinery*, 124(4):623–631, 2002.

[49] H. Herwig. *Strömungsmechanik A-Z*. Vieweg und Sohn, 2004.

[50] C. Hirsch. *Numerical Computation of Internal and External Flows*, volume 1 and 2. Wiley, 1991.

[51] J. O. Hirschfelder, C. F. Curtis, and R. B. Bird. *Molecular Theory of Gases and Liquids*. Wiley, 1969.

[52] Hypre. `https://computation.llnl.gov/casc/hypre/software.html`.

[53] ICAO. ICAO Engine Emissions Databank - Issue 16A, February 2009.

[54] A. Ingenito and C. Bruno. Reaction Regime in Supersonic Flows. In *47th AIAA Aerospace Sciences Meeting, Orlando, Florida*, 2009.

[55] B. Janus. Laseroptische Untersuchungen in einer generischen Gasturbinenbrennkammer, 2005. Dissertation, TU Darmstadt, Institut für Energie- und Kraftwerkstechnik.

[56] B. Janus, A. Dreizler, and J. Janicka. Experimental Study on Stabilization of Lifted Swirl Flames in a Model GT Combustor. *Flow, Turbulence and Combustion*, 75:293–315, 2005.

[57] S. Jenkins and D. G. Bogard. The Effects of the Vane and Mainstream Turbulence Level on Hot Streak Attenuation. *ASME Journal of Turbomachinery*, 127(1):215–221, 2005.

[58] S. Jenkins, K. Varadarajan, and D. G. Bogard. The Effects of High Mainstream Turbulence and Turbine Vane Film Cooling on the Dispersion of a Simulated Hot Streak. *ASME Journal of Turbomachinery*, 126(1):203–211, 2004.

[59] W. P. Jones and B. E. Launder. The Calculation of Low-Reynolds Number Phenomenon with a Two-Equation Model of Turbulence. *International Journal of Heat and Mass Transfer*, 16:119–1130, 1973.

[60] M. B. Kang, A. Kohli, and K. A. Thole. Heat transfer and Flowfield Measurements in the Leading Edge Region of a Stator Vane Endwall. *ASME Journal of Turbomachinery*, 121(3):558–568, 1999. ASME Paper 1998-GT-173.

[61] A. Ketelheun. Applikation und Untersuchung der Flamelet Generated Manifolds Theorie im Hinblick auf Mischungsbrüche außerhalb der Zündgrenzen. Master's thesis, TU Darmstadt, 2008.

[62] A. Ketelheun, C. Olbricht, F. Hahn, and J. Janicka. NO Prediction in Turbulent Flames using LES/FGM with Additional Transport Equations. In *33rd International Symposium on Combustion, Peking, China*, 2010.

[63] S. W. Kim. Numerical Investigation of Chemical Reaction-Turbulence Interaction in Compressible Shear Layers. *Combustion and Flame*, 101:197–208, 1995.

[64] V. Klapdor, S. Pyliouras, R.G.L.M. Eggels, and J. Janicka. Towards Simulation of Combustor Turbine Interaction in an Integrated Simulation. In *Proceedings of ASME Turbo Expo, Glasgow, UK*, 2010. ASME Paper GT 2010-22933.

[65] P. Koutmos and J. J. McGuirk. Isothermal Flow in a Gas Turbine Combustor - a Benchmark Experimental Study. *Experiments in Fluids*, 7:344–354, 1989.

[66] B. Krouthen and M. B. Giles. Numerical Investigations of Hot Streaks in Turbines. In *Proceedings of 24th Joint Propulsion Conference and Exhibit, Bosten, MA*, 1988. AIAA Paper 88-3015.

[67] J. Kuehne, A. Ketelheun, and J. Janicka. Analysis of Sub-grid PDF of a Progress Variable Approach Using a Hybrid LES/TPDF Method. *Proceedings of the Combustion Institute*, 2010.

[68] T. Landenfeld, A. Sadiki, and J. Janicka. A Turbulence-Chemistry Interaction Model Based on a Multivariate Presumed Beta-PDF Method for Turbulent Flames. *Flow, Turbulence and Combustion*, 68:111–135, 2002.

[69] L. S. Langston. Crossflows in a Turbine Cascade Passage. *ASME Journal Eng. Power*, 102:866–874, 1980.

[70] B. L. Lapworth. Advanced Compressor Design Incorporating Real Geometry Features. *ISABE Paper 2007-1306*, 2007.

[71] B. E. Launder, G. J. Reece, and W. Rodi. Progress in the Development of a Reynolds-Stress Turbulent Closure. *Journal of Fluid Mechanics*, 68:537–566,

1975.

[72] B. E. Launder and B. I. Sharma. Application of the Energy Dissipation Model of Turbulence to the Calculation of Flow Near a Spinning Disc. *International Journal of Heat and Mass Transfer*, 15:301–314, 1974.

[73] W. Lazik, T. Doerr, and S. Bake. Low NOx Combustor Development for the Engine3E Core Engine Demonstrator. *ISABE paper 2007-1190*, 2007.

[74] W. Lazik, T. Doerr, S. Bake, R. v. d. Bank, and L. Rackwitz. Development of Lean-Burn Low-NOx Combustion Technology at Rolls-Royce Deutschland. *ASME paper 2008-51115*, 2008.

[75] Arthur H. Lefebvre. *Atomization and sprays*. Hemisphere Pub. Corp., 1989.

[76] K. Mahesh, G. Constantinescu, S. Apte, G. Iaccarino, F. Ham, and P. Moin. Large-Eddy Simulation of Reacting Turbulent Flows in Complex Geometries. *Journal of Applied Mechanics*, 73(3):374–381, 2006.

[77] F. Martelli, P. Adami, S. Salvadori, K. S. Chana, and L. Castillon. Aero-Thermal Study of the Unsteady Flow Field in a Transonic Gas Turbine with Inlet Temperature Distortions. In *Proceedings of ASME Turbo Expo, Berlin, Germany*, 2008. ASME Paper GT2008-50628.

[78] M. L. Mason, L. E. Putnam, and R. J. Re. The Effect of Throat Contouring on Two-Dimensional Converging-Diverging Nozzles at Static Conditions. Technical Report NASA Technical Paper 1704, NASA, 1980.

[79] G. Medic, D. You, G. Kalitzin, M. Herrmann, F. Ham, H. Pitsch, E. v. d. Weide, and J. Alonso. Integrated Computations of an Entire Jet Engine. In *Proceedings of GT2007*, GT2007-27094. ASME, 2007.

[80] R. De Meester and B. Merci. Hybrid RANS/PDF Calculations of Sydney Swirling Flames. In *Proceedings of the European Combustion Meeting*, 4th, 2009.

[81] R. F. Menter. Zonal Two Equation k-ω Turbulence Models for Aerodynamic Flows. *AIAA Paper 93-2906*, 1993.

[82] V. Michelassi and T.-H. Shih. Low Reynolds Number Two-Equation Modeling of Turbulent Flows. Technical report, NASA, 1991.

[83] R. W. Moss and M. L. G. Oldfield. Measurements of Hot Combustor Turbulence Spectra, 1991. ASME Paper 91-GT-351.

[84] S. Muzaferija. *Adaptive Finite Volume Method for Flow Predictions Using Unstructured Meshes and Multigrid Approach*. PhD thesis, University of London, 1994.

[85] NASA. NPARC Alliance Validation Archive. On the WWW, 2008. URL http://www.grc.nasa.gov/WWW/wind/valid/transdif/transdif.html.

[86] Report of the Group of Personalities. European Aeronautics: A Vision for 2020, 2001.

[87] C. Olbricht. Numerische Berechnung technischer Verbrennungssysteme, 2009. Dissertation, TU Darmstadt, Institut für Energie- und Kraftwerkstechnik.

[88] V. C. Patel, W. Rodi, and G. Scheuerer. Turbulence Models for Near-wall and Low Reynolds number flows - A review. *AIAA*, 23(9):1308–1319, 1985.

[89] M. Peric. *Computational Fluid Dynamics*. Springer, 2002.

[90] H. Pitsch. Large-Eddy Simulation of Turbulent Combustion. *Annual Review of Fluid Mechanics*, 38(1):453–482, 2006.

[91] T. Poinsot and D. Veynante. *Theoretical and Numerical Combustion, Second Edition*. Edwards, 2005.

[92] M. D. Polanka. *Detailed Film Cooling Effectiveness and Three Component Velocity Field Measurements on a First Stage Turbine Vane Subject to High Freestream Turbulence*. PhD thesis, University of Texas at Austin, 1999.

[93] M. D. Polanka, J. M. Cutbirth, and D. G. Bogard. Three Component Velocity Field Measurements in the Stagnation Region of a Film Cooled Turbine Vane. *ASME Journal of Turbomachinery*, 124(3):445–452, 2002.

[94] S. B. Pope. An Explanation of the Turbulent Round-Jet/Plane-Jet Anomaly. *AIAA Journal*, 16(3):279–280, 1978.

[95] S. B. Pope. A Rational Method of Determininig Probability Distributions in Turbulent Reacting Flows. *Journal of Non-Equilibrium Thermodynamics*, 4:309–320, 1979.

[96] S. B. Pope. *Turbulent Flows*. Cambridge University Press, New York, 2000.

[97] T. Povey, K. S. Chana, T. V. Jones, and J. Hurrion. The Effect of Hot-Streaks on HP Vane Surface and Endwall Heat Transfer: An Experimental and Numerical Study. *Journal of Turbomachinery*, 129:32–43, 2007.

[98] T. Povey and I. Qureshi. Developments in Hot-Streak Simulators for Turbine Testing. *ASME Journal of Turbomachinery*, 131:031009–1–15, 2009.

[99] R. W. Radomsky and K. A. Thole. Flowfield Measurements for a Highly Turbulent Flow in a Stator Vane Passage. *ASME Journal of Turbomachinery*, 122:255–262, 2000. ASME Paper 99-GT-253.

[100] R. W. Radomsky and K. A. Thole. High Free-Stream Turbulence Effects on Endwall Heat Transfer for a Gas Turbine Stator Vane. *ASME Journal of Turbomachinery*, 122:699–708, 2000. ASME Paper 2000-GT-201.

[101] M. M. Rai and R. P. Dring. Navier-Stokes Analyses of the Redistribution of Inlet Temperature Distortions in a Turbine. In *Proceedings of 23rd Joint Propulsion Conference and Exhibit, San Diego, CA*, 1987. AIAA Paper 87-2146.

[102] W. J. S. Ramaekers. The Application of Flamelet Generated Manifolds in Modelling of Turbulent Partially-Premixed Flames. Master's thesis, Eindhoven University of Technology, 2002.

[103] R. P. Rhodes. A Probability Distribution Function for Turbulent Flows. In S. N. B. Murthy, editor, *Turbulent Mixing in Nonreactive and Reactive Flows*, pages 235–241, 1975.

[104] A. Rizzi and H. Viviand. *Numerical Methods for the Computation of Inviscid Transonic Flows with Shock Waves. Notes on Numerical Fluid Mechanics*, volume 3. Vieweg, Braunschweig, 1981.

[105] W. Rodi. *The Prediction of Free Turbulent Boundary Layers by Use of Two-equation Model of Turbulence*. PhD thesis, University of London, 2007.

[106] Rolls-Royce. *The Jet Engine*. Rolls-Royce plc, 5 edition, 2005.

[107] S. Roux, M. Cazalens, and T. Poinsot. Outlet-Boundary-Condition Influence for Large Eddy Simulation of Combustion Instabilities in Gas Turbines. *Journal of Propulsion and Power*, 24(3):541–546, May-June 2008.

[108] Y. Saad. A Basic Tool-kit for Sparse Matrix Computations (Version 2), 2009. `http://www-users.cs.umn.edu/~saad/software/SPARSKIT/sparskit.html`.

[109] M. M. Salehi and W. K. Bushe. Presumed PDF Modeling for RANS Simulation of Turbulent Premixed Flames. *Combustion Theory and Modelling*, 14(3):381–403, 2010.

[110] J. T. Salmon, T. J. Bogar, and M. Sajben. Laser Doppler Velocimeter Measurements in Unsteady, Separated Transonic Diffuser Flows. *AIAA*, 21(12):1690–1697, 1983.

[111] S. Sarkar and L. Balakrishnan. Application of a Reynolds-Stress Turbulence Model to the Compressible Shear Layer. Technical Report NASA CR 182002, ICASE Report 90-18, 1990.

[112] H. Schlichting and K. Gersten. *Grenzschicht-Theorie*. Springer, Berlin, 10th edition, 2006.

[113] J. U. Schlüter, H. Pitsch, and P. Moin. Large Eddy Simulation Inflow Conditions for Coupling with Reynolds-Averaged Flow Solvers. *AIAA Journal*, 42(3):478–484, 2004.

[114] J. U. Schlüter, X. Wu, E. v. d. Weide, S. Hahn, J. J. Alonso, and H. Pitsch. Multi-Code Simulations: A Generalized Coupling Approach. In *17th AIAA Computational Fluid Dynamics Conference*, June 2005. AIAA-2005-4997.

[115] M. Schäfer. *Numerik im Maschinenbau*. Springer Verlag, 1st edition, 1999.

[116] S. Shahpar and B. L. Lapworth. PADRAM: Parametric Design and Rapid Meshing System for Turbomachinery Optimisation. In *Proceedings of ASME Turbo Expo, Atlanta, GA*, 2003. ASME Paper GT 2003-38698.

[117] T. Shang, G. R. Guenette, A. H. Epstein, and P. A. Saxer. The Influence of Inlet Temperature Distortions on Rotor Heat Transfer in a Transonic Turbine. In *Proceedings of 31st Joint Propulsion Conference and Exhibit, San Diego, CA*, 1995. AIAA 95-3042.

[118] T. H. Shih, W. W. Liou, A. Shabbir, Z. Yang, and J. Zhu. A New k-ϵ Eddy-Viscosity Model for High Reynolds Number Turbulent Flows. *Computers and Fluids*, 24(3):227–238, 1995.

[119] G. P. Smith, D. M. Golden, M. Frenklach, N. M. Moriarty, B. Eiteneer, M. Goldenberg, C. T. Bowman, R. K. Hanson, S. Song, W. C. Gardiner Jr., V. V. Lissianski, and Z. Qin. `http://www.me.berkeley.edu/gri_mech/`.

[120] B. Somers. *The Simulation of Flat Flames with Detailed and Reduced Chemical Models*. PhD thesis, TU Eindhoven, 1994.

[121] P. R. Spalart and S. R. Allmaras. A One-Equation Turbulence Model for Aerodynamic Flows. *AIAA, 30th Aerospace Sciences Meeting and Exhibit*, 1992.

[122] Spurk. *Strömungslehre*. Springer, 6th edition, 2006.

[123] R. G. Stabe, W. J. Whitney, and T. P. Moffitt. Performance of a High-work low Aspect Ration Turbine Tested with a Realistic Inlet Radial Temperature Profile. Technical report, NASA TM 83655, 1984. AIAA Paper 84-1161.

[124] S. Stitzel and K. A. Thole. Flow Field Computations of Combustor-Turbine Interactions Relevant to a Gas Turbine Engine. *Journal of Turbomachinery*, 126(1):122–129, 2004.

[125] S. M. Stitzel. Flow Field Computations of Combustor-Turbine Interactions in a Gas Turbine Engine. Master's thesis, Virginia Polytechnic Institute and State University, 2001.

[126] R. K. Takahashi and R. H. Ni. Unsteady Euler Analysis of the Redistribution of an Inlet Temperature Distortion in a Turbine. In *Proceedings of 26th Joint Propulsion Conference and Exhibit, Orlando, FL*, 1990. AIAA Paper 90-2262.

[127] R. K. Takahashi and R. H. Ni. Unsteady Hot Streak Simulation Through a 1-1/2 Stage Turbine. In *Proceedings of 26th Joint Propulsion Conference and Exhibit, Orlando, FL*, 1991. AIAA Paper 91-3382.

[128] FLUENT Inc. *Fluent 6.3. User's Guide*, 2006.

[129] C. Tropea and S. Grundmann. *Aerodynamik II*. Shaker Verlag, 2004.

[130] M. D. Turell, P. J. Stopford, K. J. Syed, and E. Buchanan. Cfd Simulation of the Flow Within and Downstream of a High-Swirl Lean Premixed Gas Turbine Combustor. In *Proceedings of Turbo Expo, Vienna, Australia*, 2004. ASME Paper GT 2004-53112.

[131] J. A. van Oijen. *Flamelet-Generated Manifolds: Development and Application to Premixed Laminar Flames*. Phd Thesis, Eindhoven University of Technology, 2002.

[132] J. Warnatz, U. Maas, and R. W. Dibble. *Combustion*. Springer-Verlag Berlin Heidelberg, 4th edition, 2006.

[133] J. Weiss, J. P. Maruszewski, and W. A. Smith. Implicit Solution of the Preconditioned Navier-Stokes Equations Using Algebraic Multigrid. *AIAA Journal*, 37:29–36, 1999.

[134] C. Westbrook and H. Dryer. Simplified Reaction Mechanisms for the Oxidation of Hydrocarbon Fuels in Flames. *Combustion Science and Technology*, 2:31–47, 1981.

[135] D. C. Wilcox. Re-assessment of the Scale-determining Equation for Advanced Turbulence Models. *AIAA Journal*, 26:1414–1421, 1988.

[136] D. C. Wilcox. *Turbulence Modeling for CFD*. DCW Industries, Inc., La Canada, California, 1994.

[137] F. A. Williams. *Combustion Theory, 2nd edition*. Addison-Wesley, 1985.

[138] J. L. Xia, B. L. Smith, A. C. Benim, J. Schmidli, and G. Yadigaroglu. Effect of Inlet and Outlet Boundary Conditions on Swirling Flows. *Computers and Fluids*, 26(8):811–823, 1997.

[139] V. Yakhot, S. A. Orszag, S. Thangham, T. B. Gatski, and C. G. Speziale. Development of Turbulence Models for Shear Flows by a Double Expansion Technique. *Physics of Fluids A*, 4(7):1510–1520, 1992.

[140] Y. B. Zeldovich. The Oxidation of Nitrogen in Combustion and Explosion. *Acta Physichochim URSS*, 21, 1946.

Lebenslauf

Name	Eva Verena Klapdor
Geburtsdatum	30.08.1982
Geburtsort	Duisburg

07.1992 - 06.2001	St. Hildegardis Gymnasium, Duisburg Abitur
10.2001 - 09.2002	Westfälische Wilhelms-Universität Münster Jurastudium (ohne Abschluss)
10.2002 - 07.2005	Universität Duisburg-Essen International Studies in Engineering Abschluss: Bachelor of Science in Mechanical Engineering
01.2004 - 06.2004	Lunds University of Technology, Schweden Erasmus Austausch
	Auslandsaufenthalt in China:
08.2005 - 12.2005	Praktikum im Delegiertenbüro der dt. Wirtschaft in Peking
01.2006 - 03.2006	Praktikum bei Siemens-Shanghai Turbine Company in Shanghai
04.2006 - 10.2007	Technische Universität Darmstadt Studium des Allgemeinen Maschinenbau Abschluss: Master of Science in Mechanical Engineering
11.2007 - 10.2010	Stipendiatin im DFG Graduiertenkolleg 1344 "Instationäre Systemmodellierung eines Flugtriebwerks" Technische Universität Darmstadt Fachgebiet für Energie- und Kraftwerkstechnik